



PERFORMANCE CHARACTERIZATION  
OF A THREE-AXIS  
HALL EFFECT THRUSTER

THESIS

Spencer E. Temkin, Lieutenant Commander, USN

AFIT/GAE/ENY/10-D02

DEPARTMENT OF THE AIR FORCE  
AIR UNIVERSITY

**AIR FORCE INSTITUTE OF TECHNOLOGY**

Wright-Patterson Air Force Base, Ohio

APPROVED FOR PUBLIC RELEASE; DISTRIBUTION UNLIMITED.

The views expressed in this thesis are those of the author and do not reflect the official policy or position of the United States Air Force, United States Navy, Department of Defense, or the United States Government.

AFIT/GAE/ENY/10-D02

PERFORMANCE CHARACTERIZATION  
OF A THREE-AXIS  
HALL EFFECT THRUSTER

THESIS

Presented to the Faculty  
Department of Aeronautics and Astronautics  
Graduate School of Engineering and Management  
Air Force Institute of Technology  
Air University  
Air Education and Training Command  
In Partial Fulfillment of the Requirements for the  
Degree of Master of Science in Aeronautical Engineering

Spencer E. Temkin, AB  
Lieutenant Commander, USN

December 2010

APPROVED FOR PUBLIC RELEASE; DISTRIBUTION UNLIMITED.

PERFORMANCE CHARACTERIZATION  
OF A THREE-AXIS  
HALL EFFECT THRUSTER

Spencer E. Temkin, AB  
Lieutenant Commander, USN

Approved:

/signed/ _____ Lt.Col. R.E. Huffman, PhD (Chairman)	17 December 2010 _____ date
/signed/ _____ Lt.Col. C.R. Hartsfield, PhD (Member)	17 December 2010 _____ date
/signed/ _____ W.A. Hargus, Jr., PhD (Member)	17 December 2010 _____ date
/signed/ _____ Lt.Col. R.D. Branam, PhD (Member)	17 December 2010 _____ date

*Abstract*

The research presented here represents the first efforts to operate and quantify the performance of a three-axis Hall effect thruster. This thruster is based on the Busek BHT-200 and used a novel construction with three orthogonal faces and a common magnetic core to reduce size and weight. Operating procedures for the thruster were developed and thrust and current density measurements were performed and compared with the baseline BHT-200.

The three-axis thruster was successfully operated in single, double and triple face configurations. Distinct jet plume and ball plume modes were observed. Inverted pendulum thrust stand readings in the single face mode indicated that the three-axis thruster produced considerably lower thrust, specific impulse and thrust efficiencies than the BHT-200. Beam current density measurements conducted using a guarded Faraday probe showed significant differences in plume divergence angle, total beam current and current density distributions between the different faces and different operating modes.

Results showed three-axis thruster efficiency and stability improved with more operating faces. Improvements to the three-axis thruster design and thrust stand configuration for use with the thruster were enumerated. Suggestions for refinement to experimental methodologies to optimize testing with the three-axis thruster were made and additional diagnostic techniques were described.

## *Table of Contents*

	Page
Abstract . . . . .	iv
List of Figures . . . . .	vi
List of Tables . . . . .	vii
List of Symbols . . . . .	viii
List of Abbreviations . . . . .	ix
I. Introduction . . . . .	1
1.1 Electric Propulsion . . . . .	1
1.1.1 Types of Electric Propulsion . . . . .	1
1.1.2 Hall Effect Thrusters . . . . .	3
1.2 Spacecraft Attitude Control . . . . .	4
1.2.1 Conventional Attitude Control . . . . .	5
1.2.2 Low Thrust Attitude Control . . . . .	6
1.3 Problem Statement . . . . .	7
1.3.1 Plume Impingement . . . . .	7
1.3.2 Plume/Plume Interactions . . . . .	7
1.3.3 Single Cathode Operation . . . . .	7
1.3.4 Difficulties in Three-axis Measurements . . . . .	8
1.4 Objectives . . . . .	8
II. Background and Motivation . . . . .	9
2.1 Overview . . . . .	9
2.2 Hall Effect Thrusters . . . . .	9
2.2.1 Development . . . . .	9
2.2.2 Theory of Operation . . . . .	11
2.2.3 Limitations . . . . .	14
2.2.4 Variants . . . . .	14
2.3 Hall Effect Thrusters and Attitude Control Requirements	16
2.4 Clustered Hall Thruster Research . . . . .	18
2.5 Diagnostic Techniques . . . . .	19
2.5.1 Thrust Stand . . . . .	20
2.5.2 Faraday Probe . . . . .	21

	Page
III. Methodology . . . . .	23
3.1 Overview . . . . .	23
3.2 Vacuum Facility and Support Equipment . . . . .	23
3.2.1 Vacuum Chamber . . . . .	23
3.2.2 Pumps and Pump-down Sequence . . . . .	23
3.2.3 Gauges and Pump-up Sequence . . . . .	25
3.2.4 Translation Stages . . . . .	26
3.3 Thrusters . . . . .	31
3.3.1 BHT-200 . . . . .	31
3.3.2 Three-axis Thruster . . . . .	33
3.3.3 Propellant System . . . . .	34
3.3.4 Power Processing Unit . . . . .	35
3.4 Diagnostic Equipment . . . . .	35
3.4.1 Thrust Stand . . . . .	36
3.4.2 Faraday Probe . . . . .	42
IV. Results . . . . .	51
4.1 Overview . . . . .	51
4.2 Three-axis Thruster Operation . . . . .	51
4.2.1 Plume Modes . . . . .	51
4.2.2 Propellant Utilization . . . . .	55
4.3 Thrust . . . . .	58
4.3.1 Thrust Stand Inclination Dependence . . . . .	60
4.4 Faraday Probe Results . . . . .	62
4.4.1 BHT-200 . . . . .	62
4.4.2 Single Plume Mode . . . . .	64
4.4.3 Double Plume Mode . . . . .	69
4.4.4 Triple Plume Mode . . . . .	75
V. Conclusions and Recommendations . . . . .	81
5.1 Overview . . . . .	81
5.2 The Three-axis Thruster . . . . .	81
5.2.1 Nominal Settings . . . . .	82
5.2.2 Internal Cathode . . . . .	83
5.2.3 External Cathode . . . . .	84
5.2.4 Propellant Manifold . . . . .	85
5.3 Vacuum Chamber . . . . .	86
5.3.1 Chamber Size . . . . .	86
5.3.2 Pumping Rates . . . . .	86
5.4 Thrust Stand . . . . .	87
5.4.1 Vibration Damping . . . . .	87

	Page
5.4.2 Thermal Effects . . . . .	88
5.4.3 Future Study . . . . .	88
5.4.4 Thrust Stand Modifications . . . . .	90
5.5 Faraday Probe . . . . .	93
5.5.1 Correlated Thrust Measurements . . . . .	93
5.5.2 Coverage . . . . .	93
5.5.3 Bias Correction . . . . .	94
5.6 Other Diagnostic Techniques . . . . .	95
Appendix A. Background and Theory of Suggested Further Diagnostic Techniques . . . . .	96
A.1 Langmuir Probe . . . . .	96
A.2 Electrostatic Analyzer . . . . .	98
Appendix B. Three-axis Thruster Operating Procedures . . . . .	101
Appendix C. Faraday Probe Data . . . . .	105
Bibliography . . . . .	125
Vita . . . . .	130

## *List of Figures*

Figure		Page
1.	Aerojet MR-501B Electrothermal Hydrazine Thruster (EHT) re-sistojet. . . . .	2
2.	NASA NSTAR ion thruster. . . . .	3
3.	Schematic of a magnetoplasmadynamic thruster . . . . .	4
4.	SPT-100 Hall effect thruster . . . . .	5
5.	Artist's impression of ESA's SMART-1 mission at the moon . .	10
6.	Photo of SNECMA PPS-1350 HET used on SMART-1 . . . . .	11
7.	Hall effect thruster cross section schematic, adapted from Goebel and Katz. . . . .	12
8.	Visible plasma plume of BHC-1500 Hall effect thruster during ground testing. . . . .	15
9.	A control moment gyroscope is readied for delivery to the International Space Station . . . . .	17
10.	A cluster of four BHT-200 thrusters in operation. . . . .	18
11.	SPASS lab vacuum chamber and some associated components.	24
12.	A screenshot of the Extorr VacuumPlus software interface with select species labeled. . . . .	26
13.	Rear view of thrust stand with multi-axis thruster attached mounted on Aerotech translation stage z-axis. Aluminum box frame is visible at bottom. . . . .	28
14.	Three-axis thruster mounted to translation stage via cantilever arm. Z-face is forward and propellant manifold is clearly visible.	29
15.	Box frame with cantilever arm mounted to Aerotech z-stage. Three-axis thruster is attached. . . . .	30
16.	Thrust stand with multi-axis thruster on box frame. Beam profiler radial stage and theta stage with Faraday probe are visible in foreground. . . . .	31

Figure		Page
17.	Beam profiler translation stage is in the foreground. The three-axis thruster is mounted to the Aerotech translation stage at the far end of the chamber. . . . .	32
18.	BHT-200 thruster with BHC-1500 cathode on mounting bracket.	33
19.	Three-axis thruster. . . . .	34
20.	Thrust stand with thermal jacket removed. . . . .	37
21.	Detail of thrust stand internals. . . . .	37
22.	Thrust stand with thermal jacket and wiring harness installed.	38
23.	Screenshot of thrust stand VI. Part of a calibration step curve and a BHT-200 measured thrust run are shown in the top graph.	39
24.	Three-quarter view of thrust stand with BHT-200 attached mounted on steel platen. . . . .	40
25.	Photo of Faraday probe. . . . .	43
26.	Faraday probe schematic diagram. . . . .	44
27.	Screenshot of beam profiler radial scan VI displaying results of Faraday probe scan at three different axial distances. . . . .	45
28.	Diagram of Faraday probe coverage arcs. . . . .	46
29.	Top view diagram of Faraday probe coverage arcs showing multiple coverage planes through Z-face. . . . .	47
30.	Diagram of 180 degree Faraday probe scan arc at 30cm radius.	48
31.	Three-axis thruster in operation displaying all three faces in jet plume mode. . . . .	52
32.	X-face of thruster displaying ball plume mode. . . . .	53
33.	Startup sequence displaying transition from ball to jet plumes.	54
34.	Propellant mass flow per operating thruster face. . . . .	57
35.	Thrust stand LVDT voltage as a function of inclination, BHT-200 thruster mounted. . . . .	61
36.	Thrust stand LVDT voltage as a function of inclination, three-axis thruster mounted. . . . .	61
37.	Current density for BHT-200 thruster. . . . .	63

Figure		Page
38.	Current density for BHT-200 on logarithmic scale. . . . .	63
39.	Current density for three-axis thruster, x-face. . . . .	65
40.	Current density for three-axis thruster, x-face, on logarithmic scale. . . . .	66
41.	Current density for x-face, single plume. . . . .	67
42.	Current density for y-face, single plume. . . . .	68
43.	Current density for z-face, single plume. . . . .	68
44.	Current density for x-face, x and z-faces operating. . . . .	69
45.	Current density for y-face, y and z-faces operating. . . . .	71
46.	Current density for z-face, x and z-faces operating, in plane. . .	72
47.	Current density for z-face, y and z-faces operating, in plane. . .	73
48.	Current density for z-face, x and z-faces operating, 45 degrees out of plane. . . . .	73
49.	Current density for z-face, x and z-faces operating, in plane, logarithmic scale. . . . .	74
50.	Current density for x and y-faces, double plume mode. . . . .	74
51.	Current density for x and y-face, triple plume mode. . . . .	75
52.	Comparison of current densities at 30cm for x and y-faces, double vs. triple plume. . . . .	76
53.	Comparison of current densities at 30 cm for x and y-faces. . .	77
54.	Current density for x and z-faces, triple plume mode, centered on z-face. . . . .	78
55.	Current densities for y and z-faces, triple plume mode, centered on z-face. . . . .	78
56.	Comparison of current densities at 30 cm for x-face in different operating modes. . . . .	79
57.	Comparison of current densities at 30 cm for y-face in different operating modes. . . . .	79
58.	Comparison of current densities at 30 cm for z-face in different operating modes. . . . .	80

Figure		Page
59.	Three-axis thruster anode discharge current as a function of magnet current at constant propellant flow rates. All three faces operating. . . . .	83
60.	Typical Langmuir probe I-V curve. . . . .	97
61.	Diagram of an electrostatic analyzer configuration . . . . .	98
62.	X-face: Single plume mode, 180 degree arc, 30-50 cm radii. . .	107
63.	X-face: Single plume mode, 50-100 cm radii. . . . .	107
64.	X-face: Double plume mode (x and y-faces operating), 180 degree arc, 30-50 cm radii. . . . .	108
65.	X-face: Double plume mode (x and y-faces operating), 30-100 cm radii. . . . .	108
66.	X-face: Double plume mode (x and z-faces operating), 180 degree arc, 30-50 cm radii. . . . .	109
67.	X-face: Triple plume mode, 180 degree arc, 30-50 cm radii. . .	109
68.	X-face: Triple plume mode, 30-100 cm radii. . . . .	110
69.	Y-face: Single plume mode, 180 degree arc, 30-50 cm radii. . .	110
70.	Y-face: Single plume mode, 30-100 cm radii. . . . .	111
71.	Y-face: Double plume mode (x and y-faces operating), 180 degree arc, 30-50 cm radii. . . . .	111
72.	Y-face: Double plume mode (x and y-faces operating), 30-100 cm radii. . . . .	112
73.	Y-face: Double plume mode (y and z-faces operating), 180 degree arc, 30-50 cm radii. . . . .	112
74.	Y-face: Triple plume mode, 180 degree arc, 30-50 cm radii. . .	113
75.	Y-face: Triple plume mode, 30-100 cm radii. . . . .	113
76.	Centered 45 degrees between x and y-face: Double plume mode (x and y-faces operating), 180 degree arc, 30-50 cm radii. . . .	114
77.	Centered 45 degrees between x and y-face: Double plume mode (x and y-faces operating), 30-100 cm radii. . . . .	114
78.	Centered 45 degrees between x and y-face: Triple plume mode, 180 degree arc, 30-50 cm radii. . . . .	115

Figure		Page
79.	Centered 45 degrees between x and y-face: Triple plume mode, 30-100 cm radii. . . . .	115
80.	Z-face (plane containing x-face): Single plume mode, 180 degree arc, 30-50 cm radii. . . . .	116
81.	Z-face (plane containing x-face): Single plume mode, 30-100 cm radii. . . . .	116
82.	Z-face (plane containing x-face): Double plume mode (x and z-faces operating), 180 degree arc, 30-50 cm radii. . . . .	117
83.	Z-face (plane containing x-face): Double plume mode (x and z-faces operating), 30-90 cm radii. . . . .	117
84.	Z-face (plane containing x-face): Triple plume mode, 180 degree arc, 30-50 cm radii. . . . .	118
85.	Z-face (plane containing x-face): Triple plume mode, 30-90 cm radii. . . . .	118
86.	Z-face (plane containing y-face): Single plume mode, 180 degree arc, 30-50 cm radii. . . . .	119
87.	Z-face (plane containing y-face): Single plume mode, 30-100 cm radii. . . . .	119
88.	Z-face (plane containing y-face): Double plume mode (y and z-faces operating), 180 degree arc, 30-50 cm radii. . . . .	120
89.	Z-face (plane containing y-face): Double plume mode (y and z-faces operating), 30-100 cm radii. . . . .	120
90.	Z-face (plane containing y-face): Triple plume mode, 180 degree arc, 30-50 cm radii. . . . .	121
91.	Z-face (plane containing y-face): Triple plume mode, 30-100 cm radii. . . . .	121
92.	Z-face (plane 45 degrees between x and y-face): Single plume mode, 180 degree arc, 30-50 cm radii. . . . .	122
93.	Z-face (plane 45 degrees between x and y-face): Single plume mode, 30-90 cm radii. . . . .	122
94.	Z-face (plane 45 degrees between x and y-face): Double plume mode (x and z-faces operating), 180 degree arc, 30-50 cm radii. . . . .	123

Figure		Page
95.	Z-face (plane 45 degrees between x and y-face): Double plume mode (y and z-faces operating), 180 degree arc, 30-50 cm radii.	123
96.	Z-face (plane 45 degrees between x and y-face): Triple plume mode, 180 degree arc, 30-50 cm radii. . . . .	124
97.	Z-face (plane 45 degrees between x and y-face): Triple plume mode, 30-100 cm radii. . . . .	124

*List of Tables*

Table		Page
1.	Comparison of thruster types. . . . .	2
2.	Typical performance of conventional attitude control systems .	5
3.	BHT-200 propellant mass flow at 250 V anode discharge potential.	56
4.	Three-axis thruster propellant mass flow at 250 V anode discharge potential, Y-face operating. . . . .	56
5.	BHT-200 measured thrust and derived values at 250 V anode discharge voltage. . . . .	59
6.	Three-axis thruster measured thrust and derived values at 250 V anode discharge voltage with y-face operating. . . . .	60
7.	X-face beam parameters. . . . .	65
8.	Y-face beam parameters. . . . .	66
9.	Z-face beam parameters. . . . .	69
10.	X-face beam parameters, double plume. . . . .	70
11.	Y-face beam parameters, double plume. . . . .	70

## *List of Symbols*

Symbol		Page
$I_{sp}$	Specific impulse . . . . .	4
$\vec{E}$	Electric field . . . . .	13
$\vec{B}$	Magnetic field . . . . .	13
$v_{\perp}$	Azimuthal velocity . . . . .	13
$q$	Electric charge . . . . .	13
$r_L$	Larmour radius . . . . .	13
$T$	Thrust . . . . .	20
$\dot{m}$	Mass flow . . . . .	20
$\bar{v}$	Mean velocity . . . . .	20
$P$	Power . . . . .	20
$\eta$	Efficiency . . . . .	20
$J_B$	Beam current . . . . .	21
$\theta$	Rotation angle . . . . .	27
$\Delta b_{cal}$	Calibration bias . . . . .	41
$\Delta b_T$	Thermal drift bias . . . . .	41
$\Delta b_{res}$	Resolution bias . . . . .	42
$j_B$	Current density . . . . .	43
$V$	Voltage . . . . .	43
$R$	Resistance . . . . .	43
$A_{aperture}$	Probe aperture area . . . . .	43
$\Theta$	Divergence angle . . . . .	65
$\eta_J$	Beam current utilization efficiency . . . . .	65

*List of Abbreviations*

Abbreviation		Page
EP	Electric Propulsion . . . . .	1
ESA	European Space Agency . . . . .	1
SMART	Small Missions for Advanced Research in Technology . . .	1
NASA	National Aeronautics and Space Administration . . . . .	1
MPD	Magnetoplasmadynamic . . . . .	3
HET	Hall effect thruster . . . . .	3
SPT	Stationary plasma thruster . . . . .	3
CMG	Control moment gyroscope . . . . .	5
USSR	Union of Soviet Socialist Republics . . . . .	9
US	United States . . . . .	9
PPU	Power processing unit . . . . .	10
SNECMA	Societe Nationale d'Etude et de Construction de Moteurs d'Aviation . . . . .	11
TAL	Thruster with anode layer . . . . .	16
NSSK	North-south station keeping . . . . .	16
SPASS	Space Propulsion Analysis and System Simulation . . . . .	23
ESA	Electrostatic Analyzer . . . . .	27
LVDT	Linear variable differential transformer . . . . .	36

# PERFORMANCE CHARACTERIZATION OF A THREE-AXIS HALL EFFECT THRUSTER

## I. Introduction

### 1.1 *Electric Propulsion*

Electric propulsion (EP) is an attractive technology for replacing conventional chemical rocket systems in certain cases. EP systems in general have a much higher specific impulse than chemical or cold gas expansion systems potentially leading to a large savings in propellant mass over the lifetime of a spacecraft and in some cases making mission profiles feasible which would be unobtainable with chemical rockets.

The use of electric propulsion in space applications has been a desirable goal since space flight was first seriously discussed. More recently the use of electric propulsion has been practically implemented for spacecraft requirements where low thrust and long endurance are called for. From mundane tasks, like station keeping maneuvers for telecommunications satellites, to more glamorous missions like ESA's SMART-1 mission to the moon or NASA's Deep Space 1 comet rendezvous mission, EP use is increasingly common and presents a fruitful field for current and future research.

*1.1.1 Types of Electric Propulsion.* Electric propulsion technologies are typically grouped into several classes. The main difference between types is in the method they use to accelerate the propellant. There can be a wide range of performance between different types of electric propulsion thrusters. Typical values for each as compared to chemical systems are shown in Table 1 [1].

*1.1.1.1 Electrothermal.* Electrothermal propulsion uses an electric heat source to heat propellant, similar to a chemical rocket, but capable of achieving

Type	Specific Impulse(s)	Thrust/Weight
Chemical	200-465	1-10
Electrothermal	300-1500	$< 10^{-3}$
Electromagnetic	1000-10,000	$< 10^{-4}$
Electrostatic	2000-100,000	$< 10^{-4} - 10^{-6}$

Table 1: Comparison of thruster types.

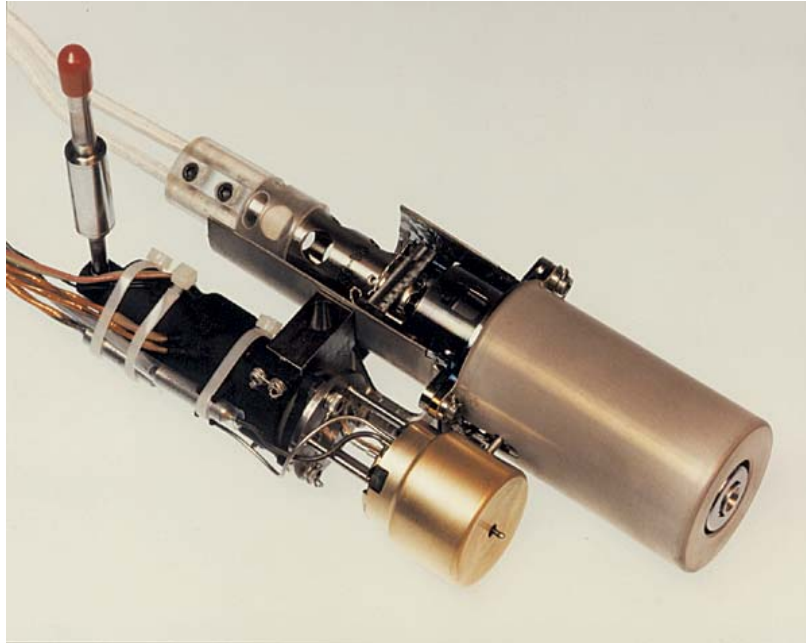


Figure 1: Aerojet MR-501 Electrothermal Hydrazine Thruster (EHT) resistojet, image courtesy of Aerojet [2].

much higher temperatures. Examples of electrothermal propulsion are the resistojet, which uses a resistive heating element, and the arcjet, which uses an electrical arc to directly heat the propellant. Both of these examples are mature technologies which have been used in space [3].

*1.1.1.2 Electrostatic.* Electrostatic propulsion systems use an electric field to accelerate particles. Thrust is provided directly by a momentum transfer from the ejected particles. The most common example of this type is the gridded ion thruster, in which ions are accelerated by a potential difference between screen and accelerator plates at the exit of the thruster. In general the terms *ion thruster* and

*gridded ion thruster* are used interchangeably. A gridded ion thruster was used on the Deep Space 1 probe previously mentioned as well as the current NASA Dawn mission. Other examples of this type include colloid thrusters where very fine droplets of liquid are accelerated by an electric field [4].



Figure 2: NASA NSTAR ion thruster, from NASA Glenn Research Center [5].

*1.1.1.3 Electromagnetic.* Electromagnetic thrusters use a magnetic field or the interaction between electric and magnetic fields to accelerate the propellant. An example of this type is the magnetoplasmadynamic (MPD) thruster in which a plasma is accelerated by the Lorentz force created by an electric field and its induced magnetic field. MPD thrusters potentially offer better performance than other types but their high power requirements and other issues require further development before they can be flown in space [6].

*1.1.2 Hall Effect Thrusters.* Hall effect thrusters (HET), also known as stationary plasma thrusters (SPT) or sometimes gridless ion thrusters, are the subject



Figure 3: Schematic of a magnetoplasmadynamic thruster, from NASA Glenn Research Center [7].

of this thesis. HET are sometimes categorized as electromagnetic thrusters since their operation requires both an electric and magnetic field, but are more correctly considered electrostatic thrusters since only the electric field is used to accelerate the propellant.

HET are attractive because of their combination of high  $I_{sp}$  (compared to chemical thrusters) and high thrust (compared to other types of electrostatic thrusters). The SMART-1 mission to the moon was equipped with an HET and they have been used on over 140 spacecraft to date, primarily for station keeping duties [8].

## ***1.2 Spacecraft Attitude Control***

Although present use of electric thrusters is concentrated in the areas of station keeping, drag makeup, etc., a potential application is for spacecraft attitude control. Use of chemical propellant thrusters for attitude control is normally limited by the propellant mass required for the thruster system. Electric systems can offer higher specific impulse and smaller impulse bits than chemical systems, providing not only more precise control, but also better propellant utilization efficiency over the operational life of the spacecraft [10].

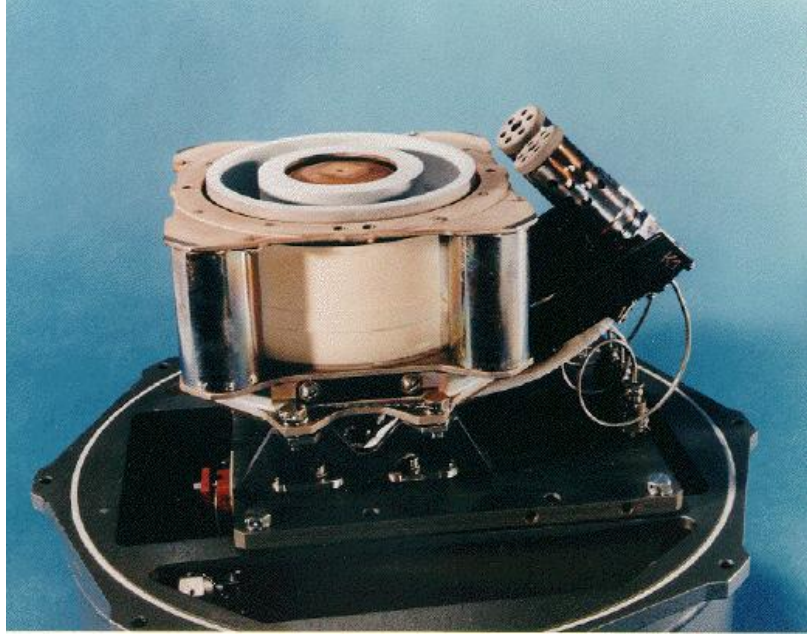


Figure 4: SPT-100 Hall effect thruster [9].

*1.2.1 Conventional Attitude Control.* Conventional spacecraft attitude control systems use some form of chemical rocket or cold gas thrusters to perform impulsive maneuvers. These systems are effective, but require a large additional propellant mass especially if a mission requires frequent or large maneuvers.

Actuator	Performance Range	Weight (kg)	Power (W)
<i>Thrusters</i>			
Hot Gas(Hydrazine)	0.5 to 9000 $N$	Variable	N/A
Cold Gas	< 5 $N$	Variable	N/A
Reaction and Momentum Wheels	0.4 to 400 $N \cdot m \cdot s$ for momentum wheels at 1200 to 5000 rpm; max torques from 0.01 to 1 $N \cdot m$	2 to 20	10 to 110
Control Moment Gyros (CMG)	25 to 500 $N \cdot m$ of torque	> 10	90 to 150
Magnetic Torquers	1 to 4000 $A \cdot m^2$	0.4 to 50	0.6 to 16

Table 2: Typical performance of conventional attitude control systems, adapted from Larson [3].

Reorientation of spacecraft is often achieved by using momentum wheel or control moment gyroscope (CMG) systems which do not require expendable propellant.

Momentum wheels operate by changing the rotational speed of a wheel which then imparts an angular velocity to the spacecraft around the axis of the wheel. They must be used in combination to provide a multi-axis change. CMG systems use a gimbaled gyroscope which pivots to provide an angular momentum. A two gimbal CMG can provide three-axis rotation with only one wheel [11].

Although these angular momentum systems are attractive in that they do not require additional propellant mass, under a constant external force they can become saturated. They can only absorb a certain amount of externally applied moment before they reach their operating limit. At this point they must be unloaded by an impulsive thrust system in a “momentum dump” maneuver. For this reason, most spacecraft typically have a combination of impulsive and momentum based systems [12].

*1.2.2 Low Thrust Attitude Control.* Low thrust propulsion systems like EP can be justly used as the reactive component of an attitude control system. HET are already utilized in a dual role on some spacecraft to provide thrust for both station keeping and momentum dump maneuvers [13]. The use of EP to provide for momentum unloading is highly attractive since it reduces the total propellant mass required compared to a lower  $I_{sp}$  system.

It should also be possible to completely replace a conventional three-axis reactive control system with a low thrust EP system. Given the lower thrust of an EP system a given maneuver would take a longer amount of time to complete, but the reduced expenditure of propellant may be more desirable in some situations.

An EP system for attitude control would most likely take the form of a gimbaled thruster. The system could reorient its thrust axis in the direction required. A combination of multiple thrusters oriented orthogonally to each other, in the familiar configuration of a conventional reaction control system will reduce the complexity of the system and provide a much more robust capability. Such a three-axis configuration of HET is the subject of this thesis.

### ***1.3 Problem Statement***

The basic premise of a three-axis HET attitude control thruster being feasible, there are still certain obstacles to integrating such a system with a practical spacecraft. All of the same issues that are present with normal HET operation are still in play, while the three-axis arrangement presents new issues and complicates existing ones as well. Assuming the power and propellant requirements for a three-axis thruster are similar to existing HETs, the main problems arise with the plume orientation and interactions.

*1.3.1 Plume Impingement.* The plasma plume of an HET presents a potential hazard to surfaces of the spacecraft that are exposed to it. High energy ions can cause erosion due to sputtering on some surfaces and deposition on others. These effects may cause degradation of spacecraft systems, especially solar arrays. The obvious solution is to orient the thruster plume away from sensitive areas and to avoid the spacecraft entirely if possible.

Plume impingement on spacecraft surfaces can also create moments due to the collisions of the ions. These moments must be counteracted by the attitude control system and must be factored into the system design. Proper characterization of the plume geometry is essential, especially since HET plumes are typically divergent.

*1.3.2 Plume/Plume Interactions.* Operating multiple HET in close proximity can potentially cause interactions between the plumes and thrusters. In a case where these thrusters are integrated into a single unit and share components this concern is even greater. It is important to determine how the operation of each thruster affects the others.

*1.3.3 Single Cathode Operation.* Typically, an HET has its own cathode to neutralize the plasma plume. With multiple thrusters operating on a single cathode it will be necessary to determine the effectiveness of this configuration or if a different cathode arrangement might be more effective.

*1.3.4 Difficulties in Three-axis Measurements.* Most studies of HET have focused on single thrusters or clusters of thrusters with a common thrust axis. Diagnostic procedures for these types of measurements are fairly well established. Taking measurements of multiple thrusters which have mutually orthogonal thrust axes is potentially problematic and may require different techniques or special considerations.

#### **1.4 Objectives**

With these problems in mind, the broad objectives of this research are to characterize the overall performance of the thruster and the nature of the plasma plumes. Since this is the first time a three-axis thruster will be operated in a test environment well established techniques are preferred. This leads to three primary goals:

1. Successfully operate a three-axis Hall effect thruster in a laboratory environment. This goal includes operating the thruster in single, double and triple face modes. This goal also includes developing methods for integrating a three-axis thruster into existing HET test bench configurations and devising a standard operating procedure for its use.
2. Take thrust measurements in both single and multi thruster operating modes. From direct thrust measurements the specific impulse and thrust efficiency can be calculated and compared to current HETs. These metrics provide the best measure of the overall performance of the three-axis thruster.
3. Take Faraday probe measurements of the plume to characterize the current density. The current density can then be used to calculate the total beam current and plume divergence angle as indicators of the beam efficiency of the thruster. The general shape of the plume can be determined from the current density distribution and the divergence angle to simplify spacecraft integration and identify plume/plume interactions.

## II. Background and Motivation

### 2.1 Overview

This chapter provides background information on the physics and operation of Hall effect thrusters and spacecraft attitude propulsion systems. The operating principles of the diagnostic techniques used in the research are also described. In the process a literature review of previous research in the fields of HET plume characterization is performed.

### 2.2 Hall Effect Thrusters

*2.2.1 Development.* The use of HET for applications in spaceflight has been described since the early days of practical spaceflight as a promising technology in electric propulsion [14]. HET research was begun by the space programs of both the United States and the Soviet Union at the same time, but only in the USSR was the technology further developed. In the US the identification of inefficiencies in HET systems operating at high power and the superior  $I_{sp}$  performance of gridded ion thrusters led to the latter being the favored technology.

While HET technology was being largely ignored in the US in favor of ion thrusters, development continued in the USSR through the 1960s and 70s and were successfully tested on spacecraft as early as 1972 [15]. Due to the lack of communication between the countries' space agencies HET development continued to be neglected in the US in favor of higher power or higher  $I_{sp}$  systems [16]. In recent years however the availability of Russian data on HET development and operation has spurred Western research in design and performance of HETs.

The higher relative thrust of HET systems combined with their higher efficiencies at low power make them desirable for a number of space applications, particularly station keeping and orbital maneuvers. HETs have traditionally been thought of as being heavily outclassed by ion thrusters for long duration missions requiring a high  $I_{sp}$ , such as interplanetary profiles. Recent successes by missions employing relatively low powered EP systems such as SMART-1 have proven their capability and some-

what disproved this view. High power Hall thrusters are now being considered as a viable alternative for future missions. The recent ESA SMART-1 probe conducted a transit to the moon operating on a single HET and set a number of duration records for HET operation in space [17].

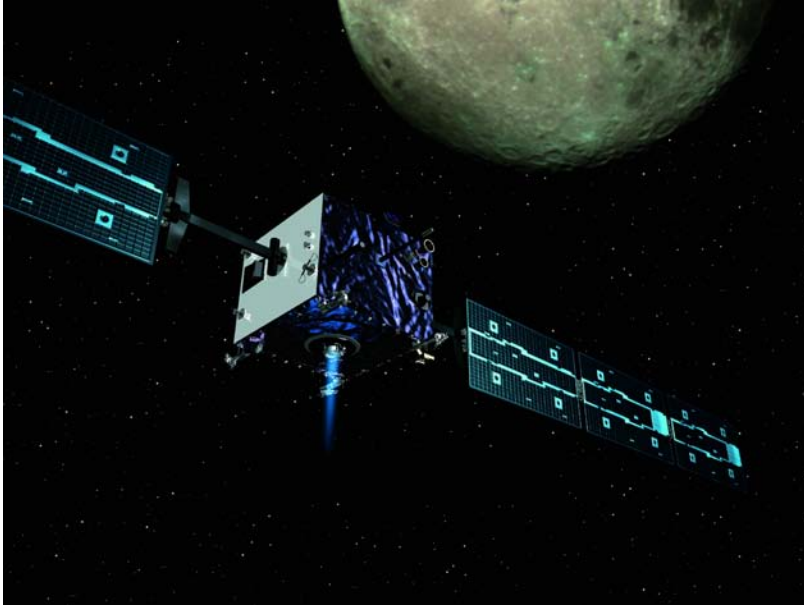


Figure 5: Artist's impression of ESA's SMART-1 mission at the moon, image credit:ESA-AOES Medialab [18].

HETs may have other system integration advantages over ion thrusters and other types of electric propulsion due to their simplified power processing requirements. This difference is a non-trivial distinction when one considers that the power processing unit (PPU) is often the most massive and most expensive component of an EP system [6]. For many reasons, HETs are now considered one of the most important electric propulsion development fields for the near future [19–21].

SPT-100 thrusters, produced by the Russian Fakel design bureau, and its derivative models have flown over 7500 hours in space [22]. The first US built HET to fly in space was the Busek BHT-200 on TacSat-2 [23]. HETs continue to be a favored option for geostationary satellites [24].

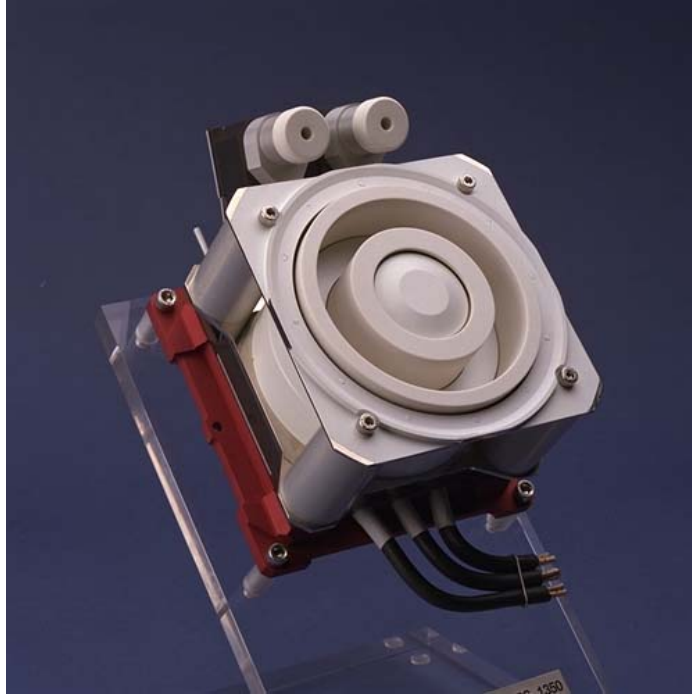


Figure 6: Photo of SNECMA PPS-1350 HET used on SMART-1, image credit:ESA [18].

*2.2.2 Theory of Operation.* At its simplest, Hall thrusters are electrostatic propulsion devices which operate by accelerating ions of a propellant, typically xenon, by an electric field. Thrust is thus generated by the accelerated ion beam, as in gridded ion thrusters. The ionization process and electric field creation however are quite a bit different in HETs than ion thrusters.

A typical HET is composed of a cylindrical channel with an anode and propellant inlet on the inboard end and a series of permanent or electromagnets lining the outboard end. The magnets produce a radial magnetic field which is perpendicular to the channel at a given point. Generally, a cathode is mounted external to the HET which is used to produce electrons. Some of these electrons are attracted to the anode, which is biased positive, and enter the channel. As the electrons enter the magnetic field at the mouth of the channel they begin to move azimuthally around the channel due to the *Hall effect*, whereby these devices get their name.

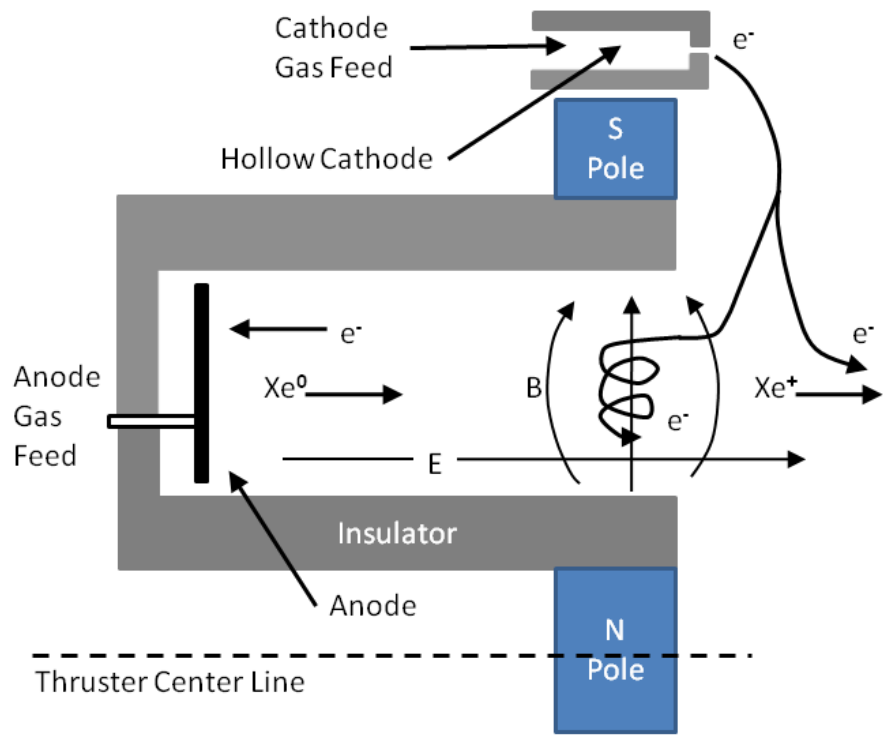


Figure 7: Hall effect thruster cross section schematic, adapted from Goebel and Katz [25].

This Hall current is induced by the interactions between the axial electric ( $\vec{E}$ ) and radial magnetic ( $\vec{B}$ ) field near the mouth of the channel. This configuration creates a force on the electrons in the channel in the  $\vec{E} \times \vec{B}$  direction, i.e. the azimuthal direction. In this configuration of radial magnetic and axial electric fields the radial centrifugal force experienced by the electrons is counteracted by the increasing magnetic field strength near the wall [25]. This creates a situation in which the electrons circle the channel, sometimes called *closed drift* leading to HETs sometimes being referred to as *closed drift thrusters*.

Due to the Lorentz force on the electrons created by their azimuthal velocity ( $v_{\perp}$ ) and the ( $B$ ) field they will also gyrate in the direction of their ( $v_{\perp}$ ). The radius of this gyration is called the *Larmour radius*. The Larmour radius is given in Equation 1 where  $q$  is the charge of the particle, in this case an electron charge.

$$r_L = \frac{mv_{\perp}}{qB} \quad (1)$$

The depth of the channel on an HET is chosen so that it is substantially greater than  $r_L$  which allows the electrons to be ‘magnetized’. This means that their progress axially towards the anode is impeded and they are held in the magnetic field near the mouth of the channel. Gradually the electrons make their way to the anode via collisions with other particles and the walls, and this is of course necessary to maintain the anode current in the device [25].

Propellant, which is fed in from near the anode is ionized by collisions with these high speed electrons near the mouth and are then accelerated by the electric field away from the thruster. The propellant particles and ions are not affected by the magnetic field in the same way as the electrons due to their much higher mass and the electric field forces are dominant. Their Larmour radius is much greater than the channel depth so that they are accelerated away before their trajectory changes to any great extent. As the ions move away from the spacecraft they are neutralized by additional electrons, typically from the same cathode neutralizer used to supply

ions for ionization. This neutralization is necessary to prevent a charge buildup on the spacecraft and the eventual back streaming of propellant particles [4].

Xenon is the most common choice of propellant for HETs due to its high atomic weight (and therefore, high thrust production) and low ionization potential. HETs are not limited to xenon as a propellant however, and research continues on using alternate propellants like krypton and bismuth [21, 26].

*2.2.3 Limitations.* It is this plasma plume containing high energy particles that can also be a great source of integration problems with HETs. A plasma plume which impinges on parts of a spacecraft can cause erosion or deposition effects which can damage or degrade components. This effect can also cause a charge accumulation on the spacecraft leading to further problems. The plasma plume can also cause interference with communications systems which can be especially troubling since communications satellites are one of the prime applications for HET use. Additionally, HET plumes tend to be more highly divergent than other types of EP. For these reasons much research has been devoted to the proper characterization of thruster plumes and their effects on spacecraft [13, 27–35].

The effects of the plasma plume are not limited to other structures on the spacecraft. Sputtering erosion from the plume gradually widens the mouth of the thruster and can erode the cathode assembly as well [36, 37]. This effect is the primary failure mode for current designs of HET [38] and provides another reason why ion thrusters are often considered preferable for very long duration missions requiring continuous thrust.

*2.2.4 Variants.* There are two main types of HET, which both operate on the principles above. The most common type has a channel wall of dielectric material (most often boron nitride) which is designed to limit the sputtering erosion caused by the ions. This type of thruster is also known as a *stationary plasma thruster* or SPT from the Russian literature. The other type of thruster also goes by its adapted



Figure 8: Visible plasma plume of BHC-1500 Hall effect thruster during ground testing.

Russian name of *thruster with anode layer* or TAL. This type of HET has metal walls and a much shallower channel than the SPT type. The primary differences in operation of these two types derives from the lower rate of secondary electron emission from the dielectric walls versus metal walls [39]. The three-axis thruster evaluated in this research is of the SPT type. Although it should be possible to construct a three-axis thruster based on the TAL design, such a thruster does not currently exist and the TAL type will not be considered further here.

Additional variations and modifications of the SPT type are a field of prolific research. Cathode type and placement have been investigated [9] as well as alternate means of plume neutralization [40]. Miniaturized cylindrical HETs have been investigated at Princeton University Plasma Physics Laboratory [41, 42], as well as magnetic thrust vectoring by Garrigues, et al. [43], but most current development is devoted towards higher power thrusters producing greater thrust. There are currently two fields of concurrent research on high thrust HETs, one devoted to creating high power monolithic thrusters and the other exploring clusters of lower power thrusters with a common thrust axis [44]. There has been little to no research to date on developing or testing multi-axis Hall thrusters.

### ***2.3 Hall Effect Thrusters and Attitude Control Requirements***

Electric propulsion on current spacecraft has been used for an array of functions including north-south station keeping (NSSK), orbit raising and orbital phasing [6]. In these situations the thruster is being used as a primary thruster and not for attitude control per se. In some cases HETs have also been used in conjunction with momentum wheel systems to provide for momentum dump capability.

A three-axis (or other multi-axis configuration) Hall effect thruster configuration would have the same advantages over a multi-axis conventional system for attitude control as it displays as a primary propulsion system. The main disadvantages to using such a system would be in the increased thrust time required to generate a required moment and the aforementioned plume interaction with the spacecraft. In most cases

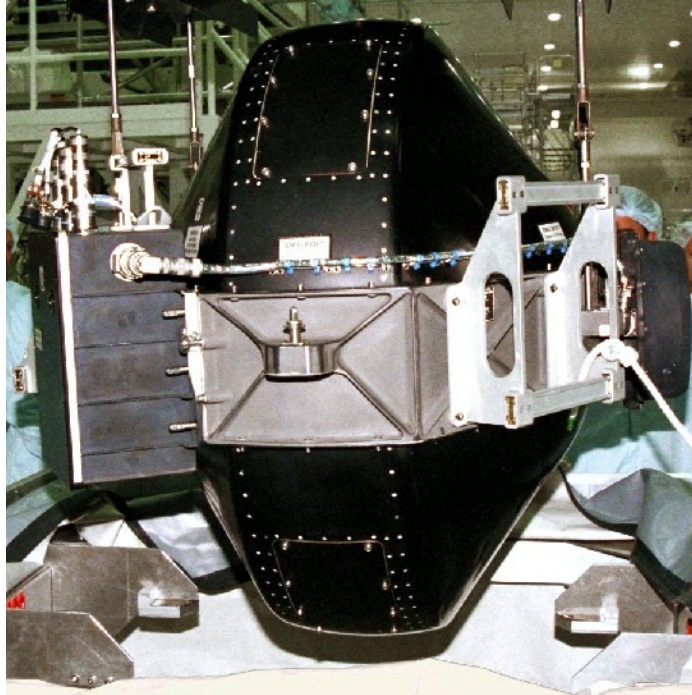


Figure 9: A control moment gyroscope is readied for delivery to the International Space Station, from NASA Kennedy Space Center [45].

attitude control maneuvers are not time critical and the low thrust provided by the HET can be favorable in situations where a small impulse is needed for vernier control or fine tuning [3]. HET attitude control could also potentially be operated in either a continuous thrust or pulsed mode to further quantize the thrust produced.

Plume interactions with the spacecraft can be minimized by proper placement of the thruster assembly. Current gimballed systems may be limited in their range of operation by the plume axis, whereas a fixed, multi-axis system may offer more flexibility. One possible solution is to place the thruster assembly on a boom or mast away from the main spacecraft structure to minimize plume impingement. This configuration has the added advantage of increasing the moment arm of the thruster thereby magnifying the effect of the thrust.

Multiple multi-axis thruster assemblies on different parts of the spacecraft could provide full three-axis attitude control. For small spacecraft or higher powered thrusters

these assemblies could be used in conjunction to provide true multi-mode operation for both fine attitude control and main propulsion.

Use of HET for attitude control of course does not preclude the use of other systems in tandem to provide improved response for a given mission requirement. HET attitude control thrusters paired with momentum wheel or control moment gyro systems may in fact be an ideal combination of complimentary systems.

#### ***2.4 Clustered Hall Thruster Research***

Although three-axis HETs have not been investigated to this point, there has been a great deal of research into operating clusters of HETs by Beal, Lobbia, Galimore, Victor and others [46–49]. The data produced by these studies is useful in understanding the operation of multiple thrusters in close proximity. The main potential problems that arise when operating multiple thrusters is the possibility of plume interactions between thrusters (cross-talk interactions) and the operation of multiple thrusters from a single cathode.



Figure 10: A cluster of four BHT-200 thrusters in operation [47].

In this case cross-talk is expected to be less of concern since the plume of each thruster is orthogonal to the others. The three-axis thruster does share common internal components between the three thruster faces. This configuration presents the possibility of some type of interaction between the thrusters as a result. It will also be interesting to examine the region between adjacent plumes, as this off-axis region is known to contain a high amount of low energy ions caused by charge exchange collisions with the main plume. The operation of adjacent thrusters in which this off-axis area overlaps may be expected to produce a higher density of such charge exchange ions there.

Operation of the three-axis thruster with a single cathode is potentially more problematic than the adjacent plume interactions. Although it has been demonstrated that multiple thrusters can operate on a single cathode, even one displaced from the thruster by a distance, the unusual geometry of the three-axis thruster may cause additional complications. In particular, the fact that the cathode is located further from each thruster face than in a typical HET and is oriented  $45^\circ$  off axis from each in addition is a concern.

One factor encountered in the clustered thruster research is expected to directly translate to the three-axis thruster. The increased back pressure in the vacuum chamber caused by multiple thrusters operating simultaneously has been shown to cause an increase in measured thrust due to increased collisions with ambient particles [50]. This effect is something that will have to be considered when taking thrust measurements with multiple thruster faces operating. Since each of the thrusters is relatively low power it is expected that this back pressure effect will be less apparent than in those studies conducted with higher power or larger clusters of HETs.

## ***2.5 Diagnostic Techniques***

Diagnostic techniques expected to be used in this research are a thrust stand and Faraday probe. These techniques are both established diagnostic tools for characterizing the performance of HETs. Well established techniques are preferred since

the novel nature of the three-axis thruster introduces its own difficulties in testing. One of the goals in conducting this research is to determine how these difficulties may affect the measurement techniques and how they can be mitigated.

*2.5.1 Thrust Stand.* Since a Hall effect thruster is, in fact, a *thruster* the most important aspect of the performance of an HET from the attitude control perspective is the amount of thrust it can produce. Thrust stand measurements allow direct observation of the overall performance of the thruster in terms of the amount of thrust that can be delivered to the spacecraft. Besides being useful for determining the spacecraft attitude control dynamics and thruster placement, thrust is also necessary to determine a number of performance criteria [51].

Given thrust  $T$ , and mass flow  $\dot{m}$ , one can calculate both mean propellant exit velocity  $\bar{v}$ , and specific impulse  $I_{sp}$ .

$$\bar{v} = \frac{T}{\dot{m}} \quad (2)$$

$$I_{sp} = \frac{T}{\dot{m}g} \quad (3)$$

Given the total system power of the thruster  $P$ , one can also calculate the thrust efficiency  $\eta$  [51].

$$\eta = \frac{T^2}{\dot{m}g_o} \quad (4)$$

Note that  $P$  here includes *all* power required to operate the thruster, including what may be required for cathode operation and generation of a magnetic field. This thrust efficiency is an overall number and there are quite a few methods of calculating efficiency and losses for individual components and processes [52].

A pendulum type thrust stand is typically used with electric propulsion thrusters because they are better suited to taking measurements in the low thrust (mN) range

exhibited by low power EP devices like Hall effect thrusters. The conventional hanging pendulum configuration is simple and stable, but requires a long moment arm for high sensitivity. Due to the space constraints of most vacuum chambers they are generally used only for higher thrust to weight EP devices.

Inverted pendulum thrust stands are more sensitive than hanging pendulum stands and are widely used for electric propulsion applications. Their stability is highly dependent on the stiffness of the springs and flexures used to support the stand. If the stiffness of these flexures changes during testing, as is often the case due to heating or other effects, the stand sensitivity can change [53]. For this reason, they are most often actively cooled and allowed to reach thermal equilibrium before taking measurements. Additionally, frequent stand calibrations during testing can be used to decrease uncertainty in measurements [54].

*2.5.2 Faraday Probe.* Essentially, a Faraday probe is a metal plate used to measure the ion current at a point in the plasma. When ions strike the probe electrons move to the collector plate which is measured by the probe as the ion current. In order to prevent plasma electrons from striking the plate and thereby artificially lowering the measured probe current many Faraday probe designs incorporate a guard ring or housing which is biased negative to repel electrons. The housing then has a small aperture which allows ions to enter and strike the collector plate. The current value is determined by measuring the voltage drop across a resistor which separates the collector plate from the ground. The enclosure or guard ring values are not measured, only the collector plate. The beam current is then found via Ohm's law and the known area of the aperture.

By taking measurements of the beam current density at various off-axis angles the total beam current,  $J_B$ , can be determined by integrating over the beam as shown in Equation 5. Faraday probes are usually swept at a constant radius from the thruster face through a range of angles to obtain the types of measurements needed for this calculation.

$$J_B = 2\pi r^2 \int_0^{\frac{\pi}{2}} j(\theta) \sin \theta d\theta \quad (5)$$

This value can then be used to determine the half-angle plume divergence, which is the angle relative to thruster centerline which contains 95% of the beam current [35].

Faraday probes in various forms are a standard tool used to characterize the beam current and plume divergence of EP plasma plumes. A source of potential error in such measurements is the effect of secondary electron emission as the result of ion bombardment of the collector plate. Secondary electrons would reduce the amount of ion current measured by the probe. For this reason, Faraday probe collector plates are usually covered in materials that have low secondary electron emission rates, such as tungsten.

Another error source in Faraday probe measurements is the effect of charge exchange ions. When the high speed plume ions collide with background neutrals a charge exchange occurs without a significant momentum transfer. This means that a fast moving neutral and a slow moving ion result from this collision. These charge exchange ions are creating moving in random directions and can compose a large proportion of the current measured by the Faraday probe, especially at large angles off-axis [46]. Methods exist to selectively exclude these low speed charge exchange ions, such as gridded Faraday probes, but these are not considered in this work.

## III. Methodology

### 3.1 Overview

In this chapter the methodology of the experiment is detailed along with specific equipment used and the manner employed. A description of the vacuum facility and support equipment is provided as well as the test configuration of the three-axis thruster and the baseline BHT-200 thruster used for comparison. The procedures used to collect and reduce experimental data are enumerated for both the thrust stand and the Faraday probe. The methods used to capture the raw data and quantify error are described. The procedures for calculating derived values from the data are also delineated.

### 3.2 Vacuum Facility and Support Equipment

The experimental work and data collection for this thesis was conducted wholly at the AFIT Space Propulsion Analysis and System Simulation (SPASS) laboratory. The SPASS lab contained the largest vacuum facility at AFIT and was capable of producing vacuum levels in the order of  $10^{-8}$  torr.

*3.2.1 Vacuum Chamber.* The primary fixture of the SPASS lab was the 2.5 meter long by 1.8 meter diameter vacuum tank. This tank enclosed an approximate volume of 6.5 cubic meters. It was produced and installed by PHPK of Columbus, Ohio. This tank was the centerpiece of the SPASS lab and has been used extensively for research on Hall effect thrusters and other electric propulsion thrusters.

*3.2.2 Pumps and Pump-down Sequence.* The first phase of pump down used a Leybold Trivac D65B mechanical roughing pump to reduce the chamber pressure to approximately 100 millitorr. The main battery of pumps consisted of five cryogenic pumps, one of which activated and began cooling when the pump cycle was initiated. The remaining four pumps activated at or around the roughing pump crossover pressure when the cryopump valves were opened to reduce chamber pressures to minimum operating levels. The roughing pump was automatically deenergized at this point.

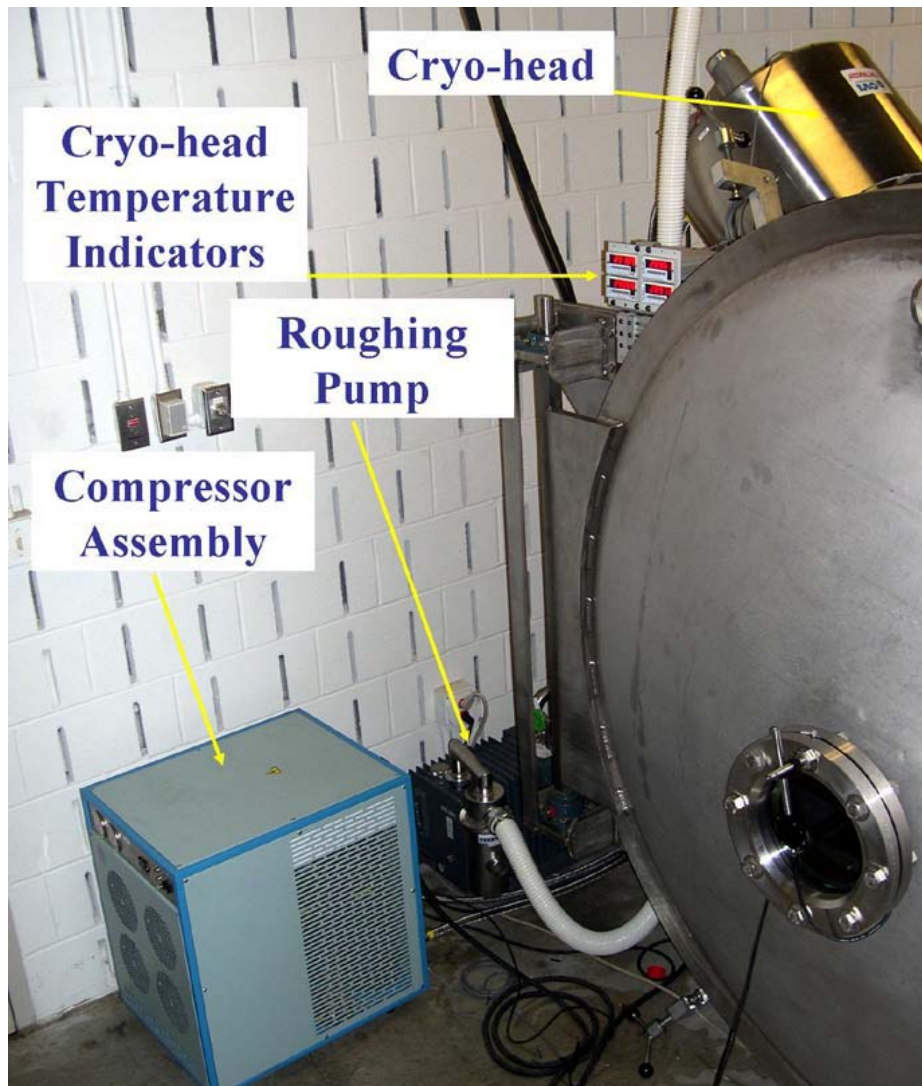


Figure 11: SPASS lab vacuum chamber and some associated components.

The main battery of cryogenic pumps were 0.5 meter diameter CVI Torr Master TM500 pumps. They were liquid helium cooled and operated at 15 to 20 Kelvin. The pump cryo-heads were mounted to the vacuum tank overhead and were individually connected to CVI CBST 6.0 scroll compressor units via flexible tubing. The pumps were capable of pumping 4000 liters per second of xenon gas per unit which typically resulted in a chamber pressure of around  $10^{-6}$  torr with a low power Hall effect thruster operating on xenon propellant [55] [56].

The fifth cryo-pump was a CVI Torr Master TM250 which began cooling upon activation of the pump down system. It was separated from the tank by a gate valve which opened automatically at tank crossover pressure. This pump had roughly half the pumping capacity of the main battery pumps, but it began removing gases as soon as the crossover pressure was reached while the main pumps still required time to cool. This decreased the amount of time required to pump down from crossover pressure to operating pressure [57].

*3.2.3 Gauges and Pump-up Sequence.* Chamber pressure monitoring and control of vacuum pumps was accomplished using a combination of two gauge systems. The first was used when tank pressures were above 0.1 millitorr and consisted of a Lesker 300 Series Convection vacuum gauge. This gauge utilized a convection-enhanced Pirani gauge to measure pressure and was used by the pump system to recognize roughing pump crossover pressure [58].

For high vacuum operating pressures an Extorr XT Series Residual Gas Analyzer (RGA), model XT100 was used for pressure readings. The RGA sensor package contained a Pirani gauge, a hot cathode ion gauge and a quadropole gauge to provide pressure readings down to  $10^{-11}$  torr. Extorr VacuumPlus software was used to control and monitor the RGA.

The software enabled a continuous readout of tank pressure using the Pirani gauge above 0.1 millitorr, the ion gauge below  $10^{-2}$  torr and the quadropole gauge below  $10^{-3}$  torr. The computer display provided a graph of gas partial pressures

in the tank reported by molecular weight. This was useful in identifying leaks or contaminants in the chamber [58].

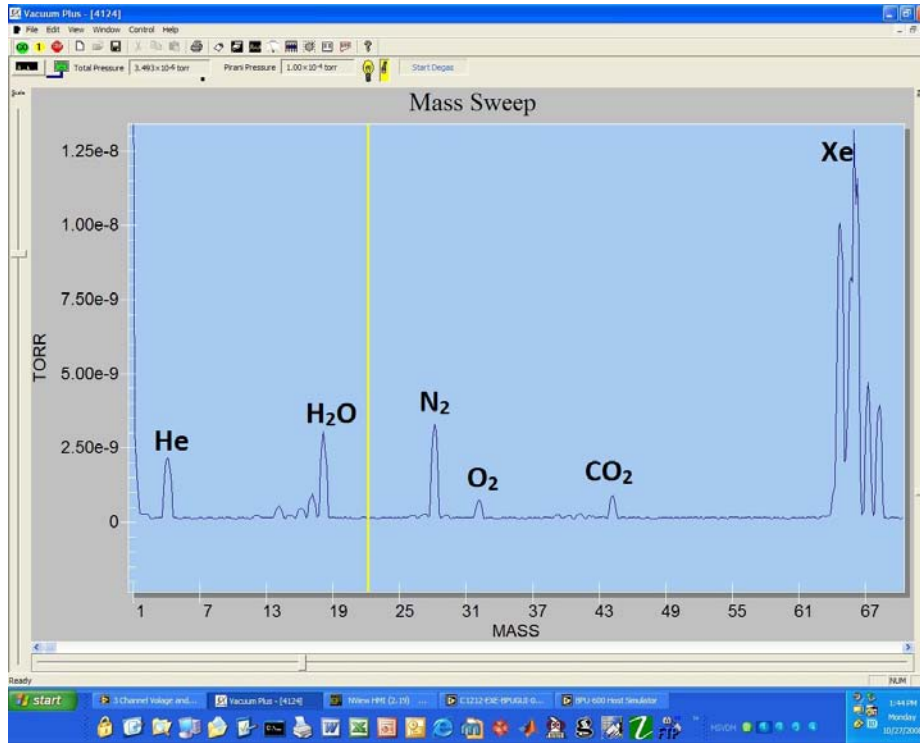


Figure 12: A screenshot of the Extorr VacuumPlus software interface with select species labeled.

The vacuum chamber was restored to atmospheric pressure by back filling with dry nitrogen. This helped to prevent contaminants from poisoning the cathodes and prolonged the life of the equipment. Nitrogen was provided from a low pressure tap off of the laboratory building's nitrogen system, which in turn was fed via a compressor and nitrogen generator.

*3.2.4 Translation Stages.* Two translation stage systems were used to manipulate the position of both the thruster and the Faraday probe inside the tank. Previous attempts to use one or the other stage resulted in incomplete coverage due to the physical limitations of stage travel and the tank dimensions. By using both stages in combination full 180 degree coverage of the thruster was achieved in a single, continuous scan.

Thrusters and the thrust stand were mounted to a three-axis Aerotech translation stage system. The system provided translation for each axis in a 60 centimeter range with a sub-millimeter precision and variable rate. The system provided for the use scripts to run pre-sequenced programs, but was used in the manual mode only for this research. The system was computer controlled via an Aerotech A3200 motion controller.

The thrust stand was attached to the Aerotech stage using a box frame constructed of 80/20<sup>®</sup> aluminum for preliminary tests. The same box frame was used to mount a cantilever arm on which the thruster was carried for later Faraday probe measurements. Some configurations of the thrust stand and mounting frames prevented full motion of the translation stage due to interference with the tank walls or other equipment in the tank.

The second translation stage was part of a beam profiler system that was designed and constructed at Colorado State University. It had two linear translation stages (axial or “z” and radial or “r”) and a rotational stage ( $\theta$ ). Linear stages were capable of motion in a one meter range and the radial stage could execute 180 degrees of rotation. Combined with a custom designed LabView software controller the beam profiler stage was capable of performing a number of automated scan profiles within a given plane. For this research it was used to conduct constant radius scans over an arc while maintaining Faraday probe orientation toward the center of the thruster [59]. The beam profiler system was capable of being used with either a Faraday probe, ExB probe or electrostatic analyzer (ESA). For this research only the Faraday probe was used.

The stepper motors used by the beam profiler system were water cooled while in vacuum. Cooling water to the beam profiler stages was provided by a Thermo Scientific NESLAB RTE7 chiller via a passthrough from outside the chamber. This was the same chiller that was used to provide cooling water to the thrust stand cooling jacket.

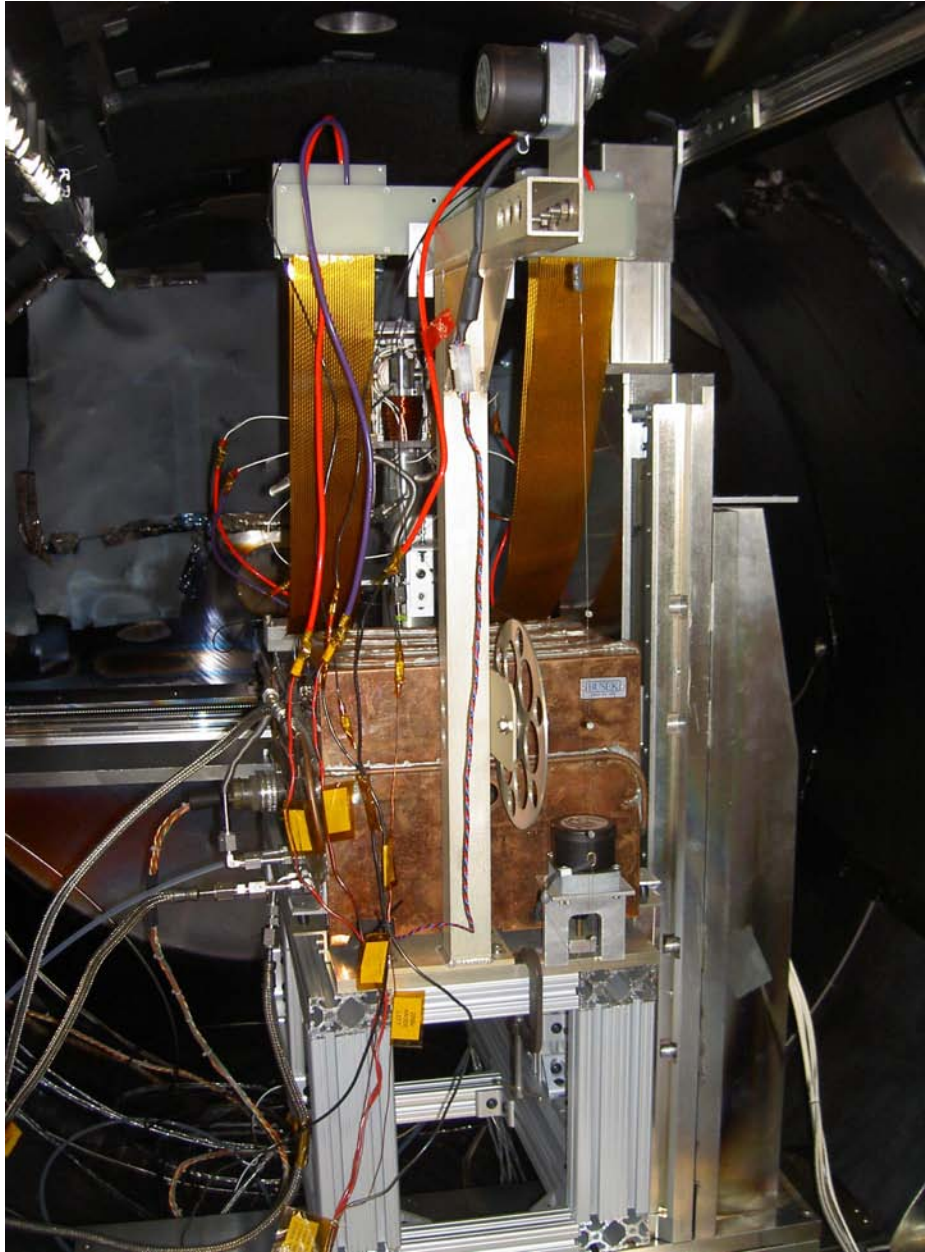


Figure 13: Rear view of thrust stand with multi-axis thruster attached mounted on Aerotech translation stage z-axis. Aluminum box frame is visible at bottom.

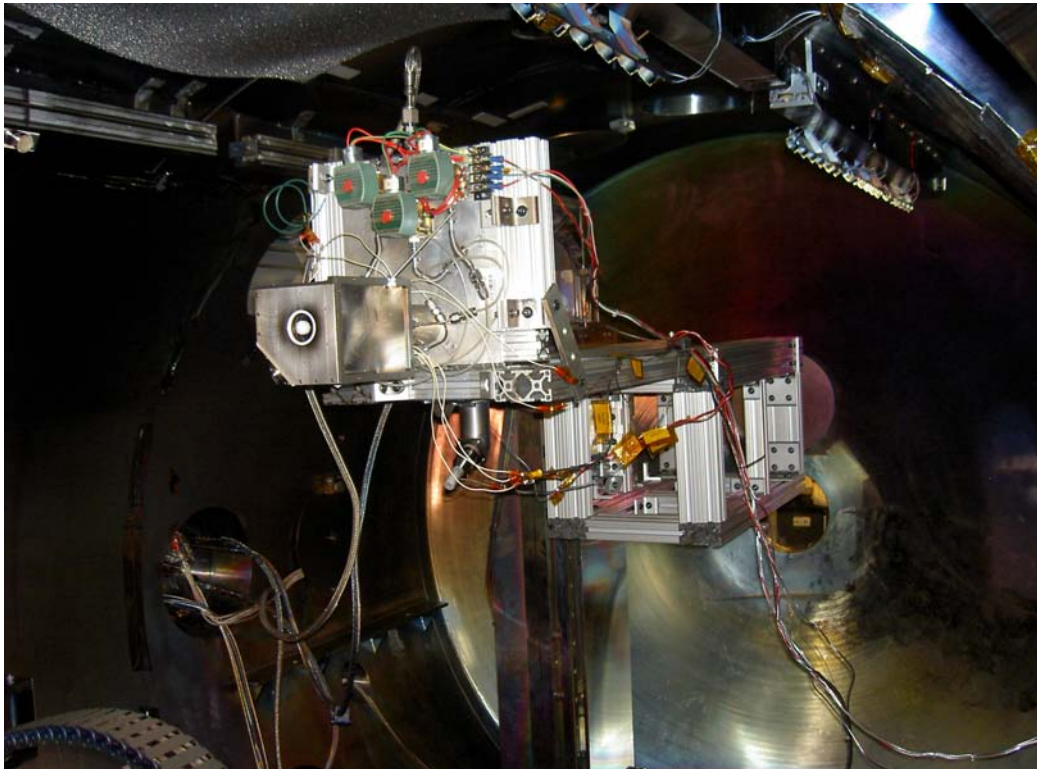


Figure 14: Three-axis thruster mounted to translation stage via cantilever arm. Z-face is forward and propellant manifold is clearly visible.

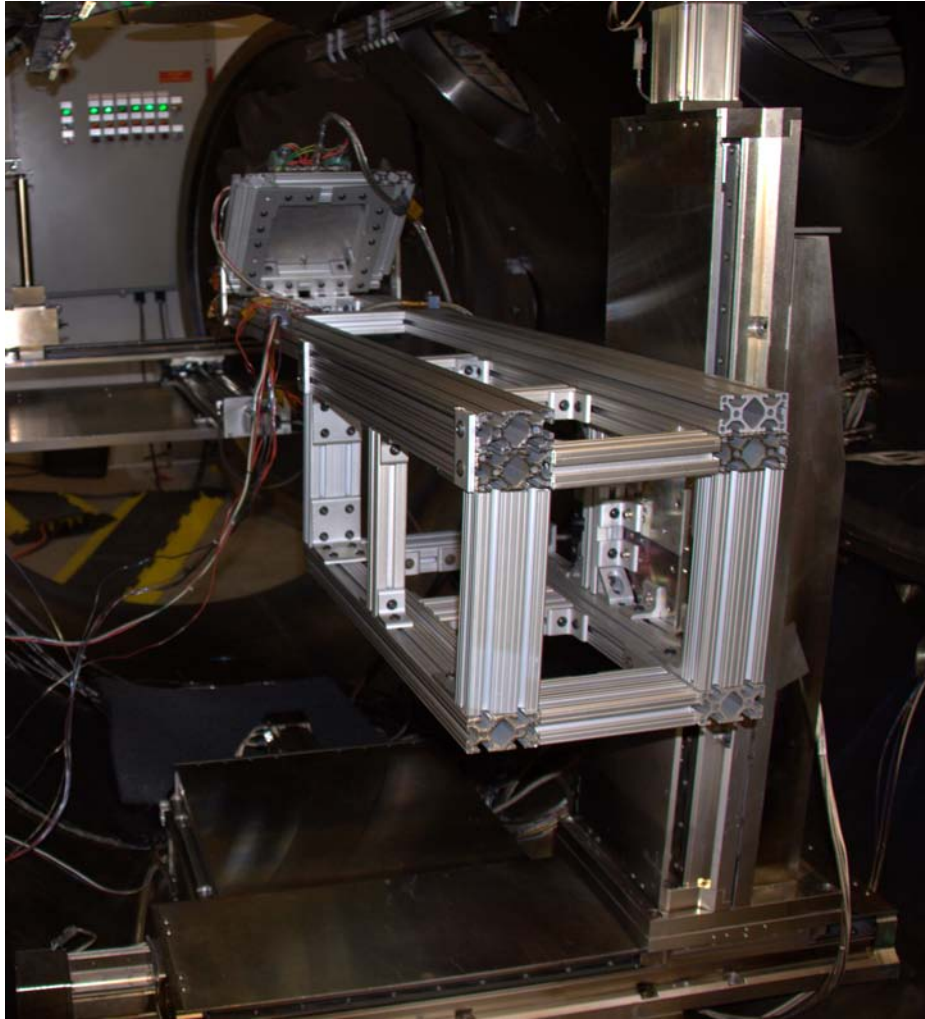


Figure 15: Box frame with cantilever arm mounted to Aerotech z-stage. Three-axis thruster is attached.

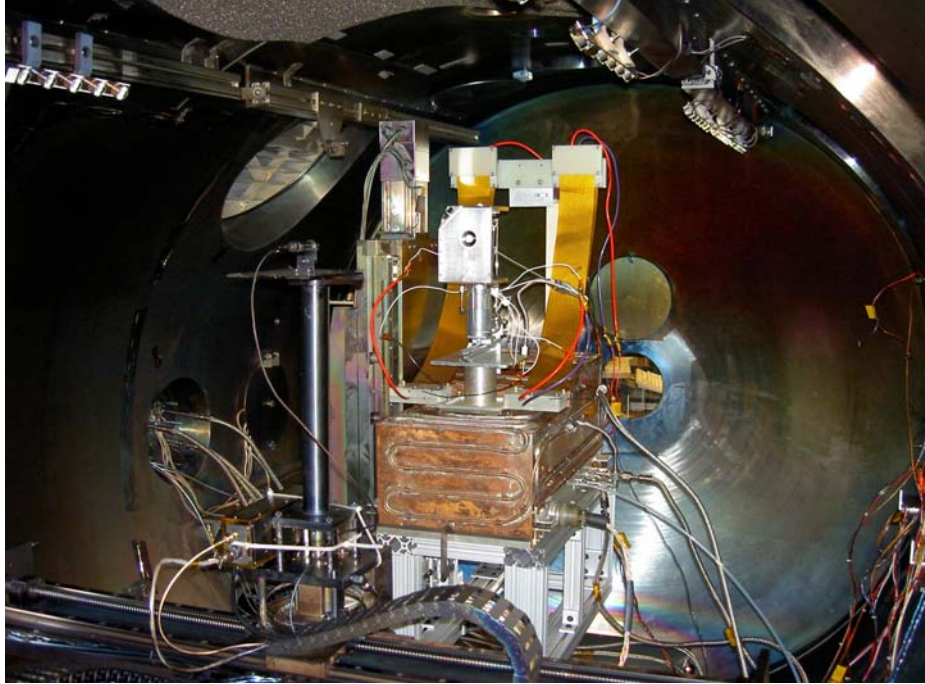


Figure 16: Thrust stand with multi-axis thruster on box frame. Beam profiler radial stage and theta stage with Faraday probe are visible in foreground.

### ***3.3 Thrusters***

Two Hall effect thrusters were used during this research. The first was a Busek BHT-200 low power thruster and the second was the experimental prototype three-axis thruster, manufactured by Busek. The BHT-200 was evaluated to validate experimental techniques and for comparison purposes. It is a well classified thruster with an existing body of research and data. The three-axis thruster is a one-of-a-kind model with no existing information on its performance or nominal operating parameters. It shares most of its components with the BHT-200 thruster which was the primary decision in using BHT-200 nominal operating parameters for testing and BHT-200 performance for baseline comparison.

*3.3.1 BHT-200.* The BHT-200 thruster was operated at manufacturer provided nominal parameters throughout testing. An external BHC-1500 cathode was used in a standard configuration. The cathode was mounted to the thruster using



Figure 17: Beam profiler translation stage is in the foreground. The three-axis thruster is mounted to the Aerotech translation stage at the far end of the chamber.

the manufacturer's provided mounting bracket for most testing. Two separate xenon propellant lines were used, one for the thruster and one for the cathode.



Figure 18: BHT-200 thruster with BHC-1500 cathode on mounting bracket [60].

*3.3.2 Three-axis Thruster.* The three-axis thruster was essentially a cluster of BHT-200 thrusters oriented orthogonally to each other (referred to hereafter as the x-face, y-face and z-face using a right handed axis system). Provisions were provided for operating the anodes through independent circuits, but all three were connected in parallel for this research. The three faces shared a common magnetic circuit with one electromagnet coil servicing the entire assembly.

In operation the three-axis thruster was run at nominal parameters for each face using BHT-200 values. In essence this made the three-axis thruster three separate 200W thrusters with a total power of 600 W for the whole assembly. Nominal magnet current for the BHT-200 is 1 A which was also used for the three-axis common magnet coil during testing. Plasma-wetted surfaces of the three-axis thruster were identical to the baseline BHT-200.

The three-axis thruster incorporated an internal cathode which was mounted equidistant to each of the thruster faces. It was planned to use the internal cathode for

testing of the three-axis thruster. An initial test run demonstrated that the thruster could run successfully on the internal cathode, but unfortunately it soon developed a fault which prevented further operation. Troubleshooting suggested that upon heating the internal cathode developed a short between the keeper and the internal cathode heater preventing proper keeper operation.

Attempts were made to reposition the cathode within the thruster body to prevent the keeper short, but were not successful. At small distances for the keeper-cathode gap the short was still evident. At larger gaps xenon gas was diverted inside the thruster body. Upon trying to light the thruster in these situations a “plasma ball” would form inside the thruster as ionization would occur at the side of the anode internal to the thruster, opposite the discharge channel. This unusual failure mode seemed to be unique to this type of internal cathode design. All further testing on the three-axis thruster was conducting using the same BHC-1500 external cathode used with the BHT-200 thruster.

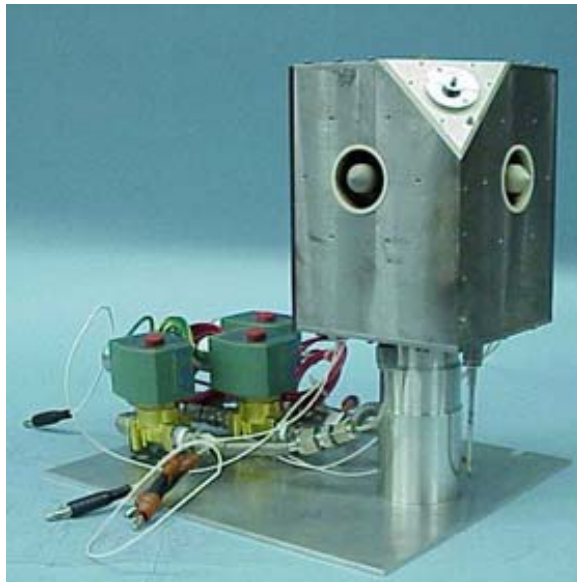


Figure 19: Three-axis thruster [60].

*3.3.3 Propellant System.* Both thrusters were operated from the SPASS lab xenon propellant flow system. Xenon gas was stored in a pressurized tank mounted

external to the vacuum chamber. A regulator valve mounted to the tank reduced pressure from approximately 600 psi to around 20 psi before being routed to two MKS model 180A precision mass flow controllers.

The cathode mass flow controller was rated from 0-10 sccm xenon and the flow controller for the anode was rated from 0-50 sccm xenon. Both controllers are rated to an accuracy of 0.01% of full flow [61]. Xenon flow was routed through a series of valves and stainless steel and PTFE lines via a chamber passthrough to the thruster. Flow rates were controlled and monitored using an MKS Type 247 four-channel readout.

The three-axis controller had a common propellant manifold which received xenon gas from the mass flow controller. Propellant flow to each face of the thruster was then controlled by three independent AC powered solenoid valves. During parallel operation individual faces were turned on and off by controlling xenon flow via the solenoid valves. Total propellant flow to operating faces could be controlled by the mass flow controller, but no provision was made in the three-axis thruster for metering flow to individual faces separately.

*3.3.4 Power Processing Unit.* Both thrusters and the external cathode received power from a Busek BPU-600 Power Processing Unit (PPU). This PPU both provided power to various components and monitored their performance using the BPU-600 Host Simulator, a LabView software interface provided by Busek. The PPU hardware received input power from a Sorensen DCS55-55 power supply rated at 3 kW. Power supply output was adjustable from 0-55 V and 0-55 A.

### ***3.4 Diagnostic Equipment***

Aside from power and propellant flow supplied to the thruster, the primary diagnostic techniques used to evaluate the three-axis thruster were the thrust stand and Faraday probe. The thrust stand was used to measure produced thrust in the 0-20 mN range. This value was then used with the measured propellant flow to determine the specific impulse and thrust efficiency. The Faraday probe provided

beam current density data which was used to determine the total beam current and plume divergence angle.

*3.4.1 Thrust Stand.* A Busek T8 inverted pendulum type thrust stand was used to take total thrust readings for the BHT-200 and the y-face of the three-axis thruster. The thrust stand was controlled and monitored using its rack mounted control box via a bundled cable and cannon plug chamber pass through. At the heart of the stand was a linear variable differential transformer (LVDT) which measured the linear displacement of the stand pedestal. To ensure operation within the linear response region the LVDT was physically adjusted to the zero position by using a set screw on the LVDT core each time the stand configuration was changed. The LVDT was controlled and monitored with a Schaevitz MP2000 LVDT readout controller [62].

The thruster was mounted to the pedestal which was connected to the base by eight metal flexures. Various thickness flexures could be fitted, with thicker flexures used for higher power thrusters. In this case 0.010 inch flexures were used for both thrusters. A spring was attached to both the pedestal and base and was used to damp the motion of the pedestal and center it. Stiffer springs could be fitted for larger thrusters, although no other spring was available during this research.

A passive eddy-current type damper was also installed on the stand. This was energized during movement of the thrust stand and when large motions were expected to reduce the severity of oscillations. It was determined that the damping circuit had little to no effect on the small random oscillations present during test runs and was deenergized during testing.

An inclinometer mounted to the stand base provided inclination information on the stand. The stand level could be adjusted using a stepper motor from the stand control box. The inclinometer digital readout displayed inclination in thousandths of a degree with max deflection at about two degrees. The thrust stand inclination was leveled before each data run and tended to drift slightly during use.

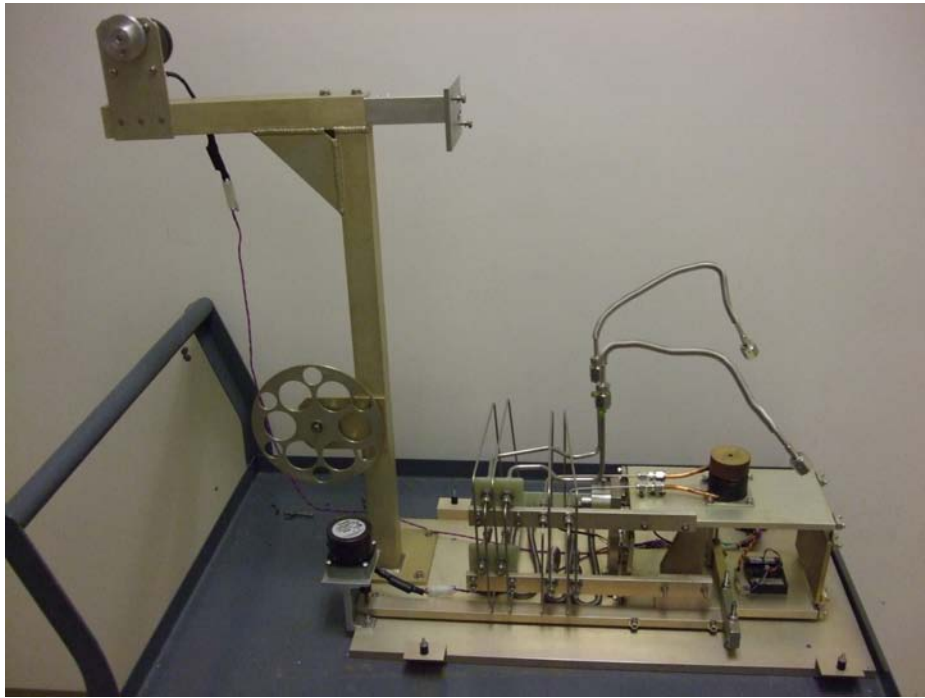


Figure 20: Thrust stand with thermal jacket removed.

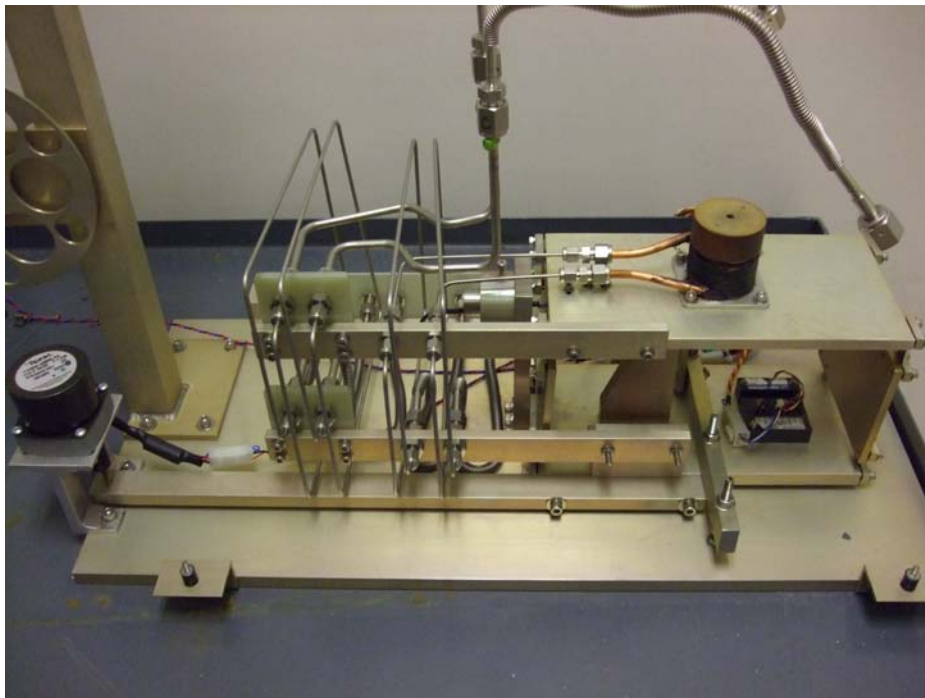


Figure 21: Detail of thrust stand internals.

The stand assembly was surrounded by a thermal jacket which isolated the internal components from the thruster body and plume. This was designed to prevent thermal heating of the stand which would induce thermal drift into the data. The thermal jacket was provided with cooling water from the NESLAB RTE7 water chiller outside the chamber. This chiller provided  $\pm 0.01^{\circ}\text{C}$  temperature stability in the cooling water [63]. The thermal jacket rested on isolation mounts attached to the stand base to minimize the transmission of water pump vibrations to the stand. A cooling line was also routed through the pendulum arm to the base of the thruster mounting pedestal to dissipate heat from the thruster and prevent conductive heating of the stand.

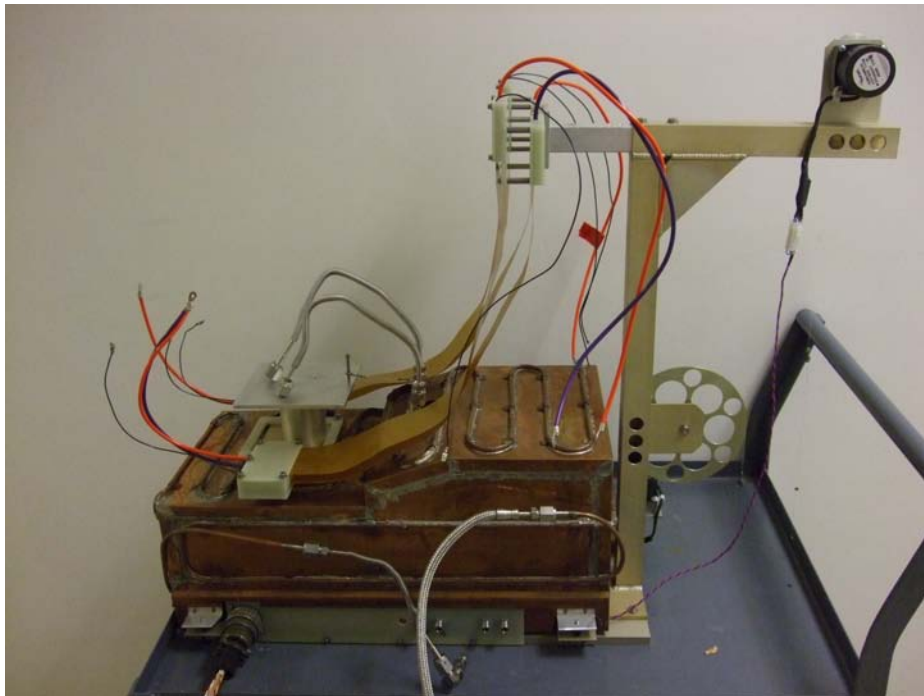


Figure 22: Thrust stand with thermal jacket and wiring harness installed.

The thrust stand was calibrated before and after each run using a series of weights suspended from the stand. Using a line and pulley system the force from the hanging weights was transferred to the stand pedestal resulting in a corresponding linear displacement. Weights were loaded and unloaded using a stepper motor con-

trolled from a switch on the control box. A series of four weights weighing 0.50 grams each was used which provided calibration in the 0-20 mN range.

Amplified output voltage from the LVDT was recorded by a LabView software interface with a 10 Hz recording rate. A near real time display allowed evaluation of the thrust stand performance during testing. During calibration each weight setting was recorded for about four minutes before loading or unloading the next weight. This resulted in 2000-3000 data points per setting.

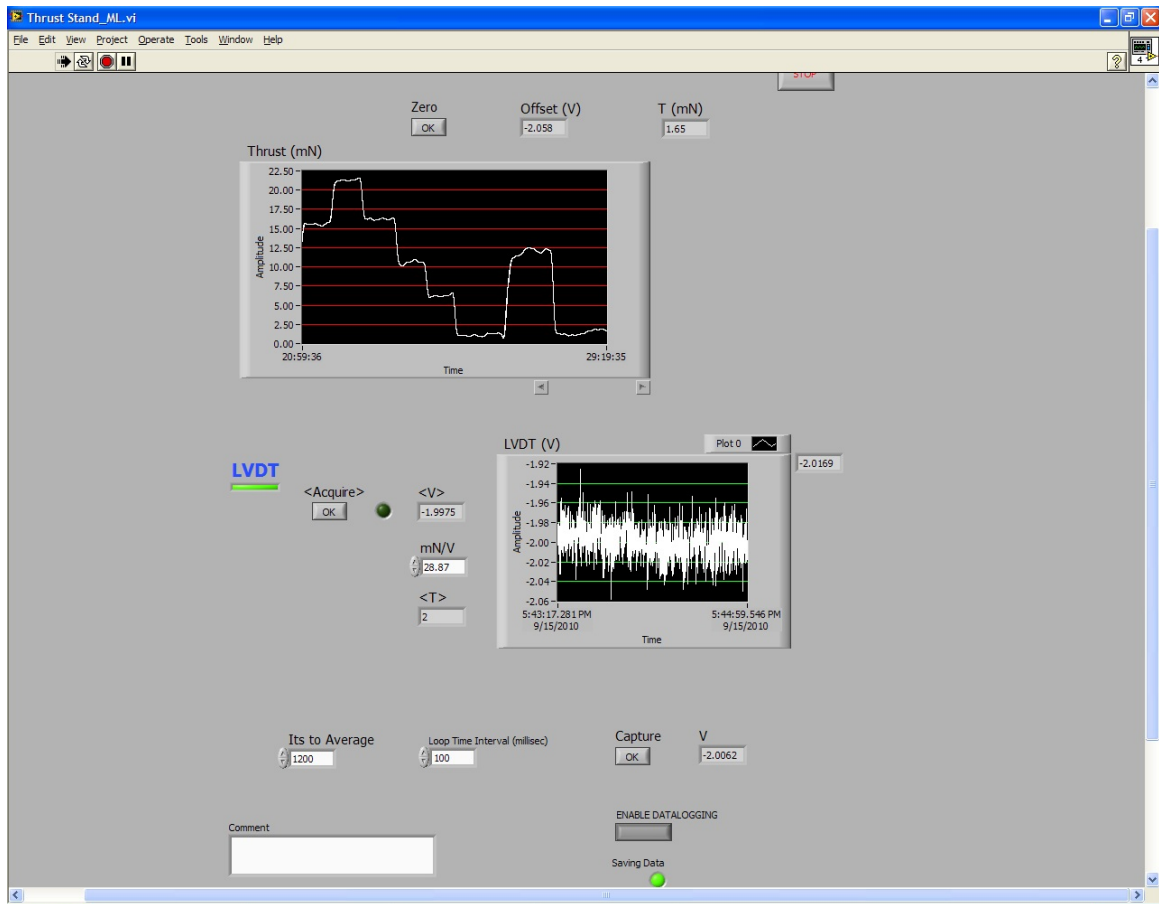


Figure 23: Screenshot of thrust stand VI. Part of a calibration step curve and a BHT-200 measured thrust run are shown in the top graph.

During thrust readings the thruster was operated for about five minutes or until the thruster operation stabilized. Thruster operating time was minimized in an attempt to decrease the amount of thermal drift error in the data. A zero thrust

reading was taken and compared before and after the thruster was operated each time to characterize thermal drift or other data bias.

Initial thrust stand installation had the stand mounted on a box frame attached to the Aerotech translation stage. Early runs displayed a large amount of error due to vibration imparted to the stand by the vacuum pumps. Loose connections internal to the connector plug between the electrical cabling and the control box also imparted an unacceptable amount of random noise. Later runs had the stand mounted to a heavy steel platen which was bolted to the chamber walls to help minimize stand shift due to vibration. This resulted in much more repeatable results.

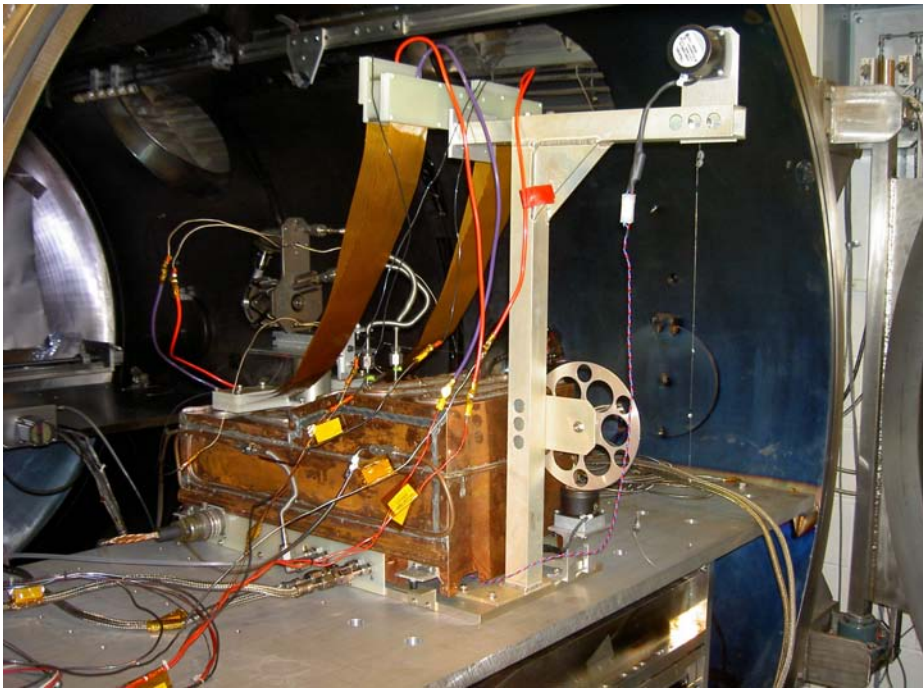


Figure 24: Three-quarter view of thrust stand with BHT-200 attached mounted on steel platen.

*3.4.1.1 Thrust Stand Data Collection and Error Quantification.* Thrust stand calibrations were performed before and after each thrust run to determine the thrust scaling factor in  $\text{mN/V}$ . The voltage generated by the displacement of the LVDT due to produced thrust was then multiplied by this value to determine the thrust in  $\text{mN}$ .

Calibration data was recorded for approximately 4-5 minutes for each calibration weight, including a zero reading at the beginning and end, nine calibration steps. Voltage readings at each step were averaged to find the LVDT voltage for that step. The 50 points (five seconds) before and after each weight addition or removal were not included in the average, only the stable voltage readings at each weight step. Each step voltage was then plotted versus the force in mN produced by the calibration weight at that step. This yielded a linear relationship between thrust in mN and LVDT voltage. The values were then correlated using a least squares linear fit to determine the actual thrust scaling factor.

A calibration bias,  $\Delta b_{cal}$  was determined for each calibration curve. This bias resulted from slightly different measured force values for identical calibration weight loading. In each case the calibration bias was computed using Equation 6, where  $y_i$  is the measured value for a calibration weight setting,  $\bar{y}_i$  was the curve fit value at the calibration weight setting and  $N$  was the number of calibration weight readings over the curve.

$$\Delta b_{cal} = \sqrt{\frac{\sum (y_i - \bar{y}_i)^2}{N}} \quad (6)$$

Comparison of the zero thrust value before and after each run gave an indication of thermal drift and bias error. Observed variation was less than 1%. Bias error due to thermal drift,  $\Delta b_T$  was then obtained by the relationship in Equation 7, where  $V_{zero-}$  was the zero reading before thrust measurement and  $V_{zero+}$  was the zero reading after thrust measurement.

$$\Delta b_T = \frac{V_{zero-} - V_{zero+}}{2} \quad (7)$$

Thrust measurements were initiated by recording zero thrust voltage for approximately 4-5 minutes. This process was repeated after the thruster was shut off also to provide a zero thrust baseline voltage. The thruster was activated and thrust

voltage measurements were recorded for 5-10 minutes. The thrust voltage data was then broken into 20 second blocks (200 data points) which each produced an average thrust voltage. The approximately thirty seconds worth of data after start and shut-down was not included due to the tendency of the thrust stand to oscillate during this time as a result of the sudden motion. The 20 second averages were then averaged together to find the total average thrust voltage over the run. This average thrust voltage multiplied by the calibration scaling factor was the thrust produced.

The statistical error of the thrust measurements was calculated by taking the standard error, shown in Equation 8, where  $\sigma$  was the standard deviation of the 20 second averages and  $n$  was the number of 20 second blocks.

$$SE = t \frac{\sigma}{\sqrt{n}} \quad (8)$$

A value of 1.96 for  $t$  gave a confidence factor of 95%.

A resolution bias for the LVDT controller readout was also calculated. The readout recorded voltage to 0.1 mV. By taking half this value and multiplying by the thrust scaling factor, the resolution bias,  $\Delta b_{res}$  was obtained. The standard error was the greatest contributor to the overall error in all cases, while the resolution bias was tiny. The total error was calculated by the method in Equation 9.

$$error = \sqrt{\Delta b_T^2 + SE^2 + \Delta b_{res}^2 + \Delta b_{cal}^2} \quad (9)$$

Total error of thrust stand measurements was found to be  $\pm 2-5\%$  of measured thrust.

*3.4.2 Faraday Probe.* The Faraday probe consisted of a collector disk with a potential applied to it mounted inside a guard enclosure to which a potential was applied to repel electrons. A small aperture was present in the front of the guard which allowed ions to enter and strike the collector. A ceramic insulator isolated the two. The collector disk voltage was read across a resistor with a known resistance.

Typically, the collector is biased positive to repel any low energy charge exchange ions in the plume while the guard is biased negative to repel electrons. Current density,  $j_B$  was determined from the following equation [64]:

$$j_B = \frac{V \cdot 1000}{R \cdot A_{aperture}}$$

$V$  was the voltage measured across the resistor,  $R$  was the value of the resistance and  $A_{aperture}$  was the area of the guard aperture. The resulting current density was expressed in  $mA/cm^2$ .



Figure 25: Photo of Faraday probe, taken from *Faraday Probe Operating Manual* [64].

The probe aperture diameter was 0.763 mm, giving a value for  $A_{aperture}$  of  $0.00457cm^2$ . The collector disk was biased to +20 V using a Keithley 6517A elec-

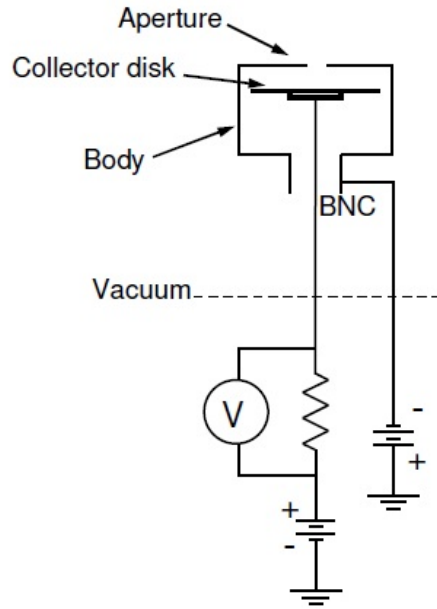


Figure 26: Faraday probe schematic diagram, taken from *Faraday Probe Operating Manual* [64].

trometer/high resistance meter. The guard body was biased to -20 V using an Agilent 6038A power supply. Midway through testing the guard body power supply output became erratic and failed. An identical model 6038A power supply was substituted for further testing. Probe voltage was read by an Agilent 34970A data acquisition switch with an accuracy of  $\pm 0.02\%$ . Voltage readings were recorded by the beam profiler LabView software interface. At each scan point three voltage readings were taken at 0.1 second intervals and averaged to create an individual data point.

Using both translation stages in conjunction allowed two separate scan profiles to be performed. The first profile involved taking probe readings at 10 cm intervals at axial distances from the thruster of 30-100 cm. Axial distance was held constant at each interval with probe readings recorded at one degree arc increments. Due to the physical travel limitations of the beam profiler stage the total arc distance covered was different for each axial distance to a maximum of about 60-70 degrees. The 60-100 cm arcs for these scan coverage areas are shown in Figures 28 and 29.

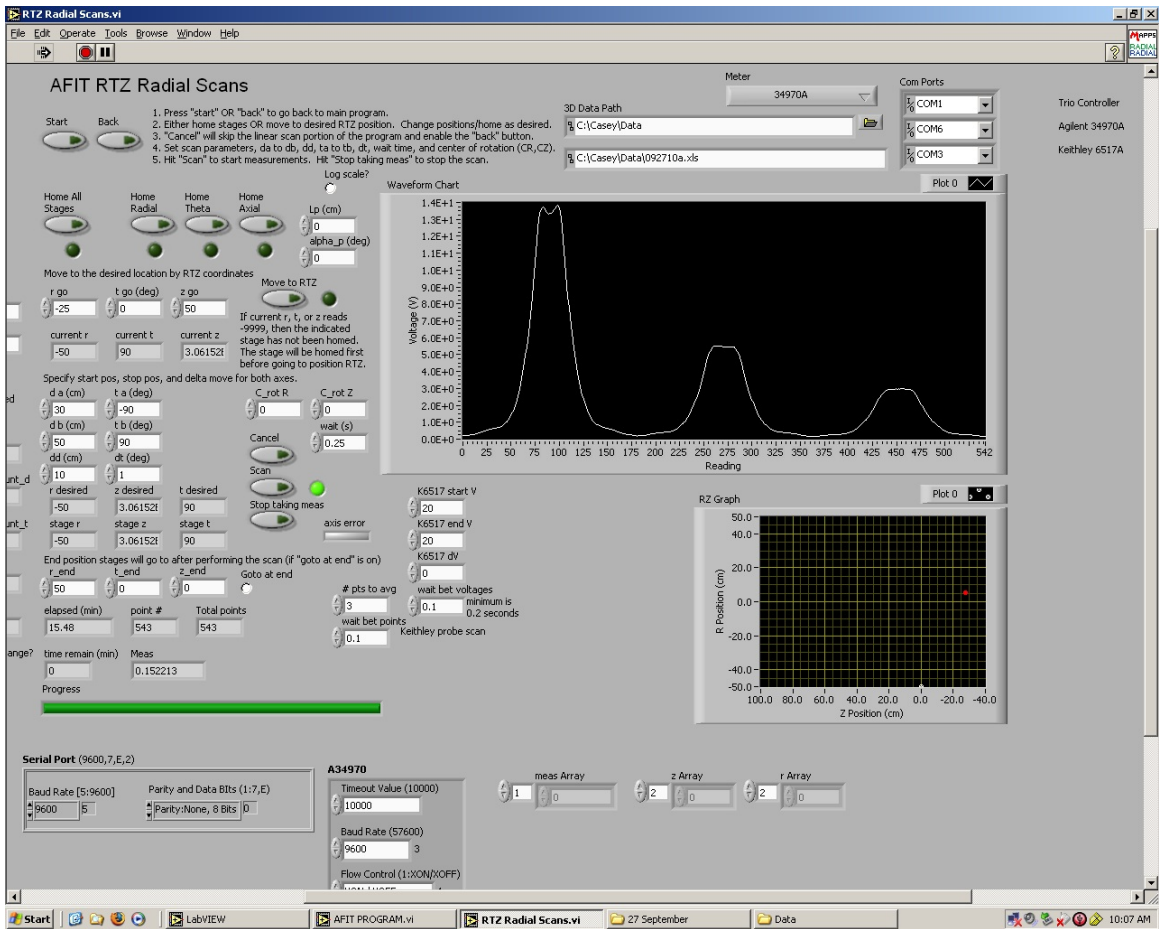


Figure 27: Screenshot of beam profiler radial scan VI displaying results of Faraday probe scan at three different axial distances.

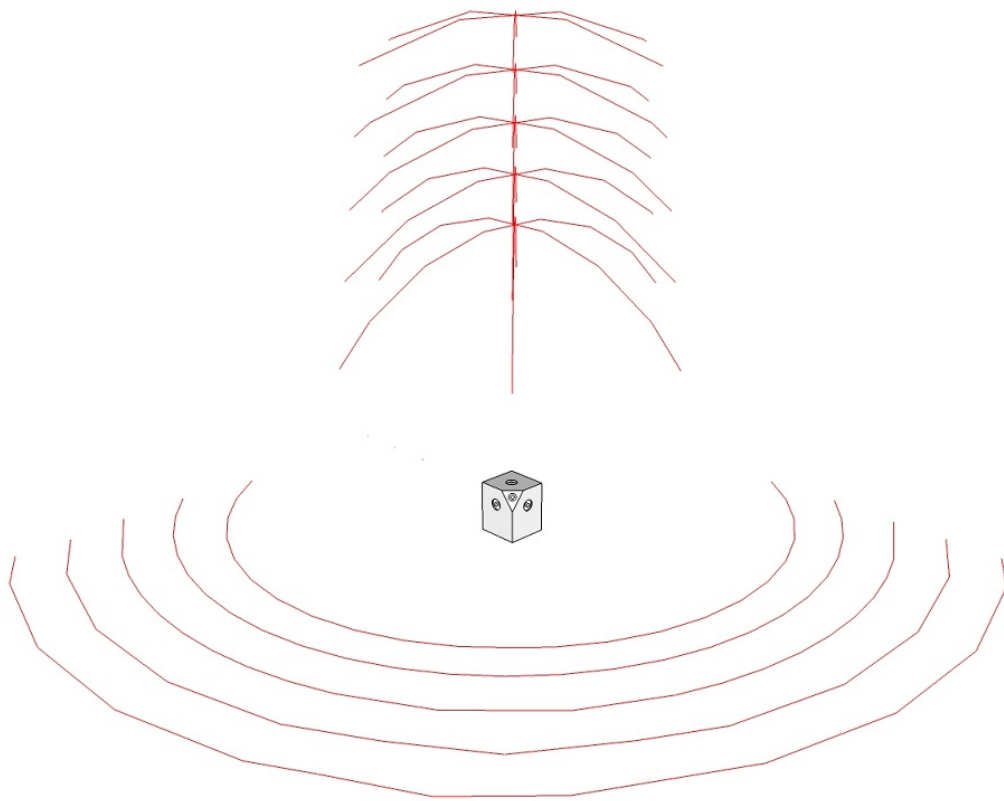


Figure 28: Diagram of Faraday probe coverage arcs.

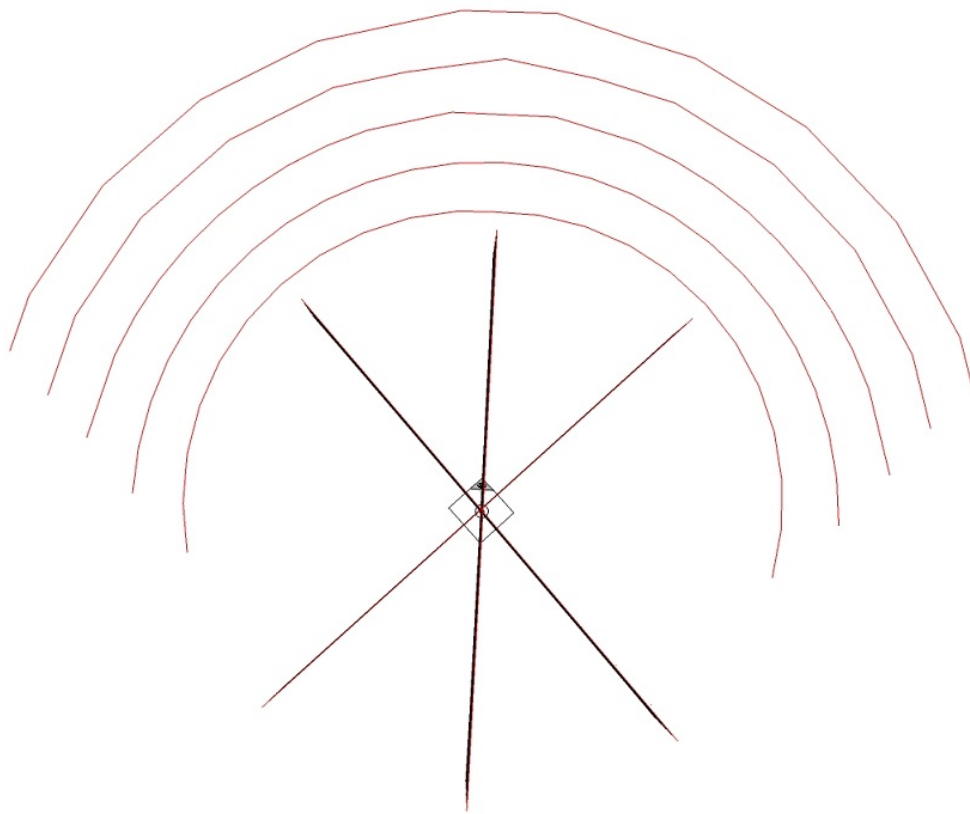


Figure 29: Top view diagram of Faraday probe coverage arcs showing multiple coverage planes through Z-face.

The second profile was performed for the multi-axis thruster and positioned the thruster within the full travel range of the beam profiler stage. This positioning allowed the Faraday probe to cover a full 180 degrees of arc at an axial distance from 30-50 cm. A number of scans were performed with the multi-axis thruster in various positions to achieve full 180 degree coverage of each face. The 30 cm radius coverage arcs are shown in Figure 30.

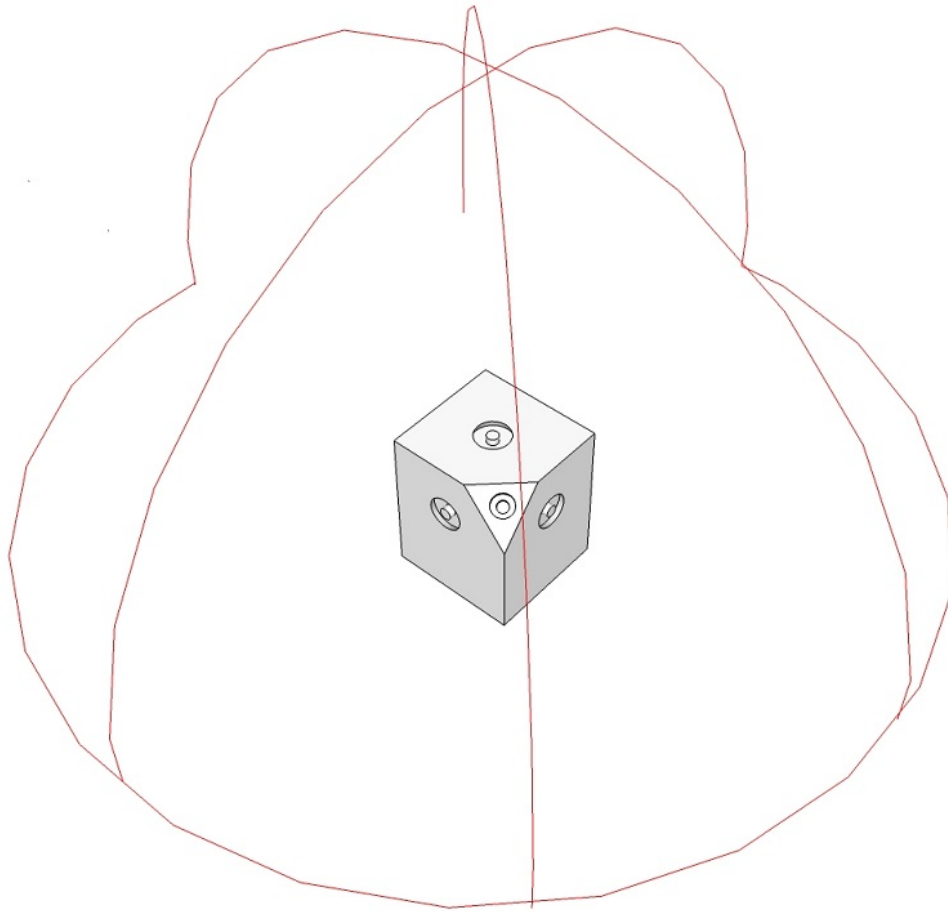


Figure 30: Diagram of 180 degree Faraday probe scan arc at 30cm radius.

Axial distances were measured slightly differently for the two thrusters. Axial distance for the BHT-200 was measured from the front face of the thruster. Axial distance for the multi-axis thruster was measured from the intersection of the thruster face centerlines, i.e., the center of the thruster body. This system resulted in some

masking of the plume by the thruster body at positions near  $\pm 90$  degrees from scan centerline.

*3.4.2.1 Faraday Probe Error Quantification.* By comparing consecutive runs encompassing identical coverage area the variation in measured beam current density was calculated for 3497 individual points. Single plume and unstable ball plume measurements were not included in the overall calculation since these displayed wide variations in measured beam current density. This variation would tend to greatly overestimate the measurement error of the Faraday probe by assuming that variations in the actual measured beam current density were caused by Faraday probe measurement error.

$$error = \frac{\Delta j_B}{j_B} \quad (10)$$

Equation 10 shows the calculation used to determine the measurement error at a point, where  $j_B$  was the measured beam current density and  $\Delta j_B$  was the difference in measured beam current density between consecutive runs. This calculation yielded the error as a percent of the measured value. The numerical average of this value over the entire 3497 point range gave a measurement error of  $\pm 2.19\%$  of beam current density. This was the total measurement error of the Faraday probe.

*3.4.2.2 Faraday Probe Alignment Correction.* In a properly aligned Faraday probe scan the current density distribution should be centered on the thrust axis, which is the zero  $\theta$  angle. For most of the scans a slight alignment error was present which resulted in the distribution being off center.

This alignment error was quantified by determining the full width half maximum (FWHM) value of the curve. The angular width of the distribution curve at FWHM was found and then shifted by a whole degree value to recenter it symmetrically about the zero angle. This correction value was applied to all points in the curve to remove the alignment bias. Not all curves were corrected, but in most cases the shift was

only 1-2 degrees. For no case was it more than four degrees. This offset is well within the angular tolerance of the Faraday probe.

## IV. Results

### 4.1 Overview

This chapter lays out the performance results of the three-axis thruster derived from the measured data. Thrust stand data was used to calculate the produced thrust, specific impulse and propulsive efficiency of the thruster, which was compared to the experimentally determined values for the BHT-200. Faraday probe scans were used to determine the total beam current for the three-axis thruster and characterize the plume shape. Additionally, several discoveries were made about the general operation of the thruster including its tendency to operate in ball plume modes.

### 4.2 Three-axis Thruster Operation

A number of useful observations arose from the simple operation of the three-axis thruster. Since one of the goals of the research was to operate the thruster in multi-face mode a successful test campaign ensued. New operating procedures for the three-axis thruster were developed and tested and the performance modes of the thruster were determined to be different from those of the baseline BHT-200. The most apparent differences were the less efficient propellant utilization of the three-axis thruster and its different plume modes.

*4.2.1 Plume Modes.* A significant discovery during operation of the three-axis thruster is its operation in two distinct plume modes. During multiple face operation all plumes displayed a highly collated jet type plume with a visible central cone. During single face operation the plume was of a diffuse ball type with greater visible divergence and no central cone.

These plume types are not unique to this thruster and have been observed in existing Hall effect thrusters. The jet type plume is typically associated with normal operation of the Hall effect thruster and is the normal plume mode for the BHT-200. The ball type plume is usually only present during operation at grossly off-nominal conditions and indicates a lower efficiency mode. The ball plume is generally regarded

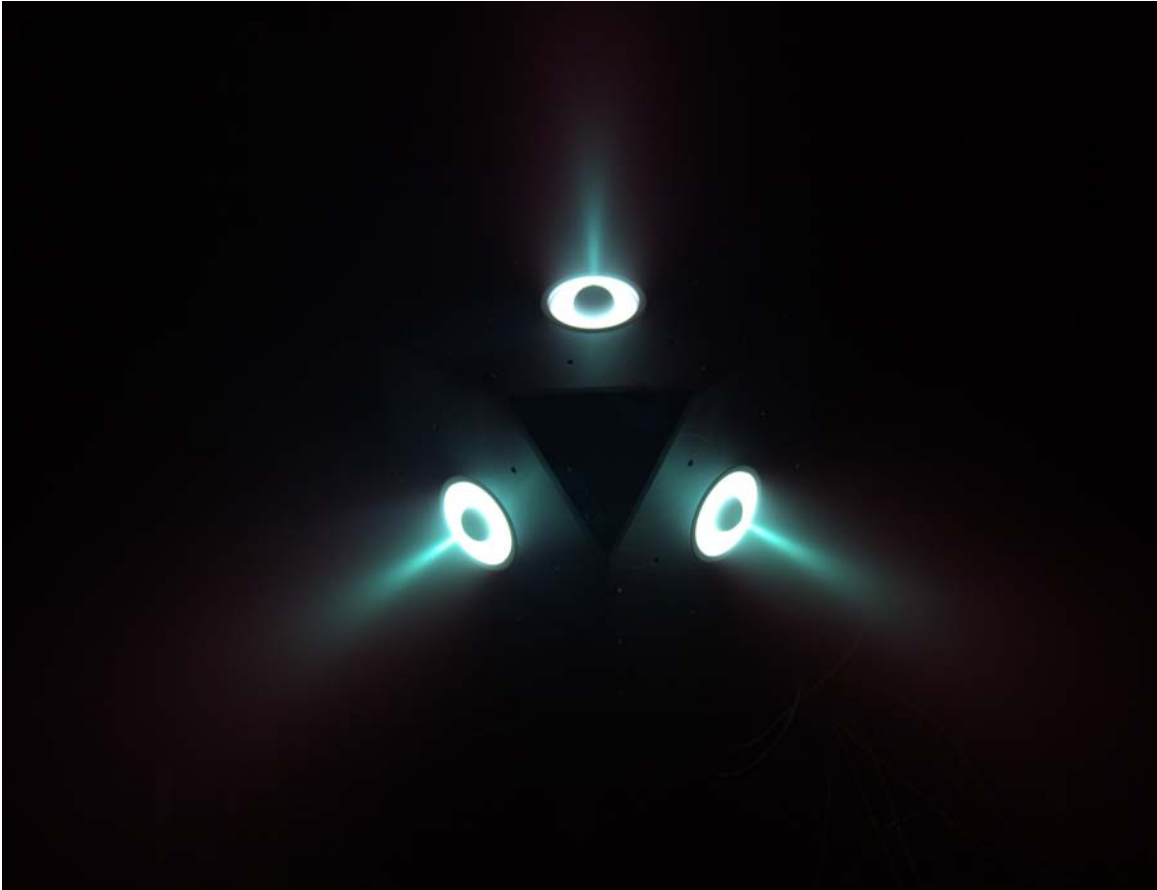


Figure 31: Three-axis thruster in operation displaying all three faces in jet plume mode.

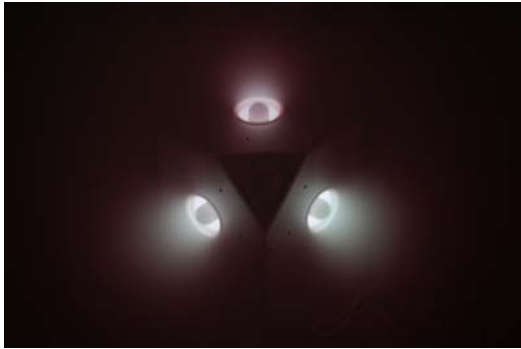


Figure 32: X-face of thruster displaying ball plume mode.

as undesirable because of this loss of efficiency due to the less collimated plume. A normal transition from ball plume to jet plume mode is observed during the startup sequence shown in Figure 33.

The three-axis thruster consistently displayed the ball plume operation in single face mode and jet plumes in multi-face mode. The cause was not believed to be directly related to the number of faces operating but was probably a result of the increased chamber back pressure with multiple faces operating. Indicated chamber pressure tended to increase from  $1 - 2 \times 10^{-5}$  torr for each additional operating face.

Single plumes were observed to transition from ball to jet plume mode when chamber pressure was artificially increased by flowing xenon directly into the chamber from spare propellant lines. This crossover pressure appeared to be around  $2 \times 10^{-5}$  torr. Chamber operating pressure was normally above this pressure during multiple face operation. The premise is if chamber pressure could be maintained



(a) Anode voltage applied at 100 V



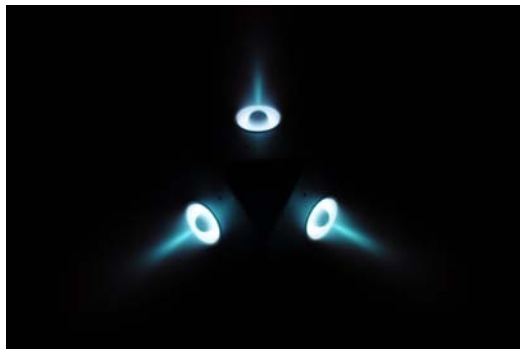
(b) Magnet current energized at 1 A



(c) Anode voltage increased to 150 V



(d) Anode voltage to 200 V



(e) Anode voltage to 250V at nominal settings

Figure 33: Startup sequence displaying transition from ball to jet plumes.

below this crossover point during multiple face operation all faces would continue to display the ball plume mode.

This pressure dependence of the three-axis thruster plume mode is highly relevant to further testing. Chamber pressure must be maintained as low as possible in order to properly simulate the space environment. If the thruster operates in a different mode during ground testing than in space it will be impossible to properly characterize its performance. Alternately, since the ball plume mode is associated with low chamber back pressures, it is likely to be the sole operating mode in space. Future flight ready models of three-axis thruster will require further development to stabilize the plume mode.

*4.2.2 Propellant Utilization.* Although the plume mode of the thruster was immediately obvious during operation, not all important features were so plain. Another difference from the BHT-200 was in the propellant utilization of the three-axis thruster. Ideally they should require the same amount of propellant flow for a given power setting. This was not the case, as became apparent after comparisons of the two.

The three-axis thruster was operated at a nominal 200 W power setting per face for all tests. One of the most useful metrics was the propellant mass flow required. The expectation was that this would be similar to the BHT-200 thruster. Tables 3 and 4 show the observed values for the BHT-200 and three-axis thruster respectively during thrust stand testing. The three-axis thruster values reflect only the y-face was running.

From these results, under similar operating conditions the three-axis thruster single face average mass flow of 0.98 mg/s was close to the BHT-200 average mass flow of 0.92 mg/s. The observed value for the BHT-200 of 0.92 mg/s at 0.78 A discharge current was very close to the reported nominal value from Busek at 0.80 A. In fact, considering the difference in discharge current, they were identical. The data

Anode Current (A)	Chamber Pressure ( $\times 10^{-5}$ torr)	Mass Flow (mg/s Xe)
0.72	2.20	0.875
0.80	2.40	0.875
0.79	2.30	0.865
0.75	2.20	0.890
0.76	2.40	0.934
0.87	2.50	0.934
0.81	2.50	0.895
0.74	2.20	0.885
0.74	2.30	0.930
0.78	2.60	0.998
0.79	2.60	1.008
0.78	2.38	0.917

Table 3: BHT-200 propellant mass flow at 250 V anode discharge potential.

Anode Current (A)	Chamber Pressure ( $\times 10^{-5}$ torr)	Mass Flow (mg/s Xe)
0.78	1.50	0.959
0.79	1.40	0.963
0.79	1.40	0.968
0.77	1.40	0.968
0.78	1.50	0.978
0.79	1.50	0.988
0.80	1.50	0.993
0.80	1.50	0.993
0.79	1.50	0.993
0.79	1.60	0.993
0.79	1.48	0.980

Table 4: Three-axis thruster propellant mass flow at 250 V anode discharge potential, Y-face operating.

suggests these are accurate observed values and the three-axis thruster operates at slightly higher propellant mass flow rates for a given power setting.

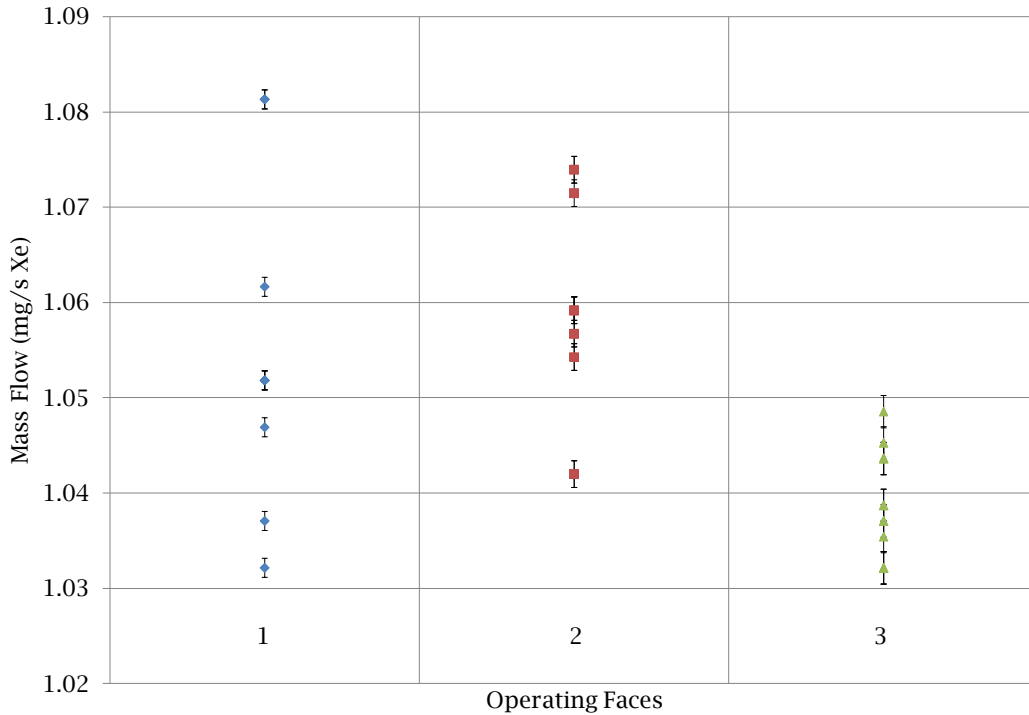


Figure 34: Propellant mass flow per operating thruster face.

Propellant flow rates to individual faces could not be measured with the existing propellant manifold, but an overall mass flow rate normalized by the number of faces operating was determined. The mass-flow-per-face metric plotted in Figure 34 was based on thruster operation during Faraday probe measurements. All values were for 250 V discharge potential and  $0.80 \pm .01$  A discharge current per face at varying back pressures. One conclusion drawn from this plot was the variability of the propellant flow decreased as the number of operating faces increased. Anode discharge current also exhibited the same behavior by showing a larger fluctuation with one face operating versus three or two. Typical observed fluctuations in discharge current were  $\pm 15$  mA with two or three faces operating and  $\pm 30$  mA with one face operating. The unstable ball plume mode observed during single face operation displayed transient fluctuations up to  $\pm 100$  mA at times.

These results suggest a reduced propellant utilization efficiency over the baseline BHT-200 thruster especially in single face operation. Since the three-axis thruster required more propellant flow to provide a given power setting its operation was less efficient than the BHT-200 overall. The increased variability of the propellant flow with fewer faces operating was a further indication of less efficient operation in single and double plume modes. The propellant utilization correlates with the less stable nature of the three-axis thruster plumes and may even be an effect of the propellant manifold system.

### 4.3 Thrust

With previous results showing inferior performance to the BHT-200 it was not surprising to find that thrust data followed suit. Results indicated that the three-axis thruster produced about 40% less thrust than the BHT-200. The BHT-200 measured thrust ranged from 10.64 to 11.28 mN, which is similar to the nominal value cited by Busek. The three-axis thruster operated in ball plume mode on the y-face during all thrust measurements.

Using the known input parameters for power and mass flow to the thruster the global metrics of thrust efficiency and specific impulse were computed directly from the measured thrust. The calculation of efficiency,  $\eta$  shown in Equation 11, where  $T$  the thrust in N,  $\dot{m}$  the propellant mass flow in kg/s and  $P$  the thruster operating power.

$$\eta = \frac{T^2}{2\dot{m}P} \quad (11)$$

Specific impulse,  $I_{sp}$  computed using Equation 12, where  $g_o$  the acceleration due to gravity at earth's surface, with a value of  $9.81 \text{ m/s}^2$ .

$$I_{sp} = \frac{T}{\dot{m}g_o} \quad (12)$$

Thrust measurement results for the BHT-200 thruster over three separate runs are shown in Table 5. The average values from these results were a thrust level of 10.93 mN  $\pm$ 2.52%, 33.0% for  $\eta$  and 1206 s for  $I_{sp}$ . These values were lower than, but reasonably close to the nominal reported values from Busek, which provided a good validation of the procedure.

Pressure (torr $\times$ 10 <sup>-5</sup> )	Anode Current (A)	Power (W)	Mass Flow (mg/s)	Thrust (mN)	Error (%)	$\eta$ (%)	$I_{sp}$ (s)
2.3	0.78	195.0	0.895	10.64	2.57	32.4	1212
2.4	0.80	200.0	0.924	11.28	2.40	34.5	1245
2.5	0.77	192.5	0.954	10.86	2.60	32.1	1161

Table 5: BHT-200 measured thrust and derived values at 250 V anode discharge voltage.

Results for three separate runs of the three-axis thruster are shown in Table 6. Average values from these results were a thrust level of 6.69 mN  $\pm$ 3.55%,  $\eta$  of 11.7% and  $I_{sp}$  of 695 s. These values were substantially lower than those for the BHT-200, even considering experimental error. Another result was the three-axis thruster performance was considerably more variable than the BHT-200. Additional measurements would be required to characterize the thruster better, but it is likely this effect is due to the observed variability of the three-axis thruster plume in single face mode.

The ball plume mode of the three-axis thruster was expected to be less efficient than the jet plume of the BHT-200. The ability to test the three-axis thruster in jet plume mode would provide more evidence. On the occasions when the three-axis thruster was observed to operate in jet plume mode an increase in thrust of approximately 2 mN was seen; a marked improvement, but still quite a bit lower than the BHT-200.

Thrust, thrust efficiency and specific impulse are important global metrics for characterizing the performance of Hall effect thrusters. The direct measurement of thrust from the three-axis thruster allows it to be compared directly with existing thrusters from an overall performance standpoint. Use of thrust and thrust derived

Pressure (torr $\times 10^{-5}$ )	Anode Current (A)	Power (W)	Mass Flow (mg/s)	Thrust (mN)	Error (%)	$\eta$ (%)	$I_{sp}$ (s)
1.4	0.79	197.5	0.963	5.62	3.73	8.3	594
1.5	0.79	197.5	0.983	6.76	1.85	11.8	701
1.5	0.79	197.5	0.993	7.71	4.90	15.1	791

Table 6: Three-axis thruster measured thrust and derived values at 250 V anode discharge voltage with y-face operating.

values as an absolute metric of thruster performance only emphasizes the importance of accurate measurements. A number of factors affecting the operation of the T8 model thrust stand were discovered during testing. The most experimentally quantifiable influence on thrust stand readings was the influence of stand inclination on measured LVDT voltage.

*4.3.1 Thrust Stand Inclination Dependence.* Thrust stand LVDT voltage turned out to be directly dependent on the measured inclination of the stand, imparting an additional drift bias. Performing calibration runs to measure the LVDT voltage while manually changing the inclination using the leveling motor resulted in the data shown in Figures 35 and 36. These figures clearly show a linear relationship between the LVDT voltage and the measured inclination, more dramatically in Figure 35. The greater scattering apparent in Figure 36 is most likely due to the greater deflection of the stand centering spring as a result of the heavier thruster.

Using this data a correction factor for stand inclination drift is possible. Since the inclination was reported only on the control box readout and not recorded with the data file, a direct correction to the thrust data is not available. The ability to correct the thrust measurements and calibration curves for the inclination drift can be used to improve future measurements. Drift of up to 0.01 degree was observed during thrust calibrations.

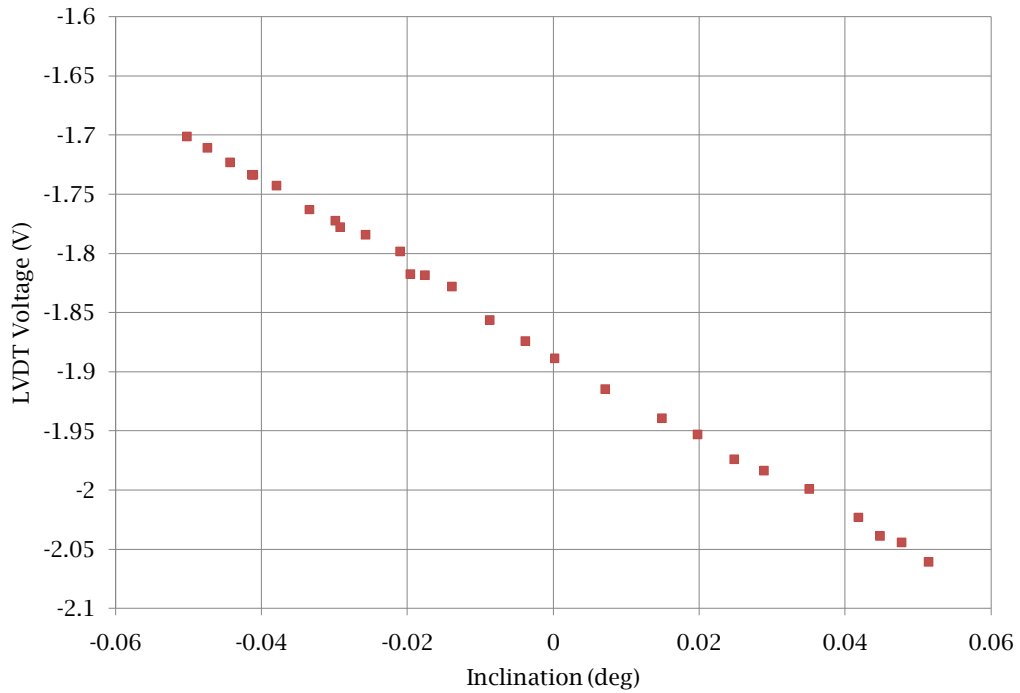
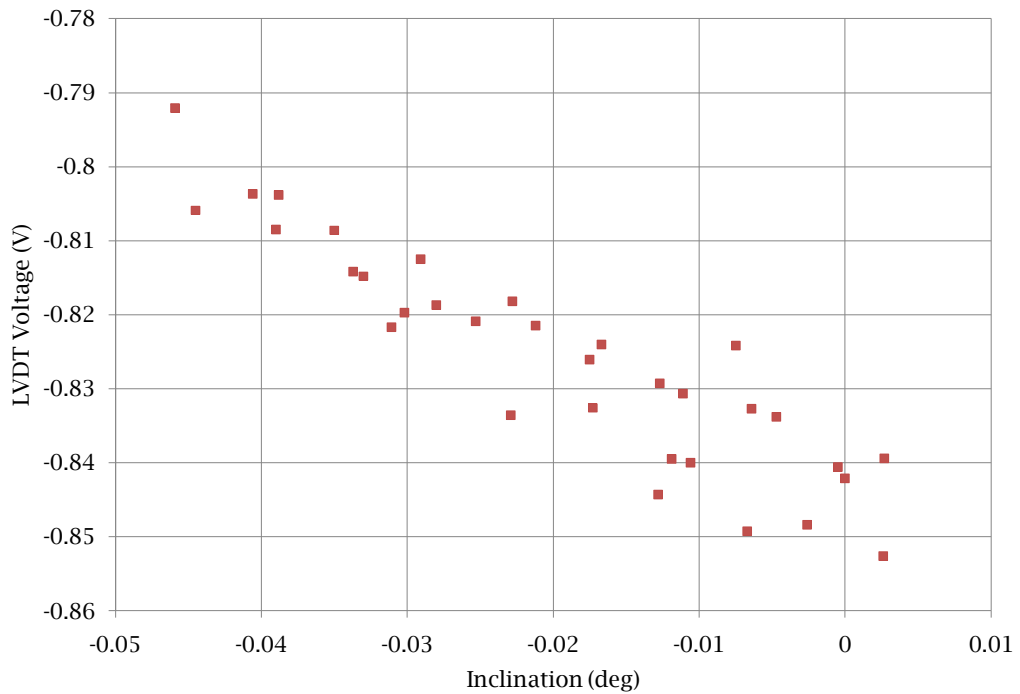


Figure 35: Thrust stand LVDT voltage as a function of inclination, BHT-200 thruster mounted.



#### 4.4 *Faraday Probe Results*

While thrust and the thrust derived values calculated above provide an absolute means of comparison common to all types of electric thrusters, some of the most relevant values for Hall effect thrusters in particular are the beam current and the plume divergence angle. Beam current can be compared to anode discharge current as a measure of how efficient the thruster is at transferring current to the plume and divergence angle gives an indication of plume shape and how tightly collimated it is. Both are important for spacecraft integration.

The means to determine both beam current and divergence angle is through Faraday probe measurements. Even though Faraday probe techniques are well established for use with Hall effect thrusters the three-axis thruster presented a unique subject for investigation. Often the operating parameters of the thruster are varied to provide different data from the Faraday probe scans. In this case only the number of plumes operating and the orientation of the thruster were changed. For all Faraday probe results shown the thrusters were operated at 250 V discharge voltage and propellant flow sufficient to create 0.8 A discharge current per operating face. The goal was to provide the maximum amount of coverage area for each face in each plume configuration.

*4.4.1 BHT-200.* A number of Faraday probe scans were performed on the BHT-200 thruster for comparison purposes. Results are shown in Figures 37 and 38. These show a highly symmetrical current density distribution which drops off exponentially away from the centerline. It also shows an exponential drop in the peak current density as distance increases. This decrease is expected since the total beam current is distributed over a hemisphere with a radius equal to the scan distance. The characteristic double peak centered on the thrust axis is present. This shape is due to the cylindrical discharge channel of the Hall thruster. The double peak is a good indicator of the thruster centerline position and serves also to show that the thruster is operating in jet plume rather than ball plume mode.

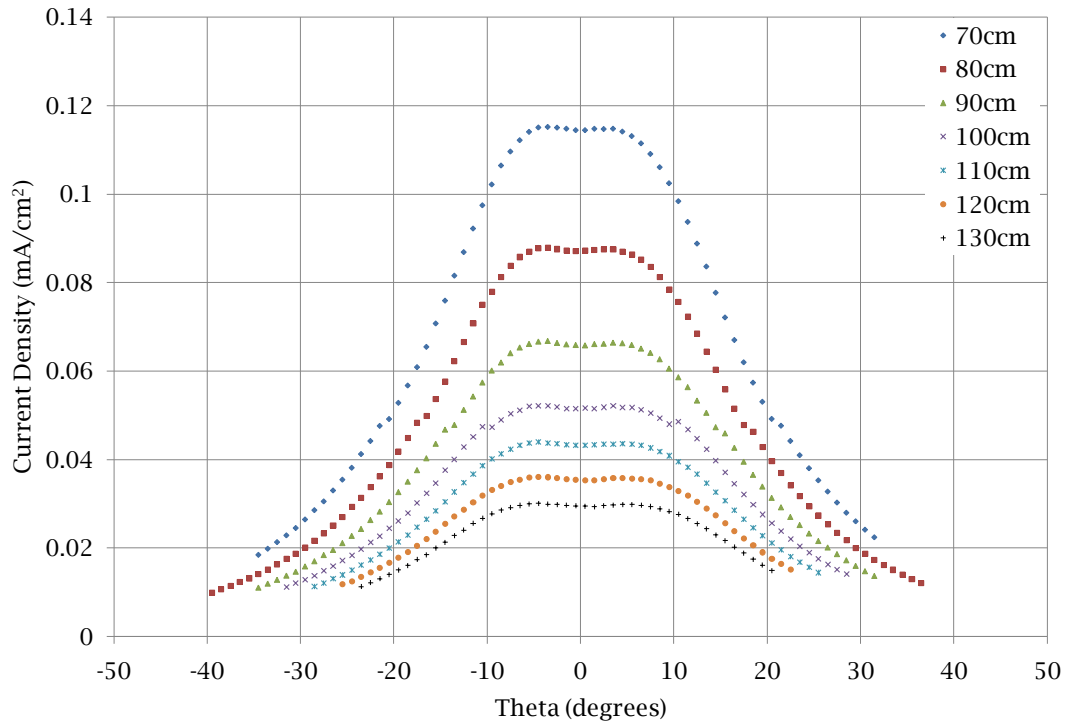


Figure 37: Current density for BHT-200 thruster.

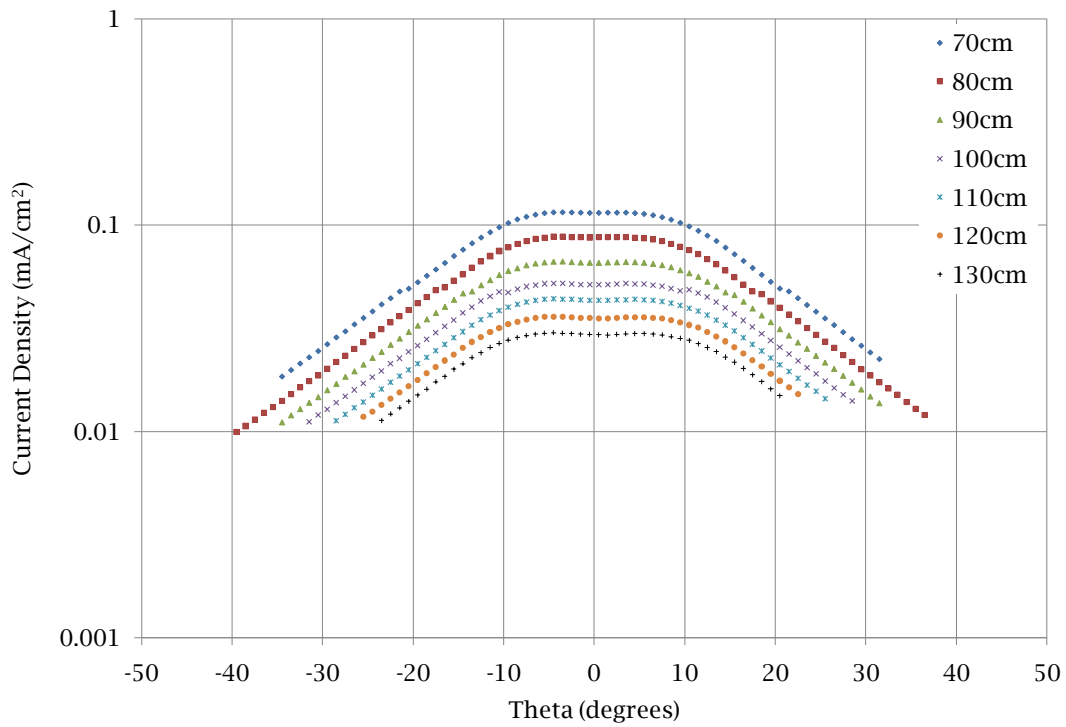


Figure 38: Current density for BHT-200 on logarithmic scale.

Total beam current for the 70 cm scan radius was calculated for the  $\pm 33$  degree of centerline coverage arc. Since a full 180 degree scan was not conducted on the BHT-200 this was then compared to the results for the three-axis thruster at the same radius and coverage region. Three-axis thruster results showed that this central third of the arc yielded 40% of the total beam current. When scaled by this factor the BHT-200 total beam current was 0.54 A. Typical Hall thruster performance suggests that one third of the discharge current was an electron current produced by the cathode which flowed to the anode. This current was not present in the beam so beam current values should have been about 67% of the anode discharge current [65]. Compared to the operating discharge current of 0.8 A during the measurements this gave a beam current utilization of 68% for the BHT-200. This result serves as a positive validation of the Faraday probe measurements and beam current calculations.

*4.4.2 Single Plume Mode.* Figures 39 and 40 show the same scan for the three-axis thruster x-face in single plume mode. This scan also showed an exponential drop off in peak current density, but the distribution was much flatter and peak current density was lower than that for the BHT-200. The double peak structure was not present and the values near centerline were more variable. These differences were primarily due to the three-axis thruster operating in ball plume mode when only a single face was active. Ball plume scans of the BHT-200 were not conducted, but could be expected to show similar characteristics.

180 degree scans of the x-face in single plume mode are shown in Figure 41. This scan matches well with the longer range scans and shows the large increase in peak current density and the more peaked nature of the distribution at smaller radii. The double peak was present in the 30cm scan. The asymmetric nature of the double peak may indicate a small angular pointing error in the Faraday probe during measurement, or may be an unknown effect of the three-axis thruster. It was present in most of the scans.

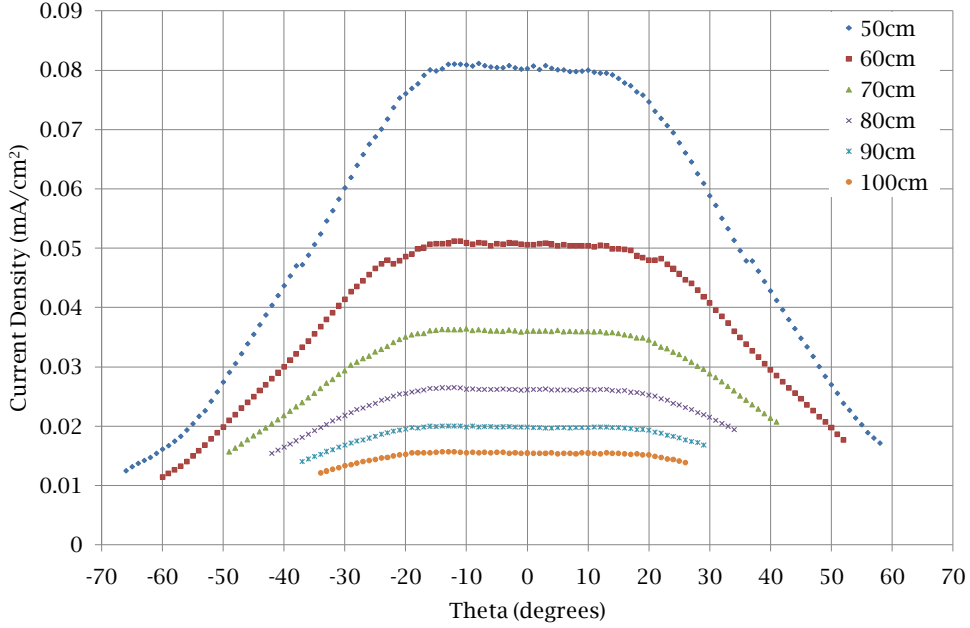


Figure 39: Current density for three-axis thruster, x-face.

From the data in Figure 41 values for total beam current,  $J_B$ , divergence angle,  $\Theta$ , and beam current utilization,  $\eta_J$ , were calculated.  $\eta_J$  is the percent of the anode discharge current present as measured total beam current. These results are in Table 7. The decrease in beam current at greater distances was due to losses in the plume such as collisions with ambient neutrals. The apparent increase in divergence angle and decrease in beam current utilization were a result of the change in beam current. Therefore, the closer values should have been more accurate.

Radius (cm)	$J_B$ (A)	$\Theta$ (deg)	$\eta_J$ (%)
30	0.419	66	52.4
40	0.418	71	52.3
50	0.415	74	51.9

Table 7: X-face beam parameters.

Identical scans were performed for the y and z faces of the thruster. Faraday probe data for the y-face is shown in Figure 42. This plot shows a lower peak current density and greater flattening of the distribution for the y-face than the x-face. During operation the plume of the y-face was less stable and more likely to operate in the

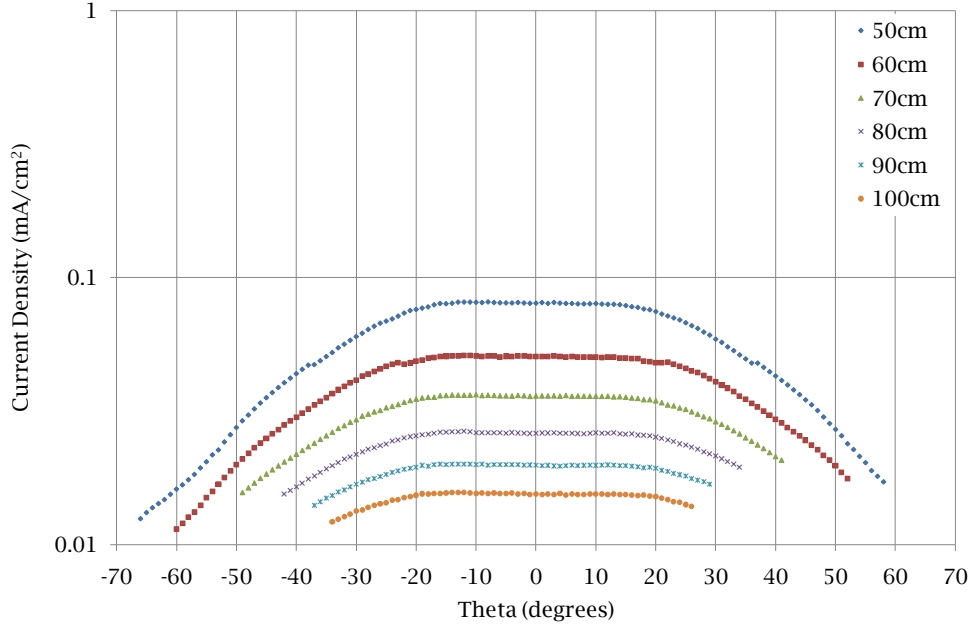


Figure 40: Current density for three-axis thruster, x-face, on logarithmic scale.

ball plume mode. The less tightly collimated plume resulted in the current density distribution shown in Figure 42.

Plume parameters for the y-face were calculated from the Faraday probe data and are shown in Table 8. The values for  $J_B$ , and therefore,  $\eta_J$  were only slightly lower than those for the x-face, but the divergence angle values were higher. This result means the y-face plume was noticeably more divergent, but contained the same amount of total beam current.

Radius (cm)	$J_B$ (A)	$\Theta$ (deg)	$\eta_J$ (%)
30	0.412	71	51.4
40	0.408	74	51.0
50	0.406	75	50.8

Table 8: Y-face beam parameters.

Z-face data is shown in Figure 43. This plot shows a similar distribution to the y-face, without the central double peak and a large amount of spreading. In single face operation the z-face plume was observed to operate exclusively in ball plume mode, but appeared visibly more stable than the y-face plume. Plume parameters for

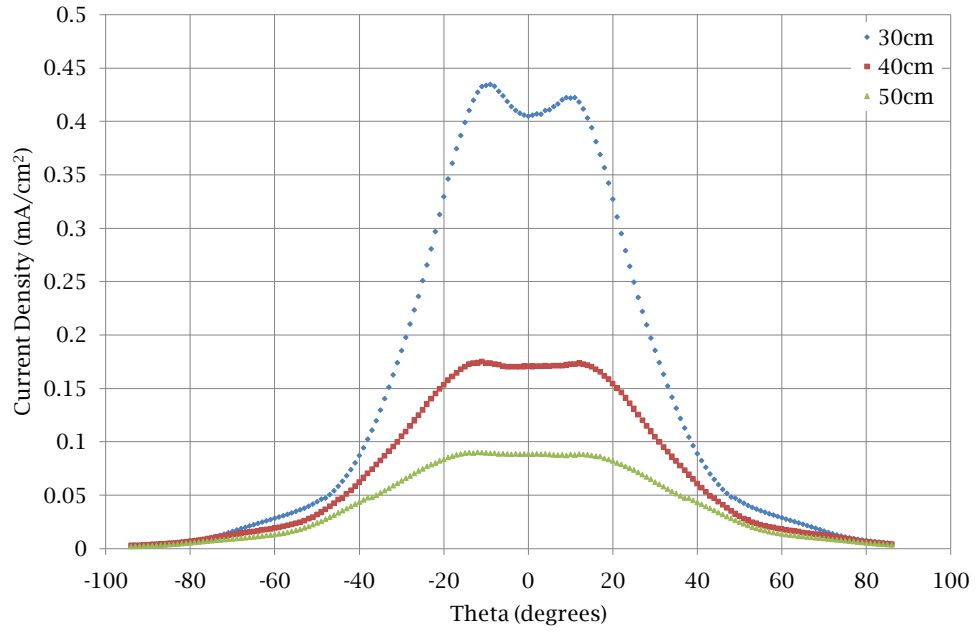


Figure 41: Current density for x-face, single plume.

the z-face are shown in Table 9. This table shows a lower beam current and higher divergence for the z-face plume.

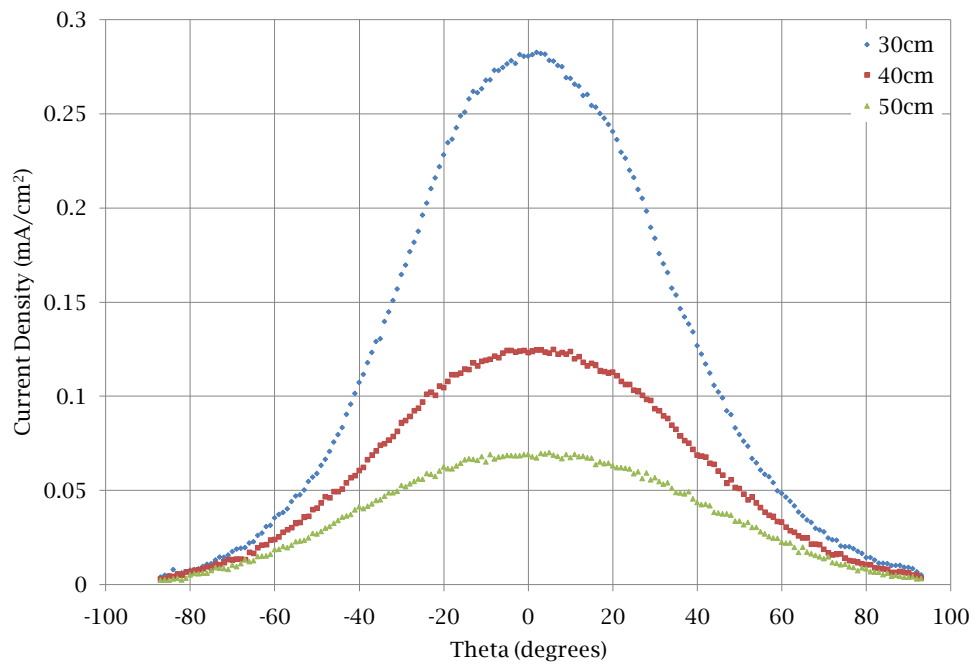


Figure 42: Current density for y-face, single plume.

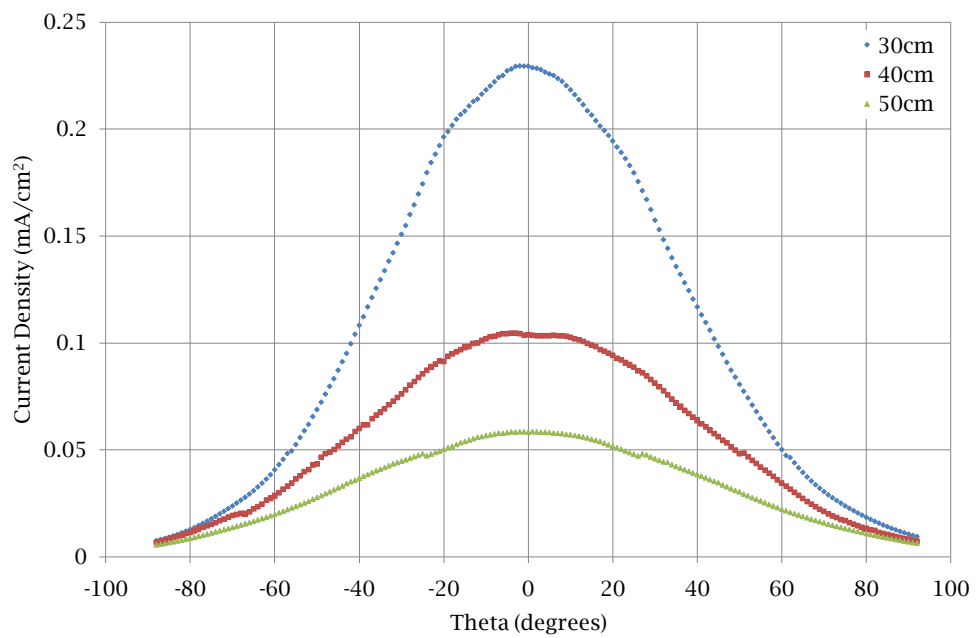


Figure 43: Current density for z-face, single plume.

Radius (cm)	$J_B$ (A)	$\Theta$ (deg)	$\eta_J$ (%)
30	0.396	75	49.5
40	0.401	78	50.1
50	0.391	80	48.9

Table 9: Z-face beam parameters.

4.4.3 *Double Plume Mode.* Operation of the x and y-faces with the z-face operating out of plane allowed for a 180 degree scan of the plume while theoretically excluding the z-face plume. Since the thruster faces switched to jet plume mode when multiple faces were operating the results were not directly comparable to the above single face data. It does provide some indication of how the thruster faces might look if operating in jet plume with a single face active.

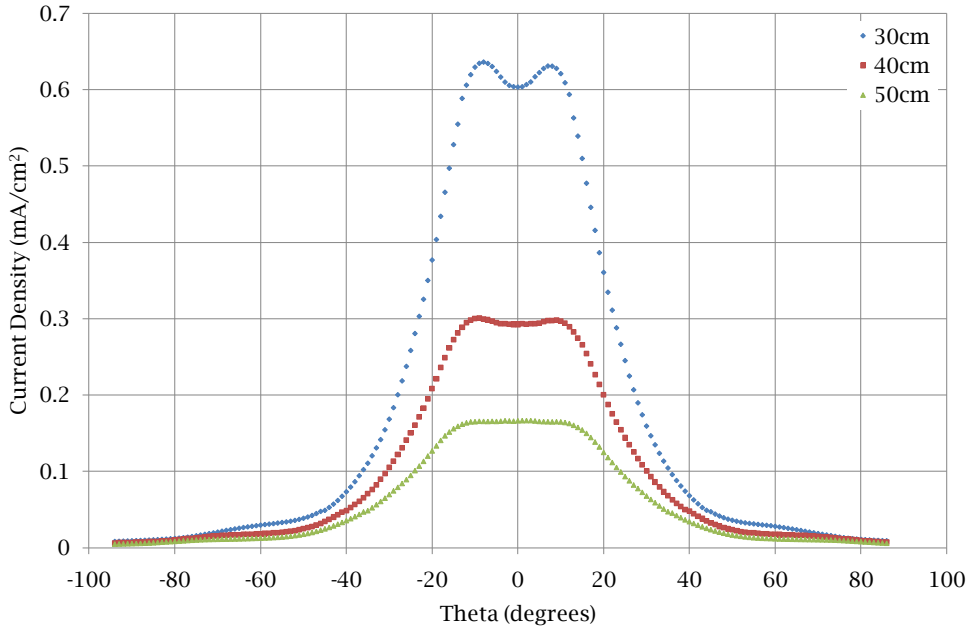


Figure 44: Current density for x-face, x and z-faces operating.

Figure 44 shows the x-face in double plume mode with the x and z-faces lit. The x-face was operating in the jet plume mode and the double peak structure was clearly visible. Peak current density was higher than in single plume mode and the distribution was slightly more peaked. Plume parameters in Table 10 show that the

total beam current actually increased as the scan radius became larger. This increase was almost certainly due to the interaction with the z-face plume. Some of the measured current was coming from the z-face as plume ions being drawn into the x-face plume or charge exchange ions created by the z-face plume being accelerated perpendicular to the z-face. The fact that the measured current increased with distance may support the latter.

Radius (cm)	$J_B$ (A)	$\Theta$ (deg)	$\eta_J$ (%)
30	0.452	70	56.5
40	0.475	74	59.3
50	0.485	77	60.6

Table 10: X-face beam parameters, double plume.

The greater divergence angles for the double plume mode over the single plume mode may be a result of this artificially high beam current. One might reasonably expect the divergence angle to be lower in the jet plume mode which has a visibly less divergent plume. Calculating the divergence angle for the double plume x-face current density distribution using the total current values for the single face mode gives an angle of around 55 degrees for all distances. Similar results were seen in the y-face and are plotted in Figure 45. Beam parameters are shown in Table 11 and show the identical trend. Divergence angle for the double plume current distribution calculated using total current from the single plume is 56 degrees.

Radius (cm)	$J_B$ (A)	$\Theta$ (deg)	$\eta_J$ (%)
30	0.452	71	56.5
40	0.467	76	58.4
50	0.481	79	60.1

Table 11: Y-face beam parameters, double plume.

Double plume scans were conducted for the z-face in the plane containing the x-face, the plane containing the y-face and 45 degrees between the two. Results are shown in Figures 46 through 48. The readings for the 45 degree plane with the y and z-faces operating is identical to those for the x and z-face plot but with slightly lower values observed at theta angles near -90. These plots demonstrate that the peak

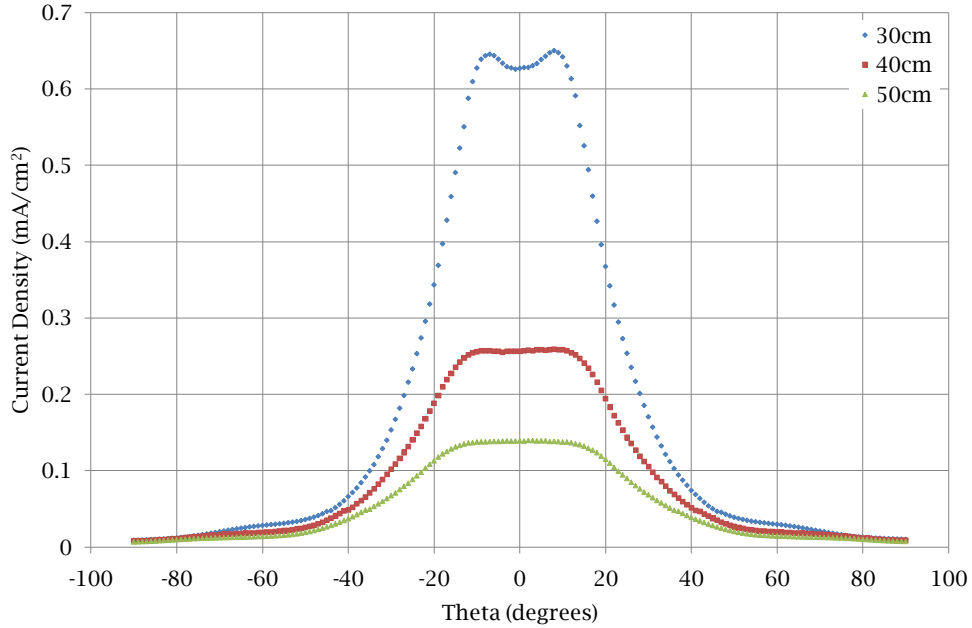


Figure 45: Current density for y-face, y and z-faces operating.

current densities for the three faces are consistently highest for the x-face, slightly lower for the y-face and considerably lower for the z-face. Peak current density for the z-face is higher when operating with the x-face than the y-face.

Also notable in these plots is the region 45 degrees between the thruster faces. Here the current density drops to some value lower than the surrounding regions, but higher than the region 45 degrees opposite the thruster centerline away from the second face. This effect is more clear in Figure 49, where the current density exponentially decays to the midpoint at -45 degrees. This current density is at substantially higher values than the opposite side and above the “step” region where charge exchange ions begin to dominate, suggesting the effect is not due to these charge exchange ions.

The same effect was observed in the region between the x and y-faces. This effect is shown in Figure 50. This plot is Faraday probe data from two 180 degree scans combined into one 270 degree coverage area. The zero degree point was centered

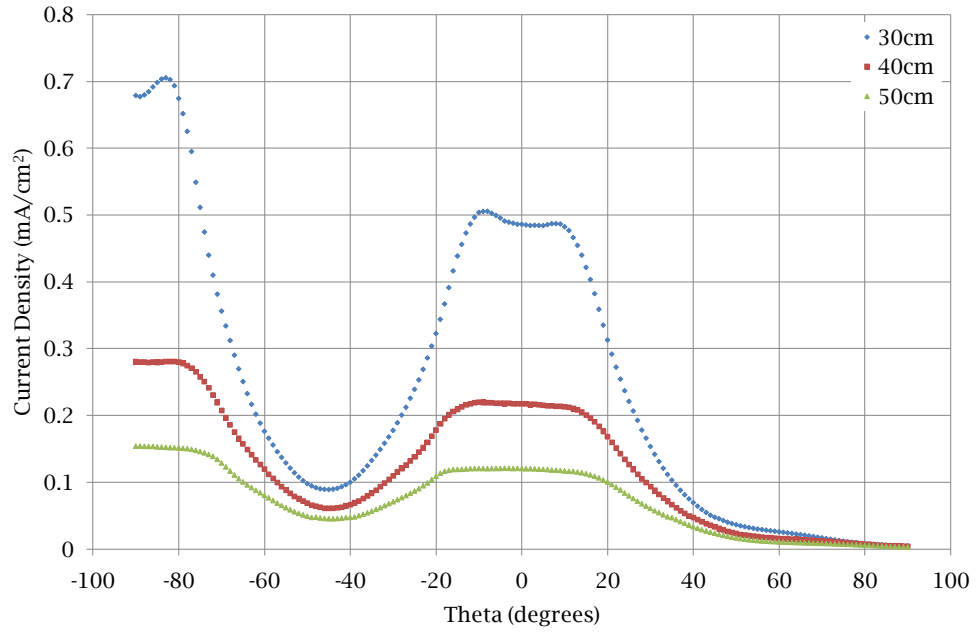


Figure 46: Current density for z-face, x and z-faces operating, in plane.

on the x-face and the greater divergence and lower peak current density of the y-face was very apparent here.

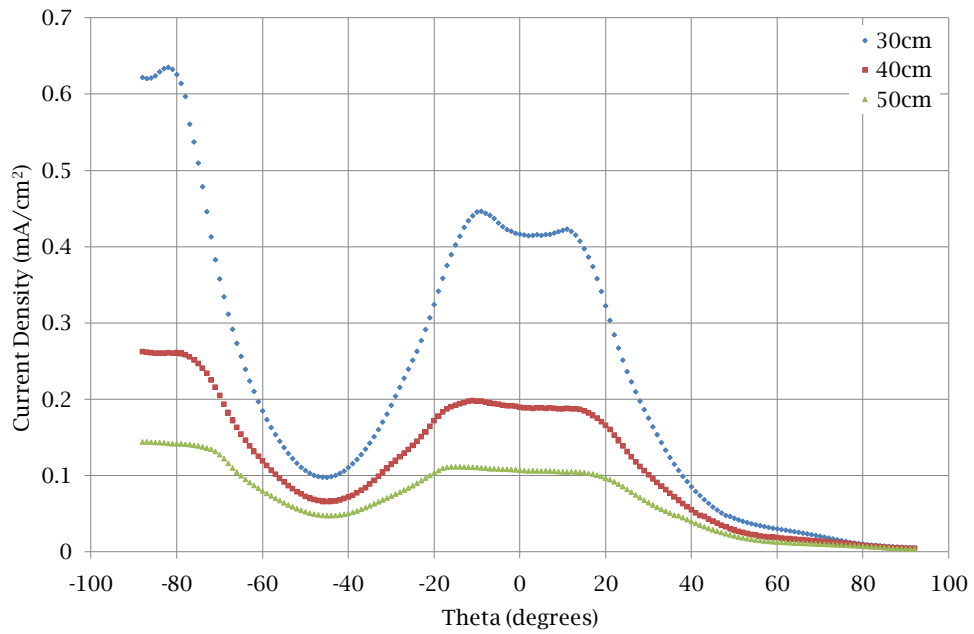


Figure 47: Current density for z-face, y and z-faces operating, in plane.

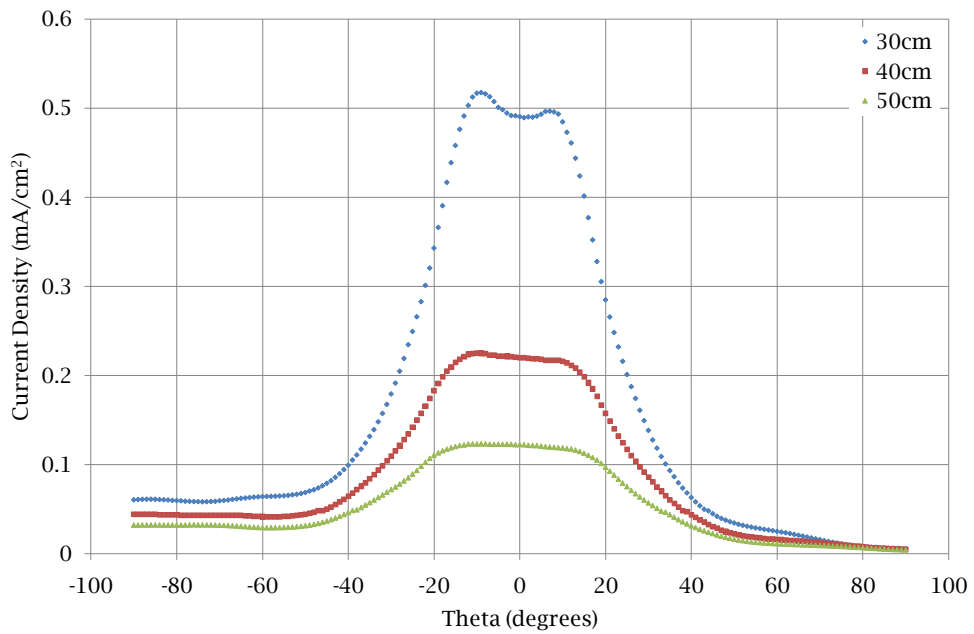


Figure 48: Current density for z-face, x and z-faces operating, 45 degrees out of plane.

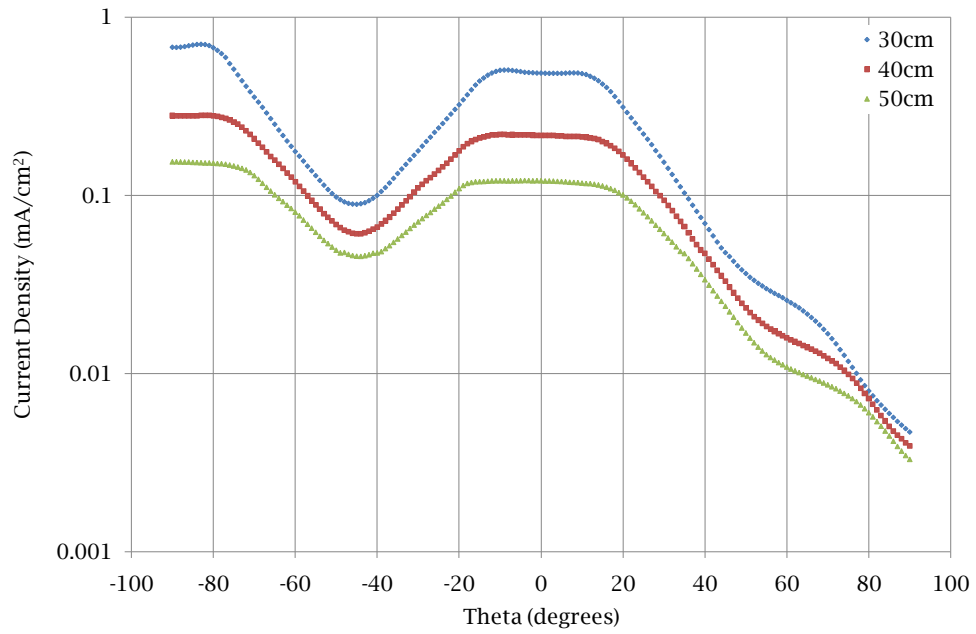


Figure 49: Current density for z-face, x and z-faces operating, in plane, logarithmic scale.

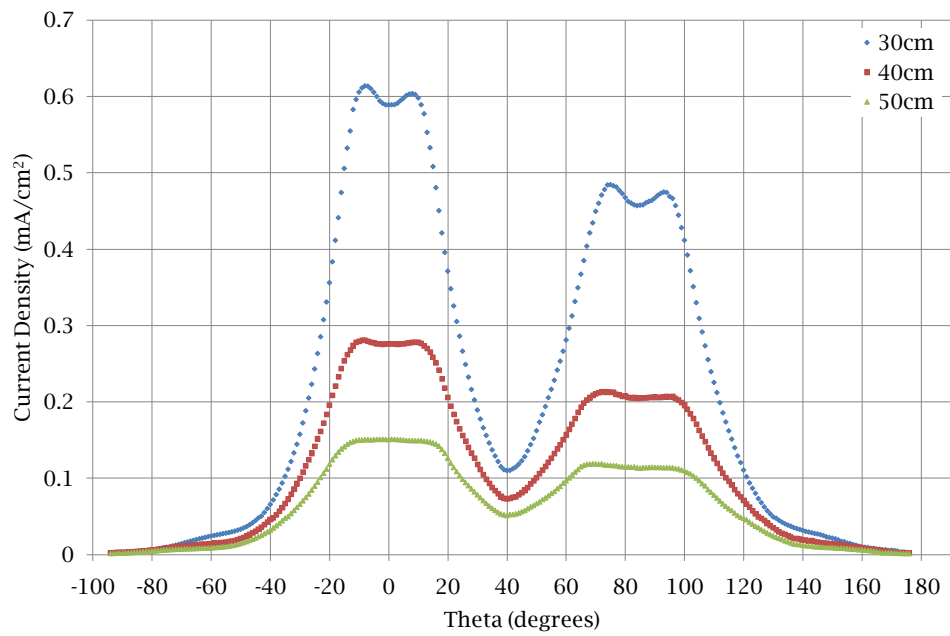


Figure 50: Current density for x and y-faces, double plume mode.

4.4.4 *Triple Plume Mode.* Results for triple plume operation followed the same trend observed between single and double plume modes. Peak current density for each face was increased and the distribution was more peaked. This effect is apparent in Figure 51 which shows the x and y-faces with theta centered on the x-face. The central hump at the peak in the 40 and 50 cm scans was likely a result of the tightly collimated central jet.

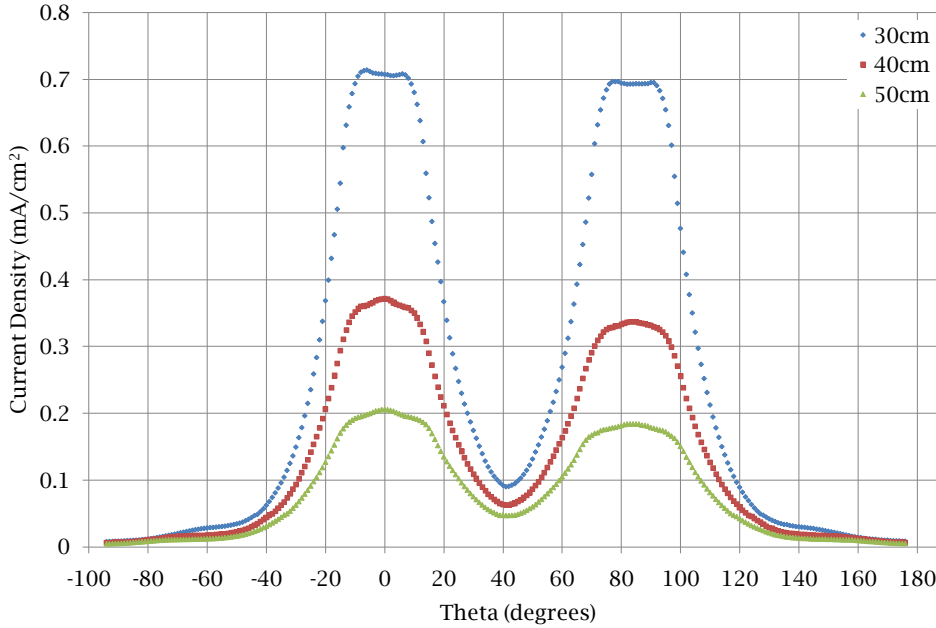


Figure 51: Current density for x and y-face, triple plume mode.

A direct comparison of the current densities for the x and y-faces at 30 cm is shown in Figure 52. Theta was centered on the x-face. Peak current density for the y-face was lower than the x-face in double plume mode, but they both increased to nearly the same value in triple plume mode. Compared to the y and z-face double plume mode shown in Figure 45 the y and x-face double plume mode showed a much lower peak current density for the y-face. The x-face was nearly the same in both cases. This result suggests the y-face operation is more strongly coupled to the z-face than the x-face is.

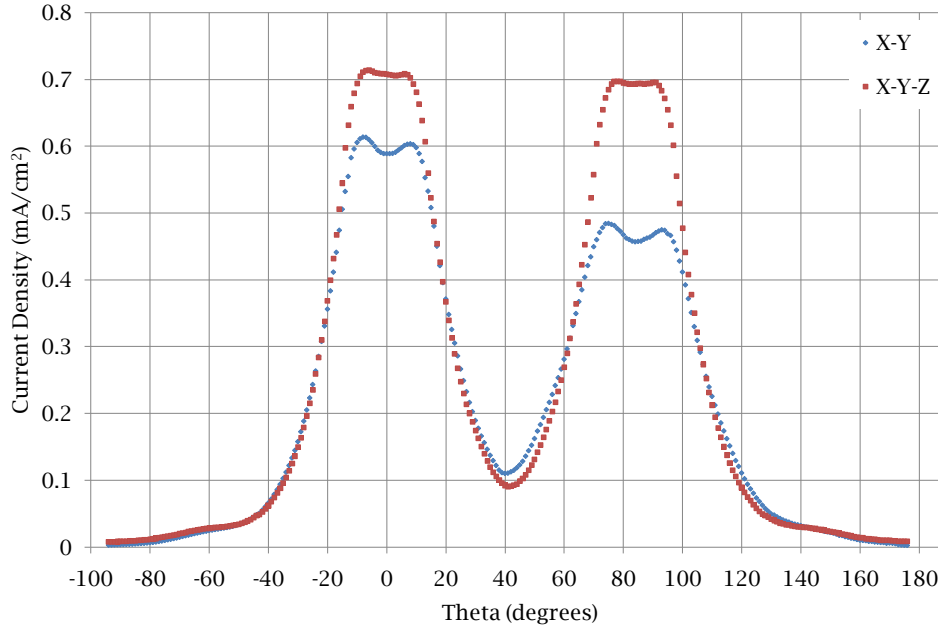


Figure 52: Comparison of current densities at 30cm for x and y-faces, double vs. triple plume.

A comparison of current densities for the x and y-faces in double and triple plume modes is shown in Figure 53. Theta was centered on the x-face. The sum of the curves for the double plume mode is also plotted, showing that the region between the two faces is approximated by this method. Although the x and y-faces operated at nearly the same peak current densities in triple plume mode, the z-face continued to display a lower peak current density than either. This difference is shown in Figures 54 and 55.

Figures 56 and 57 show a comparison of the 30 cm current densities for the x and y-faces in different operating modes. All of the trends discussed above were apparent. The transition from ball to jet plume with multiple faces operating, lower peak current densities for the y-face versus the x-face and an increase in peak current density and less divergent plume with each active face were all present.

The 30 cm mode comparison for the z-face is shown in Figure 58. This data covered the plane 45 degrees between the x and y-faces. In addition to the transition to jet plume and the increase in peak current density with more operating faces, the

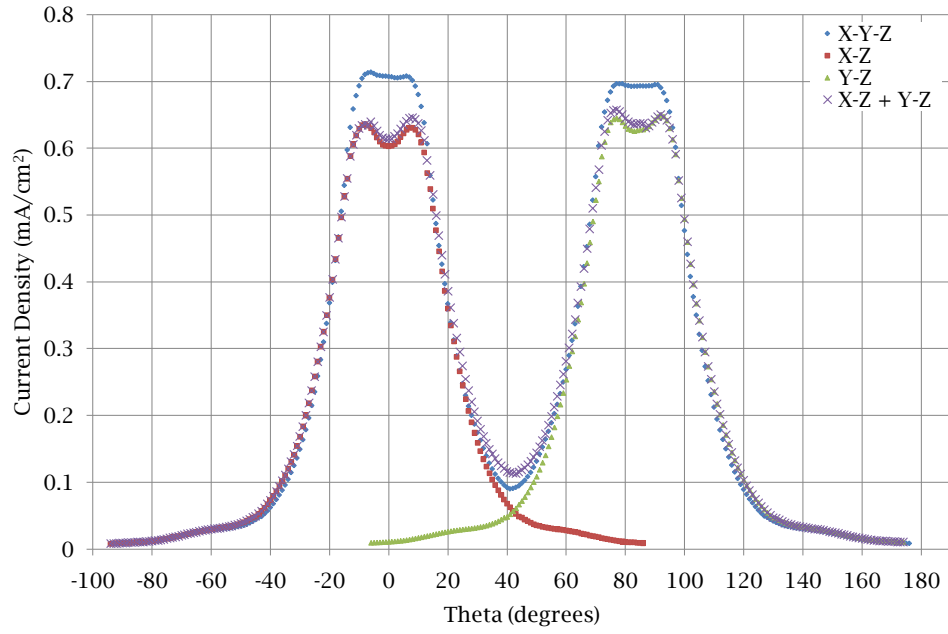


Figure 53: Comparison of current densities at 30 cm for x and y-faces.

region between the three faces could be observed. The current density in this region was slightly higher with the x-face operating over the y-face and was nearly twice as high with both operating.

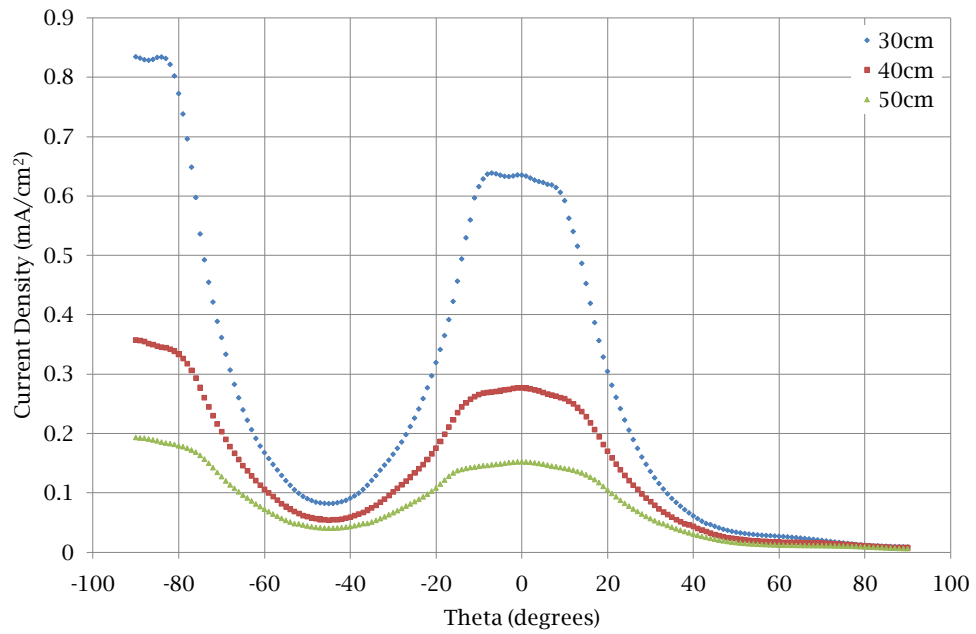


Figure 54: Current density for x and z-faces, triple plume mode, centered on z-face.

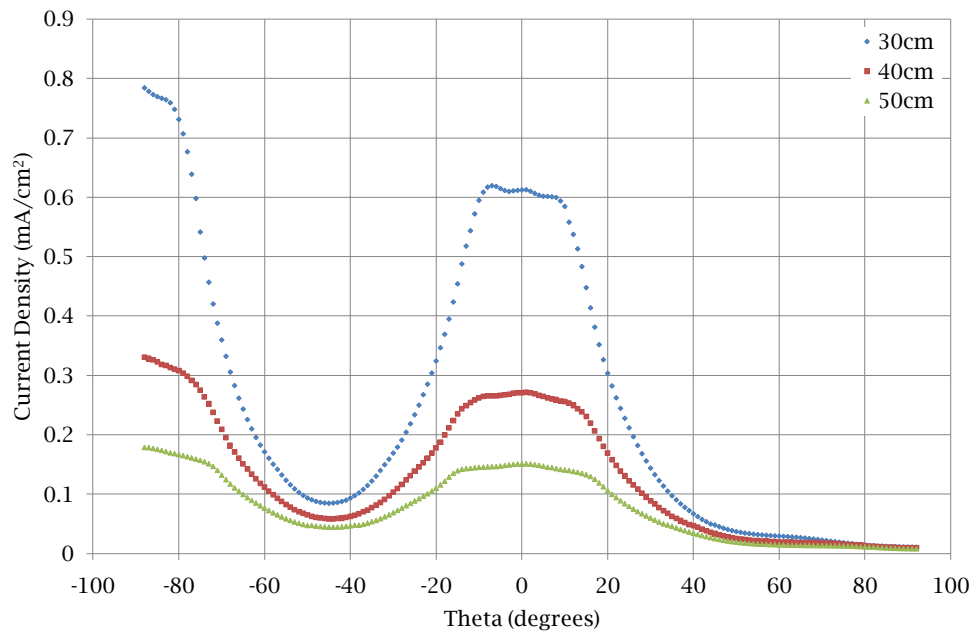


Figure 55: Current densities for y and z-faces, triple plume mode, centered on z-face.

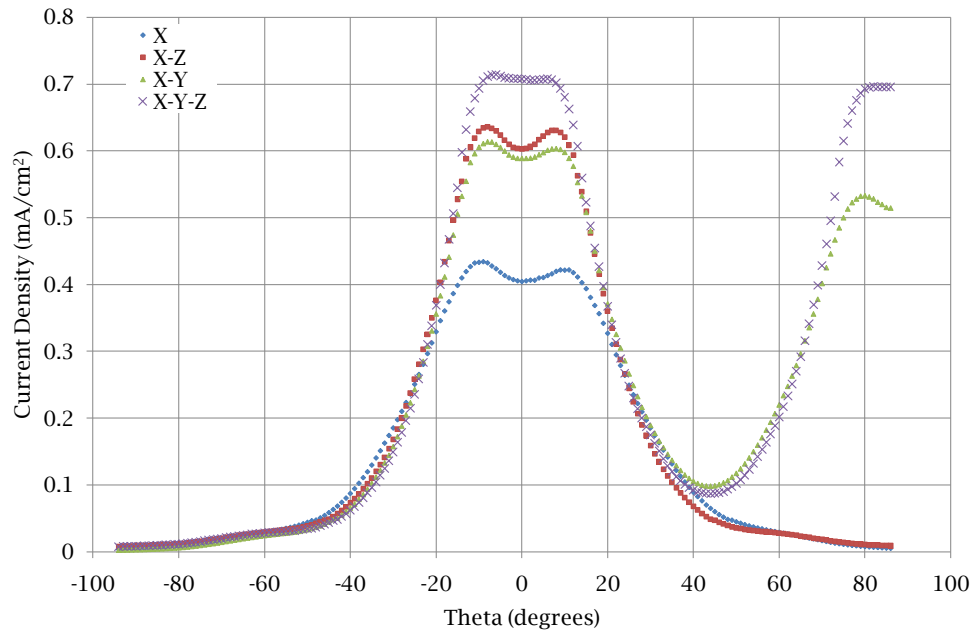


Figure 56: Comparison of current densities at 30 cm for x-face in different operating modes.

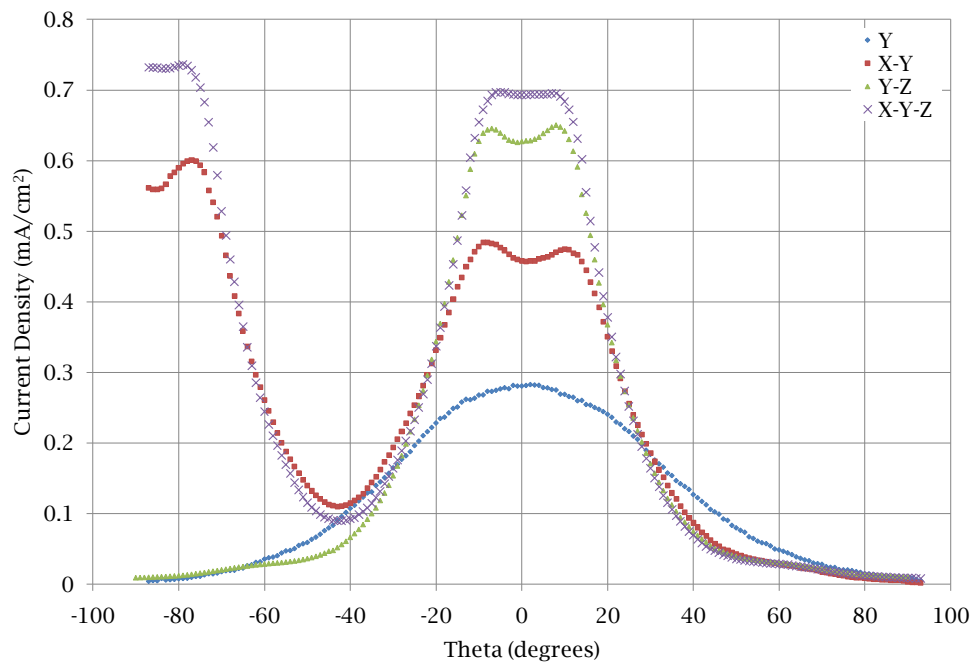


Figure 57: Comparison of current densities at 30 cm for y-face in different operating modes.

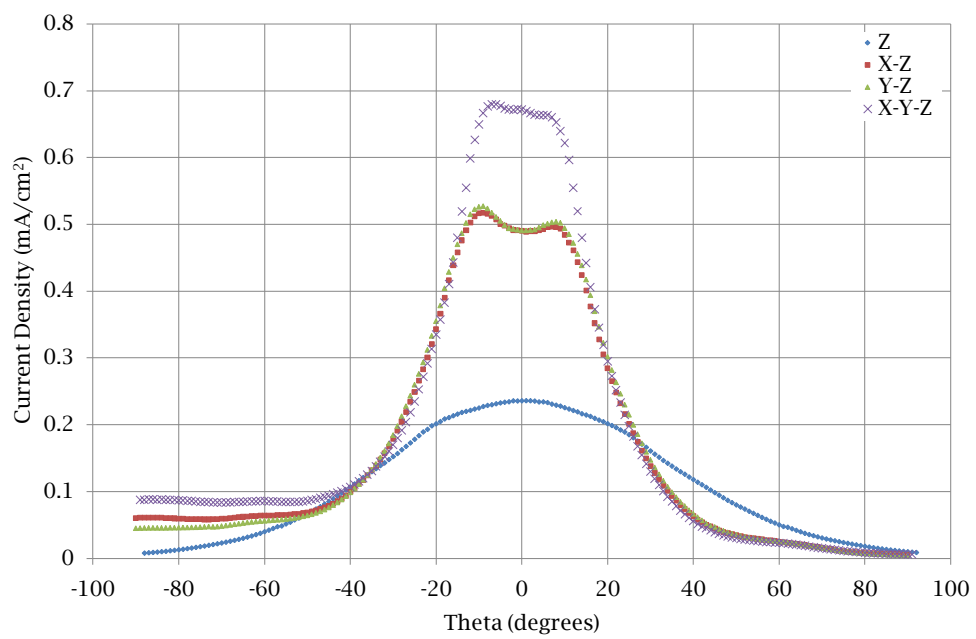


Figure 58: Comparison of current densities at 30 cm for z-face in different operating modes.

## V. Conclusions and Recommendations

### 5.1 Overview

This chapter presents preliminary conclusions resulting from this research and makes recommendations for further work with the three-axis thruster. Possible solutions to difficulties identified during this research are discussed along with methods to avoid other potential problems. Since the three-axis thruster is a prototype of a new concept in Hall effect thrusters a broad range of possibilities exist for further study.

All initial objectives of the research were met. The three-axis thruster was operated successfully in single, double and triple plume modes. Operating procedures and integration issues were identified and techniques to alleviate major difficulties were developed. Thrust measurements were conducted in single plume mode, although the design of the propellant manifold precluded multi-plume operation on the thrust stand. Thrust values show reduced performance and efficiencies compared to the baseline BHT-200. Faraday probe measurements of current density were conducted over a broad coverage range and show a less efficient, more divergent plume than the baseline BHT-200 thruster.

### 5.2 The Three-axis Thruster

Two immediate conclusions were apparent from the results. The first was that the three-axis thruster concept utilizing a common magnetic core is viable. The thruster operated successfully and produced thrust. The second was that the thruster did not operate well at this stage of development. Even though it shares a majority of working components with the well established BHT-200 thruster, its performance was considerably less efficient as characterized by the thrust stand and Faraday probe.

Faraday probe results and observations indicated that the x-face is the best performing of the three with noticeable advantages in divergence angle and current density over the other two. The y-face was only slightly better than the z-face. Further design refinements need to be made on the thruster to ensure all three faces operate at the same performance level. Since the three are identical in construction the difference

is attributed to magnetic field shaping and propellant flow control. In this design, a single magnetic coil, located at a central location may not be the best choice. Also, this thruster does not permit individual propellant flow control of each face.

Testing was conducted with the three anodes wired in parallel so that the same potential would be applied across all three. This potential was applied to all three faces even when one or two were not operating. The common magnet core also means that when the magnetic field was active for one face it was also active for all three. It is possible that some of the anode discharge current measured during single or double plume mode was due to electron current from the cathode at one of the non-operating anodes.

This effect may explain some of the increased discharge current variability observed in single and double face modes versus three face. It also may be the reason why the z-face appeared to operate less efficiently. Since it was located further from the cathode in the test configuration it is more likely that some of the electrons were drawn to the x and y-face anodes. Future measurements should be made with the individual anodes wired separately as much as possible so that differences in the faces can be properly quantified.

*5.2.1 Nominal Settings.* Part of these performance shortfalls may be due to differences in the actual optimal operating parameters for the new thruster. All measurements were taken while operating the thruster at nominal rates for the BHT-200 thruster. It is entirely possible, and even probable that the nominal rates for the three-axis thruster are different and that using settings more appropriate for this design may yield better results.

Most likely though the nominal settings, if different, will be very close to those for the BHT-200, suggesting that improvements in performance will only be slight. A brief comparison of magnet current versus anode discharge current for the three-axis thruster is shown in Figure 59. This technique is a common measure of magnet

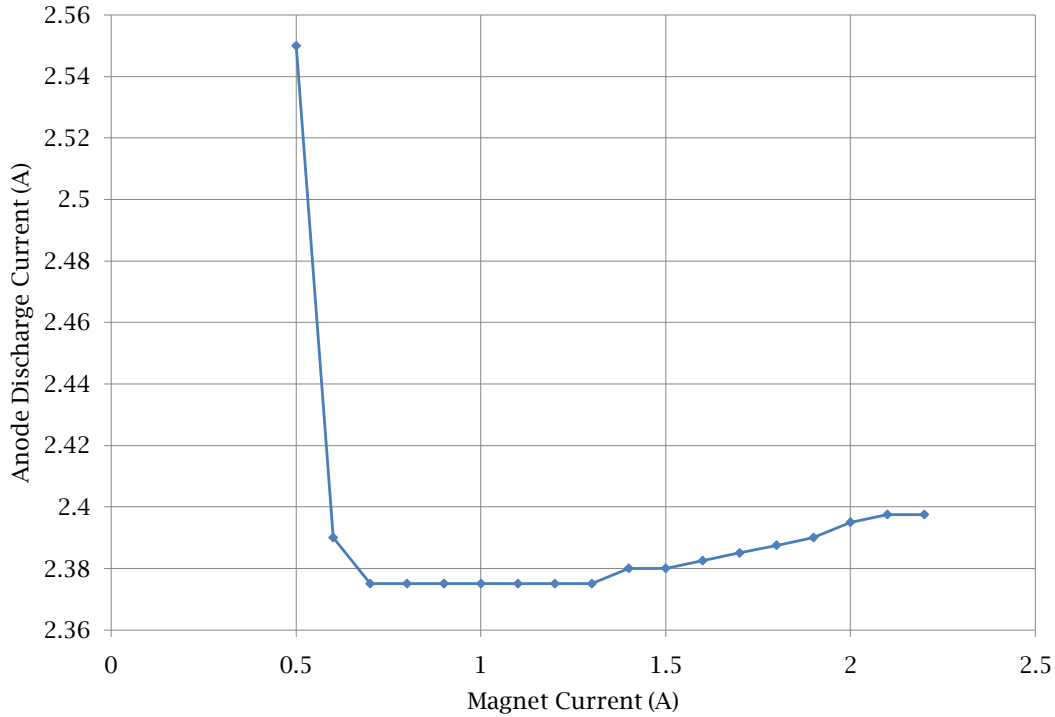


Figure 59: Three-axis thruster anode discharge current as a function of magnet current at constant propellant flow rates. All three faces operating.

current setting efficiency and shows an optimal setting of around 1 A, the same as BHT-200 nominal.

A logical next step would be to conduct a performance analysis of the thruster at different settings to identify the nominal operating parameters. This analysis would be helpful both as a baseline setting for future research and as an indicator of areas of design improvement for a more mature three-axis thruster design.

*5.2.2 Internal Cathode.* The internal cathode of the three-axis thruster did not operate properly. After the initial test run with the thruster it ceased to function at all. Indications are that its flush mounted keeper cap with the cathode internal to the thruster body is excessively prone to electrical shorts. Clearly a functioning internal cathode would be conducive to further work with the thruster.

Development testing at Busek suggests that the cathode was operated with a boron nitride spacer between the cathode heater/insert assembly and the keeper, but

this was omitted in the design used for testing. A similar modification was put forth as a solution during troubleshooting at AFIT. Some type of electrically insulating material between the cathode heater and keeper would most likely prevent the type of electrical shorts observed.

The unusual plasma ball discharge inside the thruster at high cathode flow rates is an area that may be investigated further. A cathode insulating insert may also prevent this type of problem by reducing the size of the gap between the keeper and the internal cathode assembly that allows propellant gas to accumulate inside the thruster body.

The internal cathode design on the test thruster was intended to be adjustable and the internal portion of the cathode could be retracted or extended to vary the clearance between the cathode and the keeper. With a fully operational cathode this feature may be used in future research to determine optimal placement of a single internal cathode. Clearly this is a whole field of evaluation in and of itself and could be incorporated into any of the other recommendations for further study listed here.

*5.2.3 External Cathode.* The three-axis thruster operated normally with a single external cathode. Cathode placement has the potential to greatly effect the performance of the thruster as a whole or individual faces and should be examined in further research. Optimal performance of the thruster may require a larger cathode or multiple cathodes.

The use of an external cathode naturally required that one face would be closer to the cathode than the other two. The position of the cathode relative to the thruster center was maintained throughout Faraday probe scans. This means, however, that it did move relative to each face when the thruster was rotated. During scans of the plane containing the x and y-faces the cathode was always located on the zero theta reference line, between the probe and thruster. During scans of the z-face the cathode was also located on the zero theta reference line, but rotated 90 degrees below the

plane compared to the x-y plane positioning. This positioning can be seen in Figure 14.

It was believed that placement of the cathode closer to one face would improve the performance of that face at the expense of the other two. The Faraday probe scans of the x and y-faces suggest otherwise. In both the y-centered scans, where the cathode was placed closer to the y-face, and the x-centered scans, with the cathode closer to the x-face, the x-face consistently showed higher beam current. It is probable that the inherent design inefficiencies of the thruster greatly overshadow the effects of cathode placement.

*5.2.4 Propellant Manifold.* The current propellant manifold for the thruster was bulky and heavy. Its size prevented it from being mounted on the thrust stand along with the thruster. Efforts should be made to develop a smaller and lighter assembly or to dispense with the propellant manifold entirely and use individual propellant lines to each face.

Since the manifold functioned only as an on/off switch to each face and did not individually meter flow the performance of individual faces of the thruster could not be characterized properly. With more than one face operating there was no way to tell how much of the total propellant flow was being routed from the manifold to each face. A method of metering or measuring the flow to individual faces via the manifold would make it a highly useful component, rather than just a way to turn the flow on and off. This functionality should be a priority for design improvement.

Future research at AFIT should utilize separate propellant lines to each face of the thruster rather than routing through the manifold wherever possible. Although two of the four available lines were not operable during this research, with all four lines functioning there will be one available to each face plus one for the cathode. Using this configuration propellant flow can be metered and measured through the mass flow controller readout.

### 5.3 Vacuum Chamber

In addition to the propellant flow issues inherent to the propellant manifold design the propellant flow interaction with the vacuum chamber also presents problems. The three-axis thruster presents different challenges with vacuum chamber configuration compared to a single thruster. Operating the three-axis thruster in the chamber is essentially the same as operating three separate thrusters in the chamber simultaneously with three different plume axes. This configuration presents issues with pumping rates and wall impingement.

*5.3.1 Chamber Size.* Although the SPASS lab vacuum chamber is relatively large, the unique nature of the three-axis thruster lends itself to study in an even larger chamber. Single thrusters are normally oriented to fire down the long axis of a cylindrical chamber. The orthogonal faces of the three-axis thruster prevent this, meaning that at least one of the faces is firing towards a chamber wall in all mounting configurations. Wall effects and backscatter then become a larger concern. A very large chamber where the thruster could be placed with the plasma plumes equidistant and as far from the walls as possible would be more ideal.

In addition to the influence that the multiple plumes may have on performance measurements, they also create a practical difficulty in chamber operation. With a single plume it is relatively easy to place equipment and fittings outside the firing arc of the thruster. With multiple plumes it becomes much more difficult to avoid firing high energy plasma at equipment inside the chamber. Plasma plume impingement has a high potential to degrade and shorten the life of equipment, wiring, etc. Extensive use of the three-axis thruster will most likely degrade the performance of the chamber and associated equipment much faster than even a much higher power single thruster.

*5.3.2 Pumping Rates.* A related problem is the higher propellant flow rates of the three-axis thruster compared to other low power thrusters. A higher pumping rate is needed to maintain chamber pressure. This problem is compounded by the

fact that pressure readings were unreliable when multiple faces of the thruster were operating. Pressure fluctuations of  $\pm 5 \times 10^{-5}$  torr were shown on the VacuumPlus readout during testing with three faces operating. It is possible that these were caused by erroneous pressure measurements as a result of the large volume of plasma in the chamber. It is also possible that these were localized effects near the pressure sensor or that chamber pressure actually fluctuated a great deal due to impingement of the plasma plume on a cryo-head. A larger test chamber could be expected to minimize any of these effects.

The three-axis thruster appeared to be fairly sensitive to chamber pressure. At all times during single face operation the thruster displayed the diffuse, ball type plume for all faces. This effect was apparent both through observation and the Faraday probe results. With multiple faces operating the plumes were generally of the collated, jet type which is associated with higher operating efficiency. This plume effect is almost certainly due to the increased chamber back pressure caused by the additional propellant flow. A true simulated space environment will not be possible for thrusters of this type unless a high level of vacuum is maintained.

#### ***5.4 Thrust Stand***

Thrust stand data was highly reproducible for the BHT-200 but less so for the three-axis thruster. A number of factors contributed to this and obvious solutions exist for most. Vibration and thermal effects are common to thrust stand measurements on all types of thruster. Certain design modifications could be made to minimize their influence. In addition other modifications could be made to improve thrust stand performance with the three-axis thruster specifically.

*5.4.1 Vibration Damping.* Further use of the thrust stand should involve efforts to increase the passive vibration damping of the stand. Isolation mounts for the stand could be easily constructed and may help to remove much of the random background vibration noise present during testing. This damping would allow more

precise measurements to be taken decrease the sample time required to get an accurate reading.

At times very loud environmental noises in the lab degraded sections of the thrust stand data. When long samples were required for calibration noises from pumps, slamming doors, etc. were not avoidable. Active damping only reduces the length of time the stand oscillates due to a large transient like this. Increased passive damping would reduce the amplitude as well for a much improved result.

*5.4.2 Thermal Effects.* Although thermal drift was not apparent as a major contributor in the thrust stand data, it remains a primary concern for future work. One mitigating strategy would be to directly measure the temperature of the thrust stand through thermocouples attached to various components, thermal imaging or other techniques. This technique may allow a calibration of the stand to determine the influence of thermal effects and a correction factor. Alternately it may help determine the rate of heating and cooling of the stand under operating conditions to help avoid thermal drift. Even simple temperature measurements would allow a quantification of the influence of thermal effects on the stand during a data run.

Similarly, to minimize thermal heating of the stand a higher output pump should be used with the thermal jacket. The NESLAB RTE7 used in this research to pump water to the jacket was capable, but the narrow tubing and serpentine cooling coils in the stand and jacket created a situation near the limit of its performance. An additional in-line boost pump or higher output unit would potentially increase the heat removal capacity of the thermal jacket.

*5.4.3 Future Study.* In addition to vibration and thermal effects the unique nature of the three-axis thruster presented its own issues. The thrust stand design is optimized for a single thruster with a single plume axis. It was not specifically designed for a larger thruster with three separate plume axes, but some modifications may improve its performance. A number of other tasks could be undertaken to im-

mediately continue study of the three-axis thruster using the lessons learned from its operation.

*5.4.3.1 Spring Replacement.* A requirement prior to reinstalling the three-axis thruster on the stand is replacement of the existing spring with a stiffer spring. The combination of low thrust and relatively high weight of the three-axis thruster is near the limit of the current spring's capabilities. A stiffer spring would increase the reproducibility of the calibration process while using higher mass thrusters. The total displacement measured by the thrust stand during operation would be less, but this will still be within the useful resolution of the LVDT.

*5.4.3.2 X and Z-Faces.* A logical next step is to conduct thrust measurements on the x and z-faces of the thruster. Since initial assumptions were that all faces were nearly identical the choice of the y-face for thrust measurements was somewhat arbitrary. Faraday probe data suggests that the y-face is in fact the *least* efficient of the three faces. Stand measurements of the other two faces would be expected to produce greater thrust.

*5.4.3.3 Multiple Face Operation.* Although only a single face was operated at a time during this research, it may be possible to operate multiple faces while measuring thrust on a single face. This procedure would allow study of the potential change in thrust caused by the activation or deactivation of other faces. The thrust stand LVDT measures only linear displacement along the thrust axis and the stand pedestal moves freely only along this axis. This feature should allow operation of two orthogonal faces in a horizontal plane with one aligned along the stand thrust axis. Any displacement of the stand pedestal perpendicular to the LVDT axis will be minimal and will not be recorded by the LVDT regardless.

Measurements of two faces aligned in a vertical plane is more problematic. Since the stand pedestal is configured as an inverted pendulum there is a very small amount

of vertical displacement of the stand combined with the linear motion. Therefore, any vertical thrust will be coupled with the horizontal thrust measurement of the stand.

Thrust stand propellant lines and electrical wiring harness are only configured for one thruster with attached cathode. This setup may require modification in order to operate multiple faces of the three-axis thruster while mounted on the stand. The size of the propellant manifold in its current configuration prevents it from being mounted on the stand pedestal without physical interference between it and the stand wiring harness during operation.

*5.4.3.4 Plume Mode.* If a convenient way could be found to ensure the plume operation in either the jet or ball mode over the duration of a thrust measurement one could compare the thrust produced by the two plume modes. Control of plume mode during single face operation was demonstrated by modulating chamber back pressure.

*5.4.4 Thrust Stand Modifications.* This research was the first extensive use of AFIT's T8 thrust stand to take measurements. As such, a number of improvements and modifications to the stand suggested themselves. These proposed changes incorporate operation with both the three-axis thruster and electric propulsion thrusters in general. This evaluation does not include material defects in the stand that were corrected during testing.

*5.4.4.1 LVDT Zeroing.* Standard operating procedure for the thrust stand required that the LVDT was manually zeroed before each set of measurements. This process involved inserting a long, thin tool with a hex head into a small hole in the back of the thermal jacket. The tool then had to be guided with much trial and error into the set screw for the LVDT core. By rotating the set screw the LVDT core could be moved to produce a zero reading on the LVDT controller readout. This adjustment ensured that the LVDT was centered in the linear range prior to calibration.

Unfortunately the act of inserting or removing the tool was enough to bump the LVDT out of zero. This, combined with the difficulty of engaging the set screw with the tool, made LVDT zeroing into a long and laborious process. The simple process of locking down the chamber door and pumping down also tended to cause enough displacement of the thrust stand to shift this zero position also.

An integral set screw knob or slider to reposition the LVDT core would avoid the need for a separate custom built tool and greatly streamline this process. Since the LVDT core is attached to the stand pedestal and is required to float freely within the LVDT collar it is probably easier to incorporate this adjustment into the fixed portion of the stand and move the collar rather than the core. Since the relative position of the core and collar is all that matters this would provide the same result. Ideally this system would incorporate a small motor which could be controlled from outside the vacuum chamber. Such a system would allow small adjustments to made even after the tank is sealed and evacuated.

*5.4.4.2 Wiring Harness and Propellant Lines.* Currently the stand wiring harness incorporates only six wires: three for the thruster and three for the cathode. To properly operate the three-axis thruster with separate anode wiring for each face requires five wires. The internal cathode requires another three. The propellant manifold has another four wires to control the propellant solenoids. This gives a sum total of twelve wires to mount a fully operational three-axis thruster on the stand. Operation in this configuration will require a second wiring harness or modification of the existing harness.

Operation of the three-axis thruster without the propellant manifold would require a separate line for each face plus one for the cathode. It is essential that these propellant lines are run internal to the stand to prevent interaction with the free movement of the stand pedestal. Addition of propellant lines to the the thrust stand would require major modifications and is not practical without essentially constructing a new stand.

*5.4.4.3 Leveling.* Stand leveling was conducted manually using a switch on the control box to control a stepper motor on the stand. This configuration allowed only imprecise control of the stand level. It could be zeroed initially before calibration, but could not be accurately adjusted if it drifted. Very small changes such as tank vibration or calibration weight loading and unloading were enough to cause measurable drift in stand level.

The stand level had a small, but measurable influence on the LVDT voltage readings. This effect may lead to a level drift error during measurement. If the inclinometer readings could be recorded and correlated with the voltage readings the inclination bias could be calibrated and corrected for.

An even better solution would be to incorporate a self-leveling circuit into the thrust stand. By removing the manual adjustment switch and replacing it with a feedback loop between the inclinometer and the leveler step motor the stand could be made self-leveling. This improvement would virtually eliminate any inclination drift error. A gain adjustment could provide fine tuning for any situation. Of all modifications suggested here this is probably the easiest to accomplish and requires only adjustments to the control box, not the stand itself.

*5.4.4.4 Null-type Stand.* The ideal situation for taking thrust measurements of the three-axis thruster would be a null-type thrust stand. These type of stands are of similar construction to the T8 stand but indirectly measure the force required to hold the pedestal in position rather than its displacement. Since the stand does not actually move to produce measurements multiple thruster faces could be operated simultaneously without the produced thrust being coupled to the measured axis. Use of a null-type stand may also avoid some of the spring problems associated with the use of heavier thrusters.

Null-type stands are in current usage and it may be possible to modify AFIT's thrust stand to operate on the same principles. It may even be possible to construct a

null-type stand which is capable of thrust measurements in multiple axes at the same time. This change is probably the most difficult modification proposed.

## **5.5 Faraday Probe**

The standard Faraday probe configuration produced useful data with no modification to the probe. Difficulties in taking Faraday probe measurements were primarily due to the geometry of the thruster and the need to scan over a three-dimensional coverage area encompassing multiple faces. Further Faraday probe measurements can be conducted using the same methodology to increase the coverage range or using modified techniques to examine the thruster performance more in depth.

*5.5.1 Correlated Thrust Measurements.* The original configuration of the thrust stand in the chamber had it mounted on the Aerotech translation stage. This arrangement allowed it to be aligned with the measurement plane of the Faraday probe for simultaneous thrust and Faraday probe measurements. It was discovered that movement of the Faraday probe translation stage caused vibration which was recorded by the thrust stand which degraded the data.

Additionally, the requirement for cooling water flow to both the thrust stand and Faraday probe beam profiler stage was beyond the capacity of the existing installation. Additional tank pass throughs and a second chill water loop would allow simultaneous operation on separate cooling circuits. This system would allow for the simultaneous operation of the beam profiler and thrust stand to provide for true correlation between the two measurement techniques.

*5.5.2 Coverage.* Only time constraints prevented the collection of additional Faraday probe sweeps. Using identical methodology the Faraday probe measurements begun in this research could be continued to give a full spherical current density map of the thruster plume. Other scan modes of the beam profiler system are available but were not used during this research. Specifically a linear scan mode is available

which could be used to map a grid rather than an arc. This scan mode may provide additional information on the plume structure and interaction.

The biggest difficulty in achieving full coverage of the multiple plume configuration was the need to open the chamber and manually reposition the thruster every time a new orientation was required. An additional rotation stage to combine with the Aerotech 3-axis linear stage has been a standing request as a chamber improvement. If such a stage had been available the requirement to open the chamber for thruster repositioning would have been reduced by about two-thirds.

A three-bar rigid linkage system for repositioning the thruster was in development when data collection terminated. This system would have connected a static thruster mount to the Aerotech translation stage via linkages. It was designed to convert the linear motion of the Aerotech stage into rotation of the thruster around either of two axes. This system would nearly eliminate the need to open the chamber for repositioning.

180 degree scans were conducted with the center of the thruster as the center of rotation. This reference enabled the use of the same center of rotation for all three faces. It may be preferable to use the center of the face being examined as the center of rotation. This reference system would provide a more true measurement of beam current but requires a different coordinate reference for each face.

*5.5.3 Bias Correction.* Faraday probe measurements are subject to bias due to collection of low energy charge exchange ions, backscatter ions and plume electrons. The design of the guarded probe is intended to minimize the collection of backscattered particles, but the multiple plumes of the three-axis thruster increases the probability of backscatter particles reaching the collector plate. One method future research could use to correct for this is to take a baseline backscatter measurement with the probe facing away from the thruster plume. This baseline backscatter current can then be subtracted from the measured beam current density.

Plume electrons collected by the probe would tend to reduce the measured beam current. Conversely charge exchange ions from the plume would raise the measured beam current since they are ionized in the plume and not at the anode. Increasing the negative probe guard bias will tend to repel these electrons. Increasing the collector plate positive bias will tend to repel charge exchange ions. Conducting a baseline scan using a thruster with a known beam current should allow adjustment of these values to collect only the actual beam current. These settings can then be used again for the experimental setup with a high confidence that any bias due to these effects are minimized in the measured beam current.

### ***5.6 Other Diagnostic Techniques***

Any of a range of commonly used diagnostic techniques employed on Hall effect thrusters could be applied to the three-axis thruster. Other equipment currently in use at AFIT which could be adapted to the current thruster installation include an ExB probe, an electrostatic analyzer (ESA) and a Langmuir probe. These instruments can be used to characterize ion charge distribution, ion energy distribution and plasma density, respectively.

Another technique that has been used on other Hall effect thrusters at AFIT is the use of thermal imaging cameras. This technique would be an excellent tool to use with the three-axis thruster. It was noticed that the three-axis thruster remained quite hot to the touch, even after it had been shut off for quite some time. With three thruster faces operating from a thruster assembly that is the same size as most small Hall effect thrusters a large amount of heat is produced and retained within the thruster. It is possible that excessive heating of the thruster over extended use with multiple faces running may cause material failures or degraded performance. Excessive component heating is a situation that should be explored thoroughly to determine if additional thermal management needs to be incorporated into future design refinements.

## *Appendix A. Background and Theory of Suggested Further Diagnostic Techniques*

Two of the proposed diagnostic techniques for further study of the three-axis thruster are currently available at AFIT. The Langmuir probe and electrostatic analyzer (ESA) are other well established diagnostic techniques that could be used to gather additional data on the three-axis thruster with minimal modification to the existing configuration. Plasma density values provided by the Langmuir probe could be used to further characterize the shape and nature of the plumes. Ion energy distribution from the ESA could be especially useful for identifying plume/plume interactions particularly in the regions between the plumes.

### ***A.1 Langmuir Probe***

Langmuir probes are a commonly used diagnostic techniques for plasmas. At its simplest, this device is simply a conducting electrode placed into the plasma. This probe is biased to a potential which is swept over negative and positive values compared to the plasma potential. Current is measured at each applied voltage value and a current-voltage (I-V) curve can be calculated. An example I-V curve is shown in Figure 60.

The current measured by the probe is due to both ions and electron currents. For the negatively biased probe electrons are repelled and the probe current is due to the ion current. This region is known as the ion saturation region. As the probe voltage is increased it passes a zero current point, which is known as the floating potential. Increasing voltage further it enters a region where high energy electrons can penetrate the potential difference to be collected at the probe while lower energy electrons are still repelled. This is the electron retarding region. At high probe potentials ions are repelled and electrons are collected by the probe. This is the electron saturation region. The plasma potential appears on the curve as a “knee” between the electron retarding and electron saturation regions. This plasma potential voltage occurs where there is no potential difference between the probe and the plasma [36].

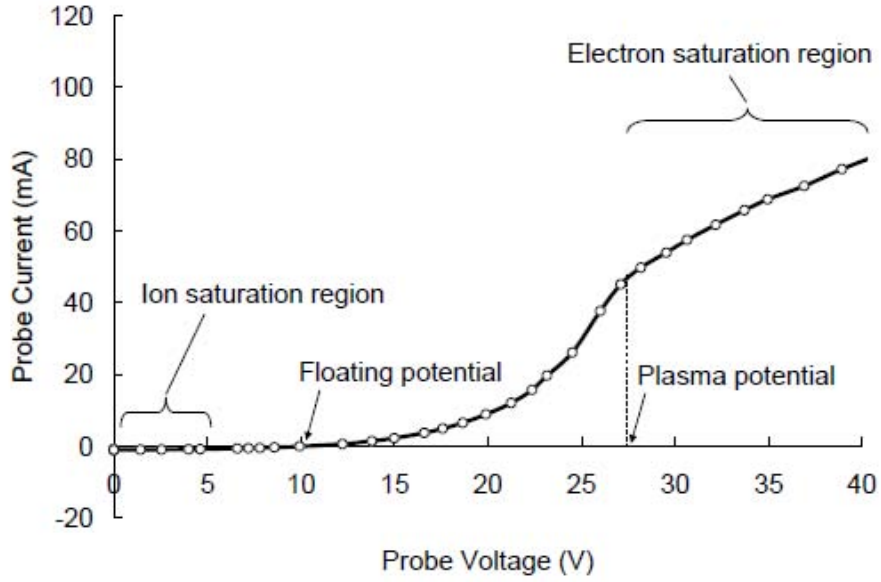


Figure 60: Typical Langmuir probe I-V curve [36].

A number of useful properties can be calculated from the I-V curve results. Electron temperature can be found from the exponential slope of the curve in the electron retardation region as shown in Equation 13.

$$\frac{k_B T_e}{e} = \left( \frac{d \ln(I_p)}{dV} \right)^{-1} \quad (13)$$

Once the electron temperature is known the electron density can be determined from the probe current in the ion saturation region as shown in Equation 14 where  $A_p$  is the probe area.

$$n_e = \frac{I_p}{A_p} \sqrt{\frac{2\pi m_e}{e^2 k_B T_e}} \quad (14)$$

Although Langmuir probes are a commonly used tool, they are not without their limitations. The physical presence of the probe in the plasma and its applied voltage can disturb the local plasma. A non-Maxwellian electron velocity distribution in the plasma invalidates some of the assumptions made in the above equations. The plasma potential “knee” is often poorly defined. Probe sizing is also important since

the analysis techniques used are dependent on the ratio of the probe radius to the Debye length. Debye length is shown in Equation 15.

$$\lambda_D = \sqrt{\frac{\epsilon_0 k_B T_e}{n_e q^2}} \quad (15)$$

## A.2 Electrostatic Analyzer

An electrostatic analyzer (ESA) is an instrument which separates ions by their energy to charge ratio. The working parts of the ESA are two curved, nested plates with applied voltage biases. Ions entering the analyzer experience an electrostatic force as a result. This force is proportional to the ion's charge state,  $z$ , and the electric field in that segment of the analyzer,  $\vec{E}_{seg}$ . This is shown in Equation 16.

$$\vec{F} = z \cdot q \cdot |\vec{E}_{seg}| \quad (16)$$

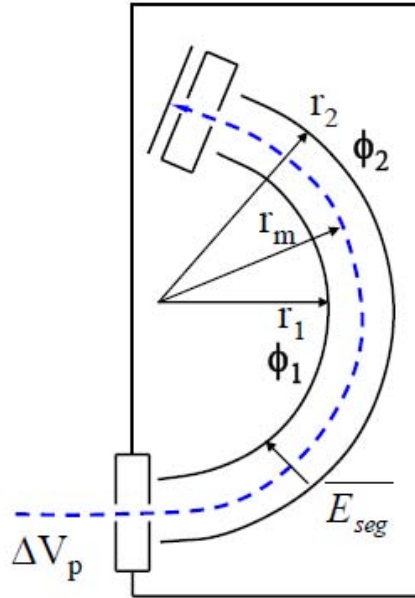


Figure 61: Diagram of an electrostatic analyzer configuration [36].

Since the channel of the ESA is curved, the electrostatic force acting on the ion must be balanced with the ion's velocity to allow it to negotiate the curve. This relationship is shown in Equation 17.

$$\vec{F} = \frac{m \cdot \vec{v}^2}{r_m} \quad (17)$$

Those ions that negotiate the channel end up at a collector plate on the far end of the curve. Clearly if an ion is moving too fast it will collide with the outer wall and if it are moving too slowly the electrostatic force will cause it to collide with the inner wall.

By relating the two equations it is possible to solve for the ion energy,  $E$ , in Equation 18, where  $\Delta V_p$  is difference between the potentials of the ion's creation point in the plasma and the entrance of the ESA [32].

$$E = z \cdot q \cdot \Delta V_p = \frac{1}{2} \cdot m \cdot v^2 \quad (18)$$

It is a simple matter to rearrange Equation 18 to get the velocity of the ion as in Equation 19.

$$v = \sqrt{\frac{2z \cdot q \cdot \Delta V_p}{m}} \quad (19)$$

Equations 18 and 19 can be set in spherical coordinates and solved to find  $\Delta V_p$  in terms of the ESA segment potential difference,  $\Delta\phi$ . This is shown in Equation 20.

$$\Delta V_p = \frac{\Delta\phi}{\frac{r_2}{r_1} - \frac{r_1}{r_2}} \quad (20)$$

Both  $r_1$  and  $r_2$  are only functions of the geometry of the ESA. This means it is possible to define the relationship between  $\Delta V_p$  and  $\Delta\phi$  by a constant which is a function only of the design of the ESA. Since this expression is not dependent on the charge or mass of the ion ( $z$  and  $m$  in Equations 18 and 19) the ESA is not able to differentiate

between different ion species. Also note that the ESA is only capable of detecting an ion's energy to charge ratio,  $E/z$ , not its absolute charge state.

## *Appendix B. Three-axis Thruster Operating Procedures*

The following procedures were used with the operation of the three-axis thruster. This procedure is for use with the solenoid operated propellant manifold and the anodes wired in parallel.

The three-axis thruster was operated with the external BHC-1500 cathode, but the same procedure is used for the internal cathode.

1. Ensure vacuum chamber pressure is below  $1 \times 10^{-6}$  torr.
2. Purge xenon propellant lines:
  - (a) Ensure xenon gas bottle is closed.
  - (b) Turn on MKS four-channel readout.
  - (c) Open flow controllers to anode and cathode.
  - (d) Open propellant regulator valve.
  - (e) Once flow rate drops below 1 sccm, close all valves and secure flow controllers.
3. Condition cathode.
  - (a) Turn on PPU power supply and cooling fans.
  - (b) Start BPU-600 host simulator interface.
  - (c) Set heater current to 2 A for 90 minutes.
  - (d) Set heater current to 4 A for 90 minutes.
  - (e) Set heater current to 6 A for 30 minutes.
  - (f) Turn off heater current.
4. Prepare propellant lines.
  - (a) Open xenon bottle valve.
  - (b) Set propellant regulator valve to 20 psi.

- (c) Open mass flow controller to cathode with 1 sccm flow rate set.
5. Light cathode.
- (a) Set cathode heater current to 6.5 A for eight minutes.
  - (b) Set cathode keeper current to 0.5 A.
    - i. Cathode ignition is indicated by a drop in keeper voltage.
    - ii. If keeper voltage stays at 650 V, cathode failed to break down. Reattempt.
  - (c) Turn off heater current once cathode is lit.
6. Light thruster.
- (a) Turn on propellant manifold solenoid valves to operating faces.
  - (b) Confirm valve position using indicator lights.
  - (c) Open mass flow controller to propellant manifold set for 10 sccm per operating face.
  - (d) Set discharge voltage to 100 V.
    - i. A purple glow discharge at the anode face indicates the thruster is lit.
    - ii. It is possible for not all thruster faces to light. If this occurs, power off and reattempt.
    - iii. If thruster faces repeatedly fail to light, ensure propellant manifold valves are open and cathode is operating. Increased xenon flow may assist.
7. Collimate plume.
- (a) Set magnet current to 1 A.
  - (b) If increased xenon flow was used to light thruster, reduce flow to 10 sccm per operating face.
  - (c) Gradually increase anode discharge voltage from 100 V to 250 V.

- (d) Adjust xenon flow to achieve discharge current of 0.8 A per operating face.
- 8. Run thruster for 30 minutes or as long as necessary to stabilize. Adjust xenon flow to fine tune discharge current.
- 9. Conduct testing. Monitor chamber back pressure.
- 10. Deactivating operating thruster faces.
  - (a) Reduce xenon flow to that required for reduced number of faces.
  - (b) Turn off propellant manifold solenoid switch to face(s) to be shut off.
  - (c) Secured face(s) will extinguish when propellant is secured.
    - i. Discharge current will spike low as face extinguishes and then recover to previous level.
  - (d) Readjust propellant flow to achieve discharge current of 0.8 A per operating face.
- 11. Activating unlit thruster faces.
  - (a) Turn on propellant manifold solenoid switch to face(s) to be lit.
  - (b) Activated face(s) will light when they receive xenon flow, nearly immediately.
    - i. Discharge current will spike high as face lights and then recover to previous level.
    - ii. If face fails to light, turn off solenoid switch, then reattempt.
  - (c) Readjust propellant flow to achieve discharge current of 0.8 A per operating face.
- 12. Securing thruster.
  - (a) Secure power to anode, magnets and keeper.
  - (b) Secure xenon flow to the propellant manifold and cathode.
  - (c) Close xenon bottle.

- (d) Shut off BPU-600 software and turn off PPU power supply and cooling fans.
13. If restoring the chamber to atmospheric pressure ensure dry nitrogen is used to back fill, in order to reduce the chances of poisoning the cathode.

### *Appendix C. Faraday Probe Data*

Faraday probe data collection consisted of two scan profiles for each face. All readings were taken at one degree increments on a constant radius arc centered on the thruster face centerline. Scan radii ranged from 30 to 100 cm in 10cm increments. Full 180 degree arc coverage,  $\pm 90$  degrees of centerline, was conducted from 30 to 50 cm. Longer range scans were also conducted from 30 to 100 cm radii with varying arc coverage of less than 180 degrees due to travel constraints of the beam profiler translation stage system. Probe collector plate was biased to +20 V for all scans. Probe guard body was biased to -20 V.

X-face	
Single plume mode	
180 degree arc, 30-50 cm radii	Figure 62 on page 107
50-100 cm radii	Figure 63 on page 107
Double plume mode	
(x and y), 180 degree arc, 30-50 cm radii	Figure 64 on page 108
(x and y), 30-100 cm radii	Figure 65 on page 108
(x and z), 180 degree arc, 30-50 cm radii	Figure 66 on page 109
Triple plume mode	
180 degree arc, 30-50 cm radii	Figure 67 on page 109
30-100 cm radii	Figure 68 on page 110
Y-face	
Single plume mode	
180 degree arc, 30-50 cm radii	Figure 69 on page 110
30-100 cm radii	Figure 70 on page 111
Double plume mode	
(x and y), 180 degree arc, 30-50 cm radii	Figure 71 on page 111
(x and y), 30-100 cm radii	Figure 72 on page 112
(y and z), 180 degree arc, 30-50 cm radii	Figure 73 on page 112
Triple plume mode	
180 degree arc, 30-50 cm radii	Figure 74 on page 113
30-100 cm radii	Figure 75 on page 113

Centered 45 degrees between x and y-face	
Double plume mode	
(x and y), 180 degree arc, 30-50 cm radii	Figure 76 on page 114
(x and y), 30-100 cm radii	Figure 77 on page 114
Triple plume mode	
180 degree arc, 30-50 cm radii	Figure 78 on page 115
30-100 cm radii	Figure 79 on page 115
Z-face: Plane containing x-face	
Single plume mode	
180 degree arc, 30-50 cm radii	Figure 80 on page 116
30-100 cm radii	Figure 81 on page 116
Double plume mode	
(x and z), 180 degree arc, 30-50 cm radii	Figure 82 on page 117
(x and z), 30-90 cm radii	Figure 83 on page 117
Triple plume mode	
180 degree arc, 30-50 cm radii	Figure 84 on page 118
30-90 cm radii	Figure 85 on page 118
Z-face: Plane containing y-face	
Double plume mode	
(y and z), 180 degree arc, 30-50 cm radii	Figure 88 on page 120
(y and z), 30-100 cm radii	Figure 89 on page 120
Triple plume mode	
180 degree arc, 30-50 cm radii	Figure 90 on page 121
30-100 cm radii	Figure 91 on page 121
Z-face: Plane 45 degrees between x and y-face	
Single plume mode	
180 degree arc, 30-50 cm radii	Figure 92 on page 122
30-90 cm radii	Figure 93 on page 122
Double plume mode	
(x and z), 180 degree arc, 30-50 cm radii	Figure 94 on page 123
(y and z), 180 degree arc, 30-50 cm radii	Figure 95 on page 123
Triple plume mode	
180 degree arc, 30-50 cm radii	Figure 96 on page 124
30-100 cm radii	Figure 97 on page 124

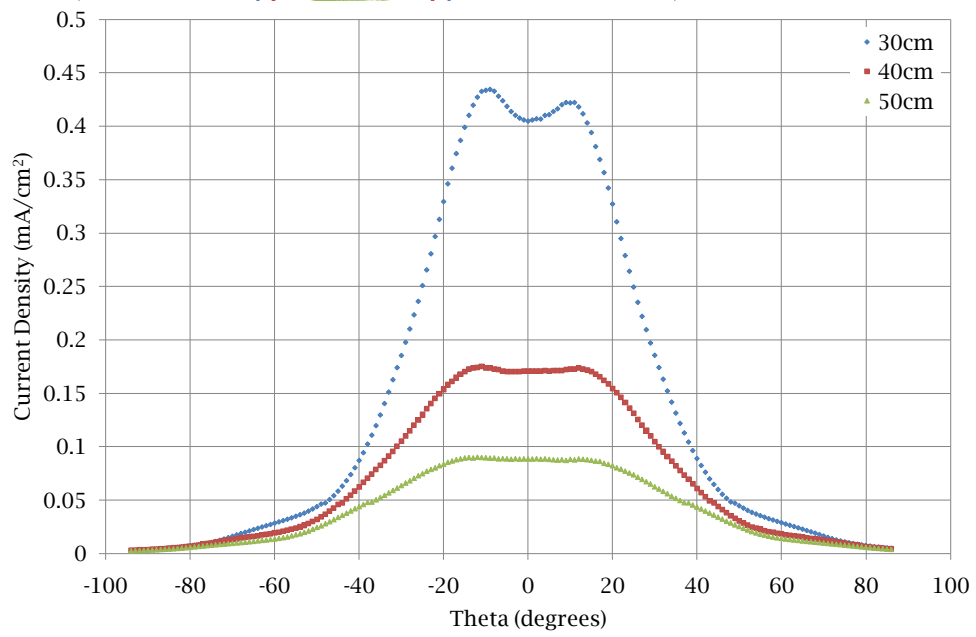


Figure 62: X-face: Single plume mode, 180 degree arc, 30-50 cm radii.

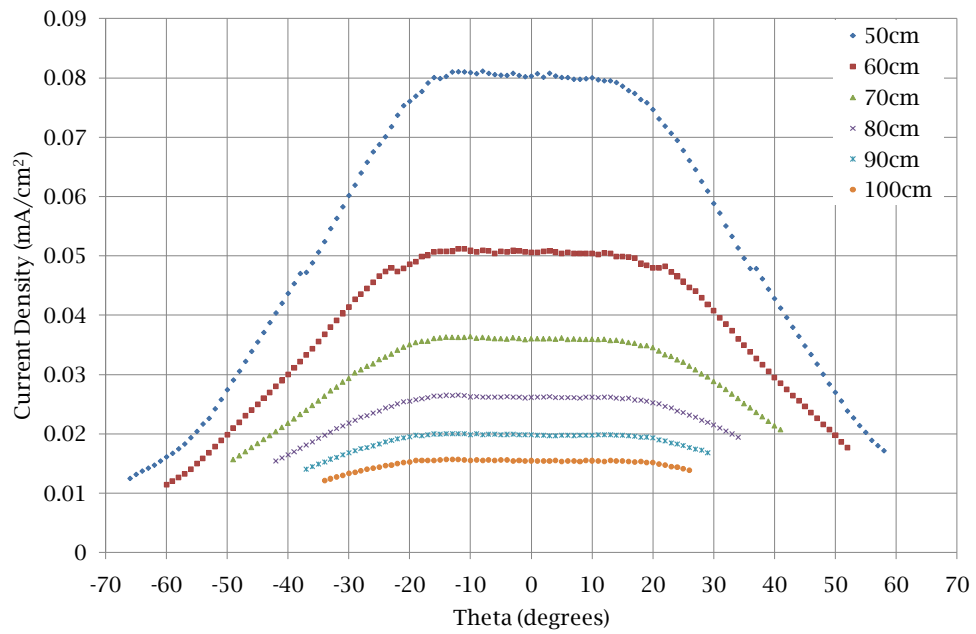


Figure 63: X-face: Single plume mode, 50-100 cm radii.

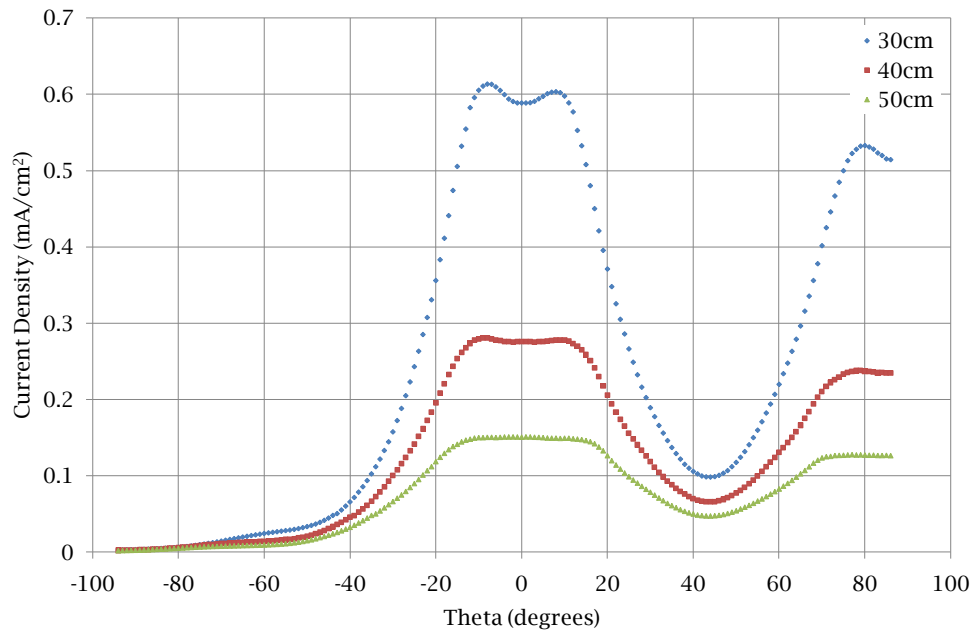


Figure 64: X-face: Double plume mode (x and y-faces operating), 180 degree arc, 30-50 cm radii.

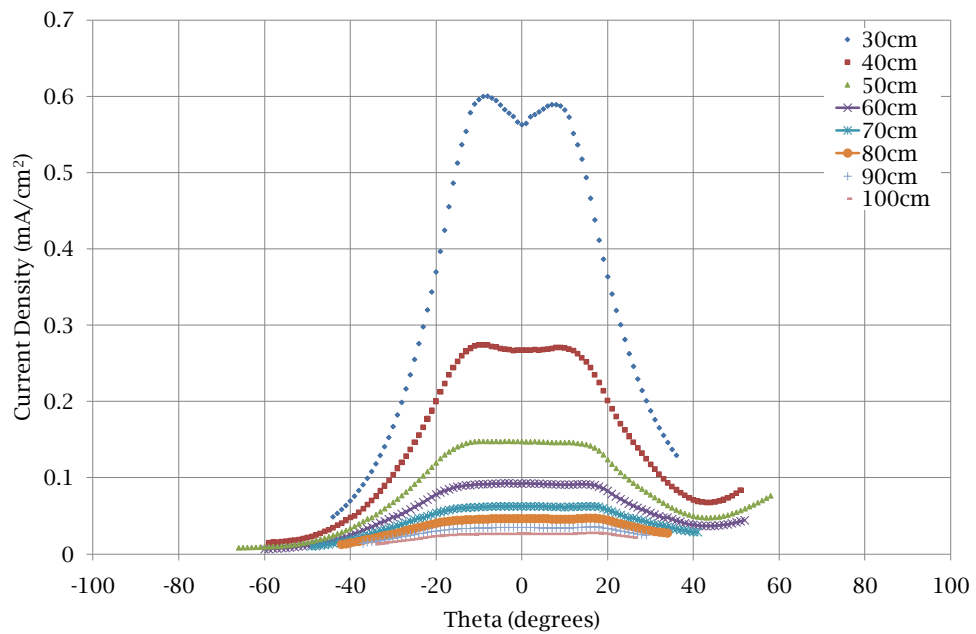


Figure 65: X-face: Double plume mode (x and y-faces operating), 30-100 cm radii.

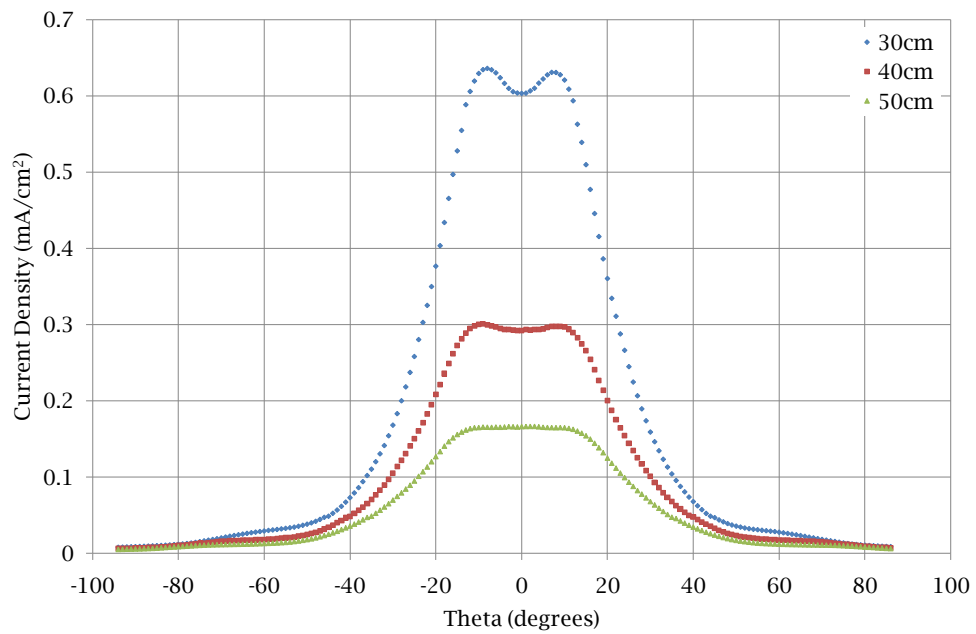


Figure 66: X-face: Double plume mode (x and z-faces operating), 180 degree arc, 30-50 cm radii.

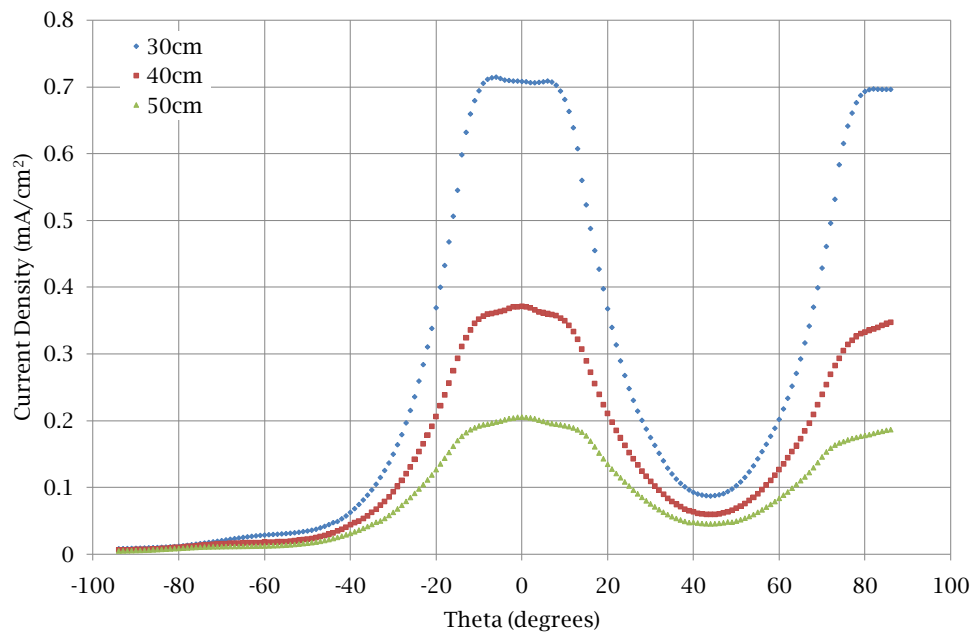


Figure 67: X-face: Triple plume mode, 180 degree arc, 30-50 cm radii.

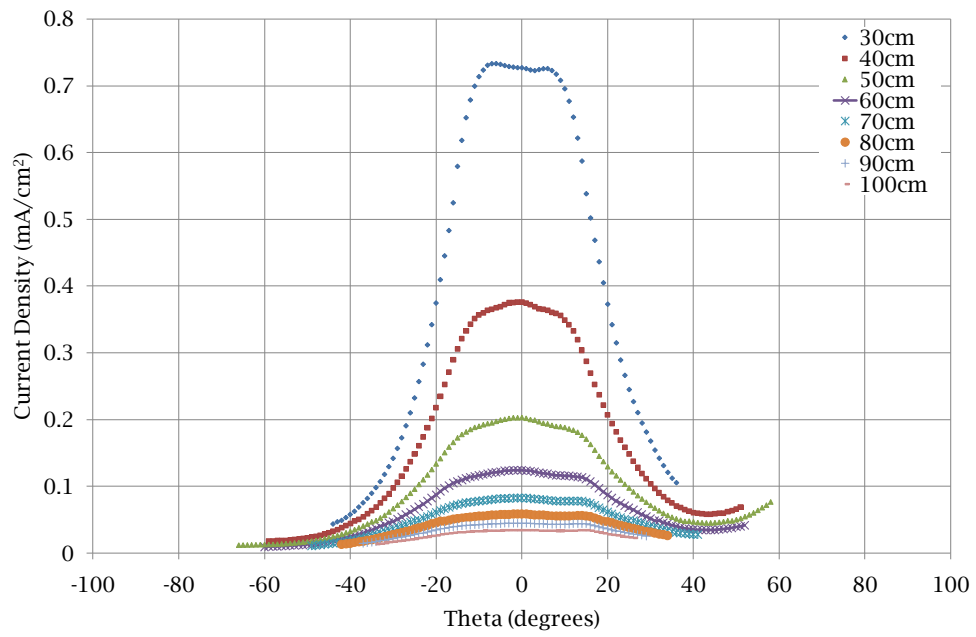


Figure 68: X-face: Triple plume mode, 30-100 cm radii.

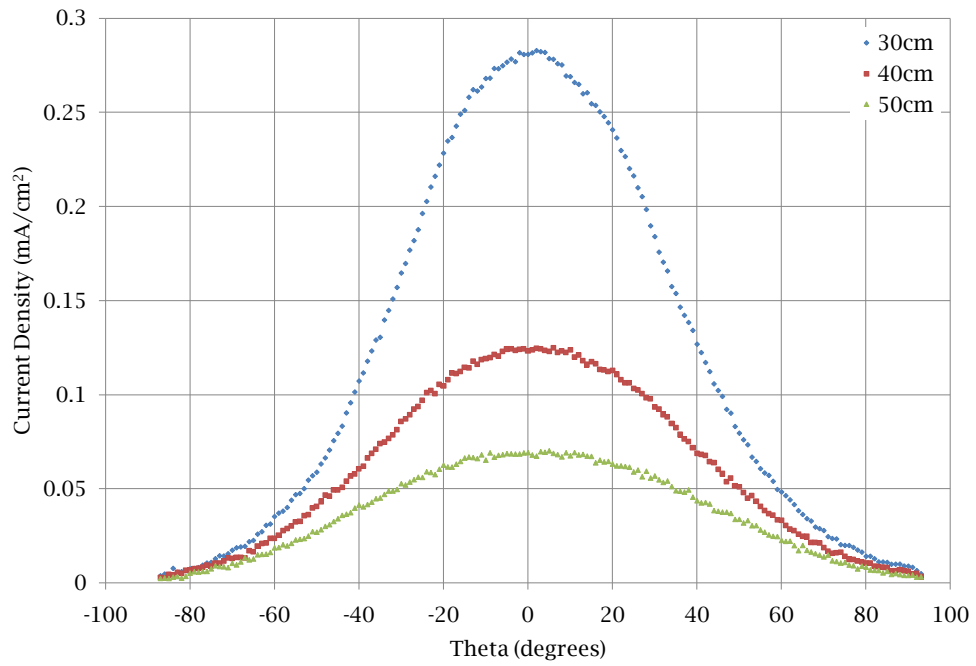


Figure 69: Y-face: Single plume mode, 180 degree arc, 30-50 cm radii.

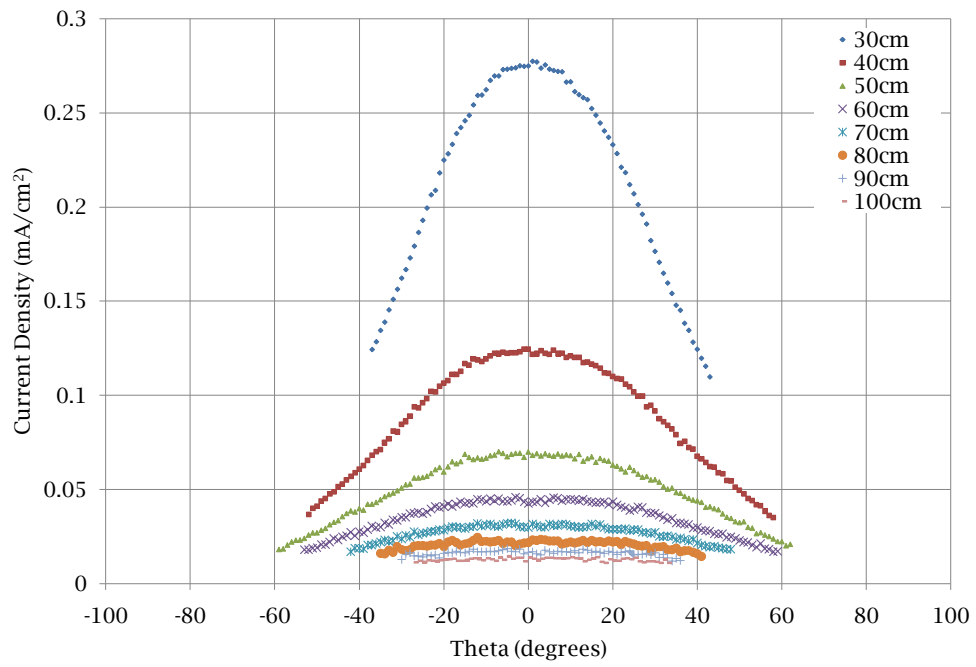


Figure 70: Y-face: Single plume mode, 30-100 cm radii.

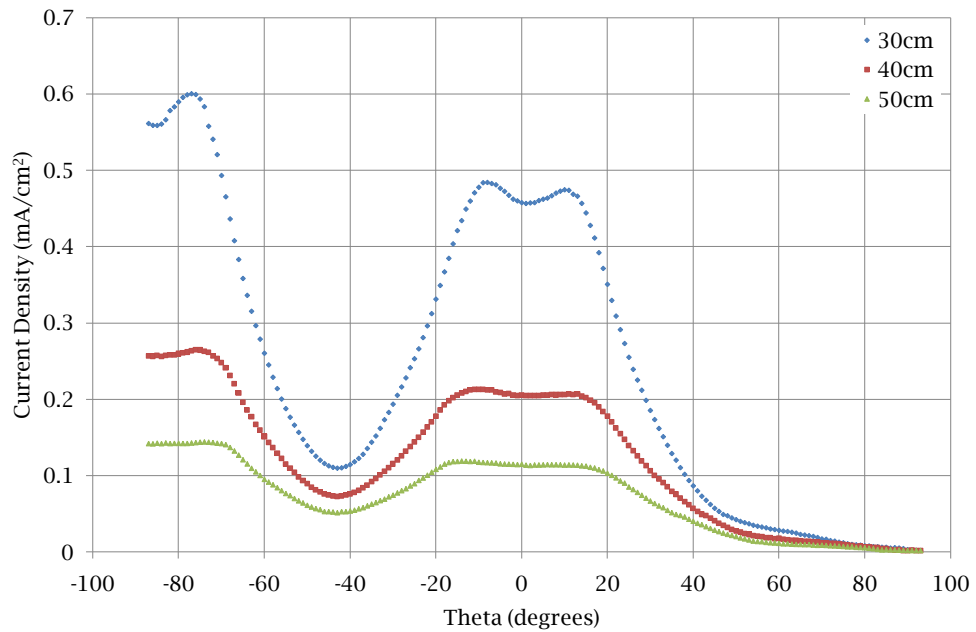


Figure 71: Y-face: Double plume mode (x and y-faces operating), 180 degree arc, 30-50 cm radii.

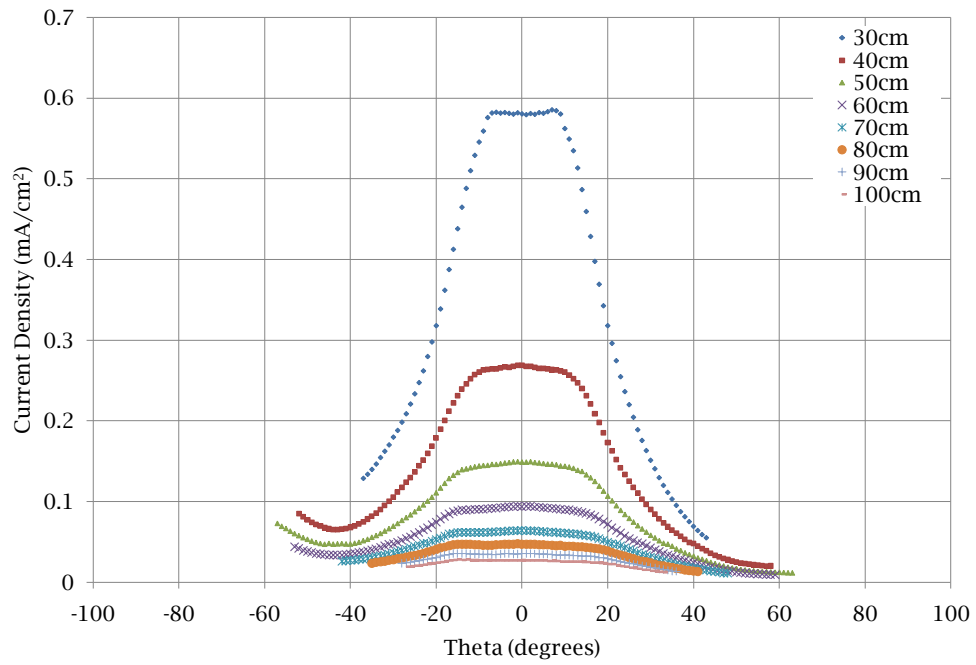


Figure 72: Y-face: Double plume mode (x and y-faces operating), 30-100 cm radii.

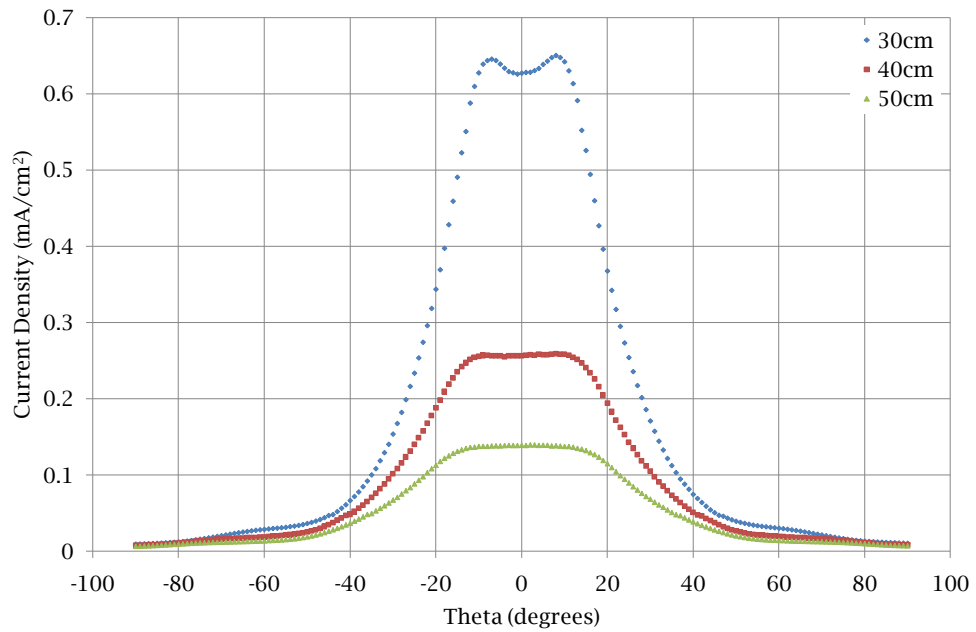


Figure 73: Y-face: Double plume mode (y and z-faces operating), 180 degree arc, 30-50 cm radii.

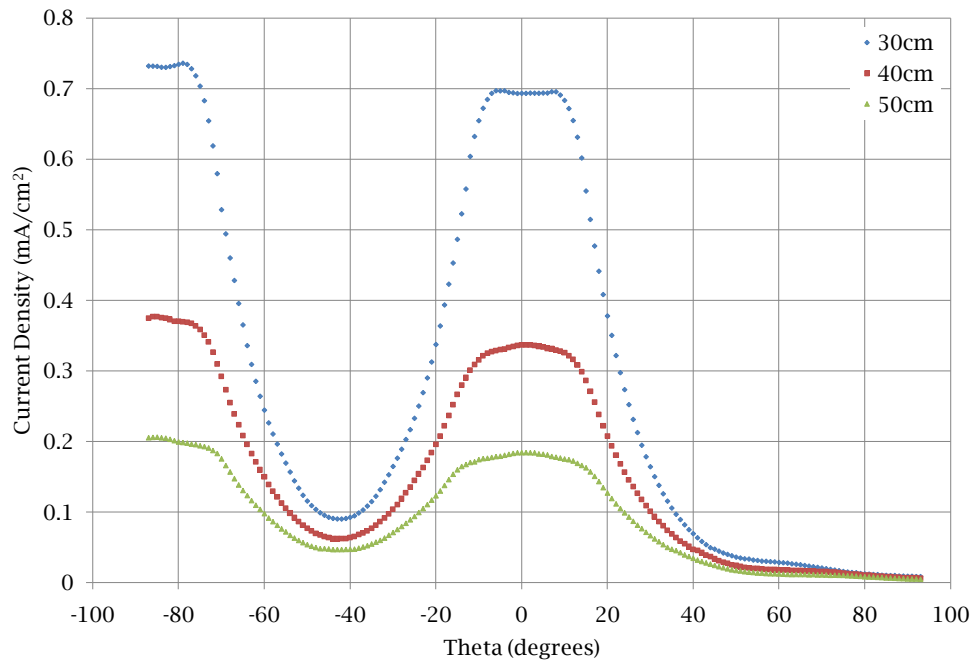


Figure 74: Y-face: Triple plume mode, 180 degree arc, 30-50 cm radii.

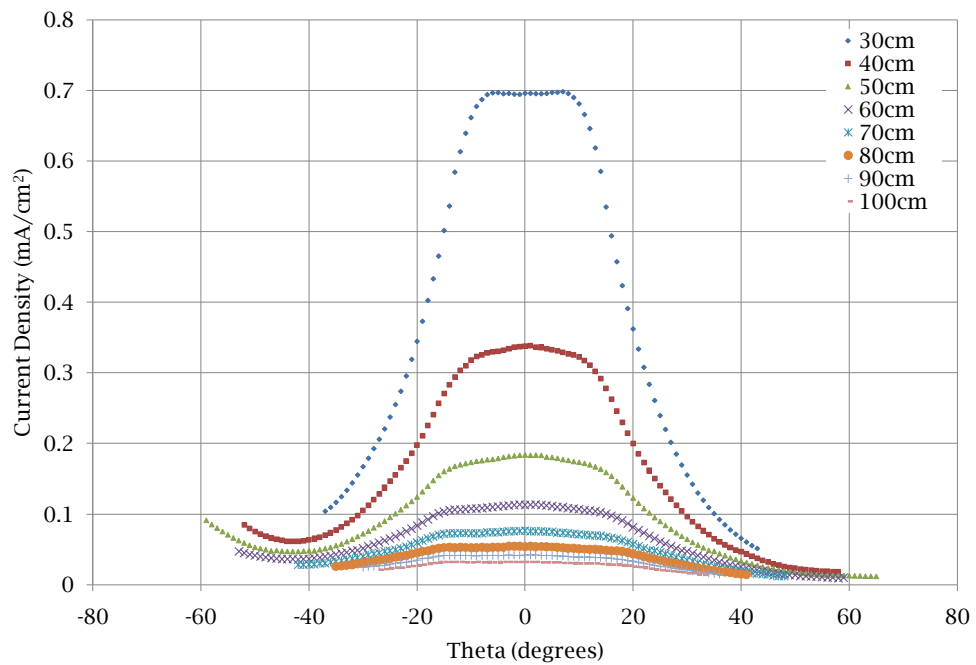


Figure 75: Y-face: Triple plume mode, 30-100 cm radii.

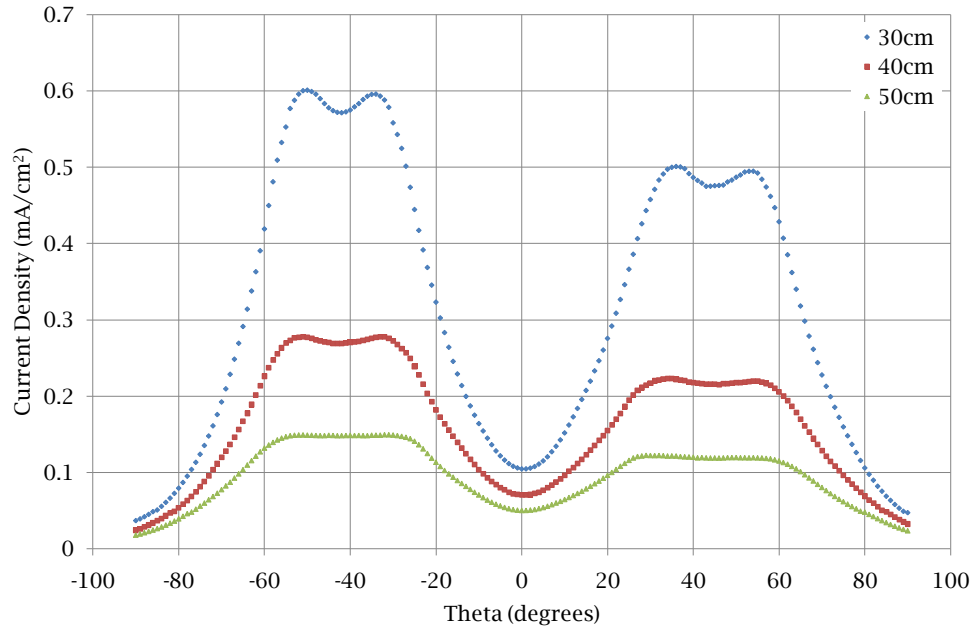


Figure 76: Centered 45 degrees between x and y-face: Double plume mode (x and y-faces operating), 180 degree arc, 30-50 cm radii.

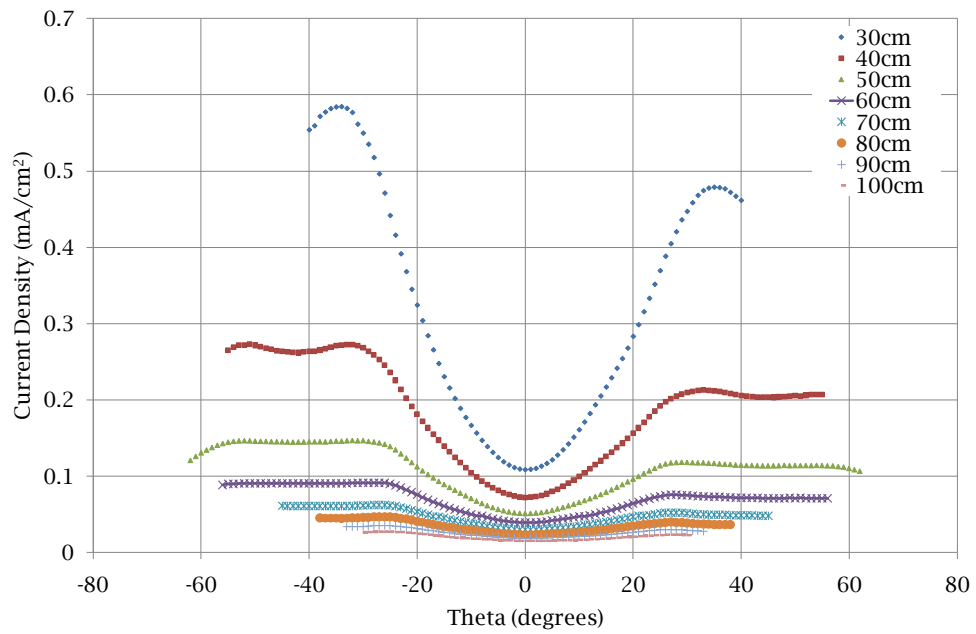


Figure 77: Centered 45 degrees between x and y-face: Double plume mode (x and y-faces operating), 30-100 cm radii.

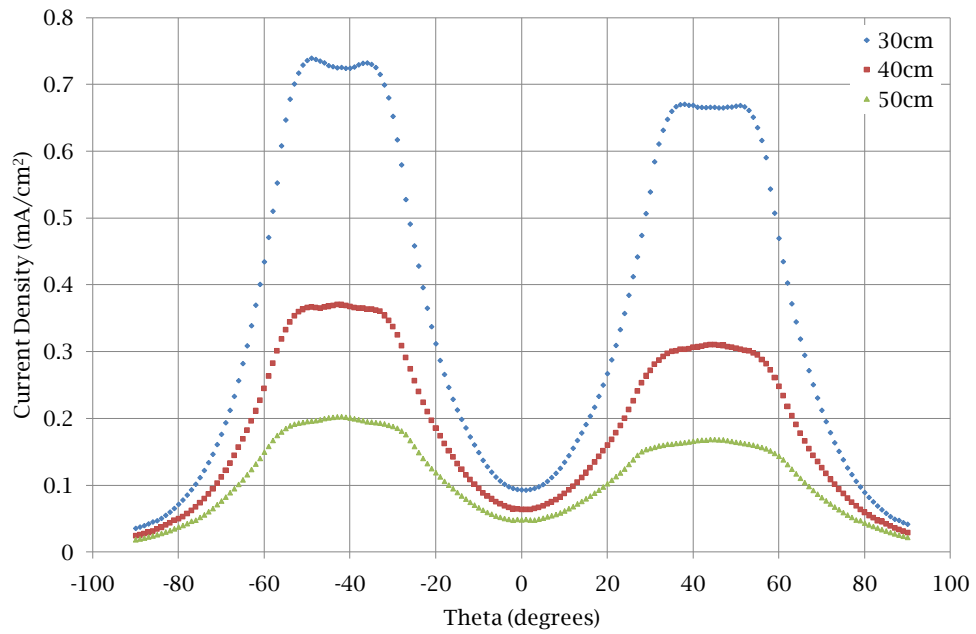


Figure 78: Centered 45 degrees between x and y-face: Triple plume mode, 180 degree arc, 30-50 cm radii.

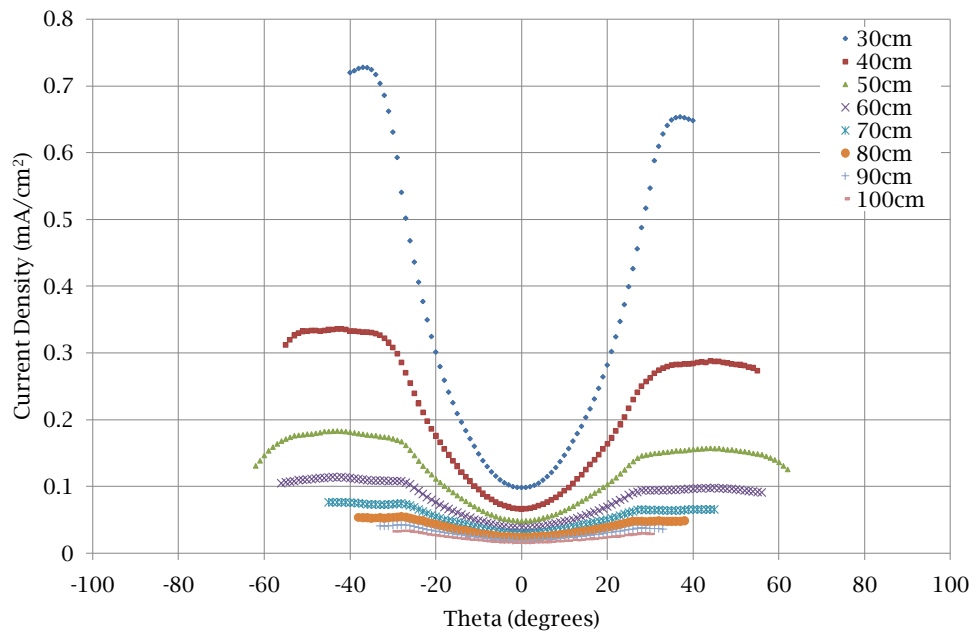


Figure 79: Centered 45 degrees between x and y-face: Triple plume mode, 30-100 cm radii.

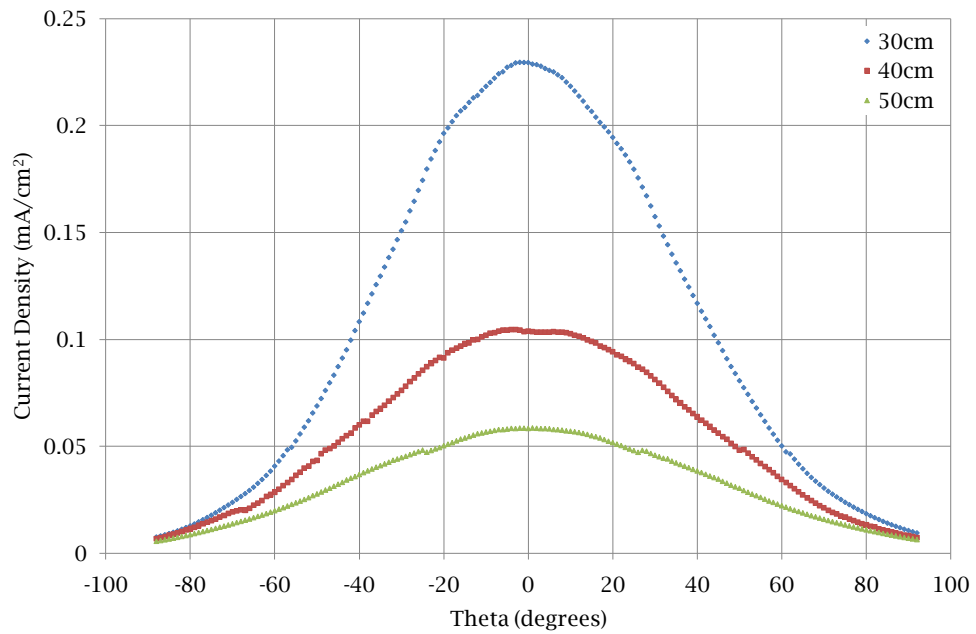


Figure 80: Z-face (plane containing x-face): Single plume mode, 180 degree arc, 30-50 cm radii.

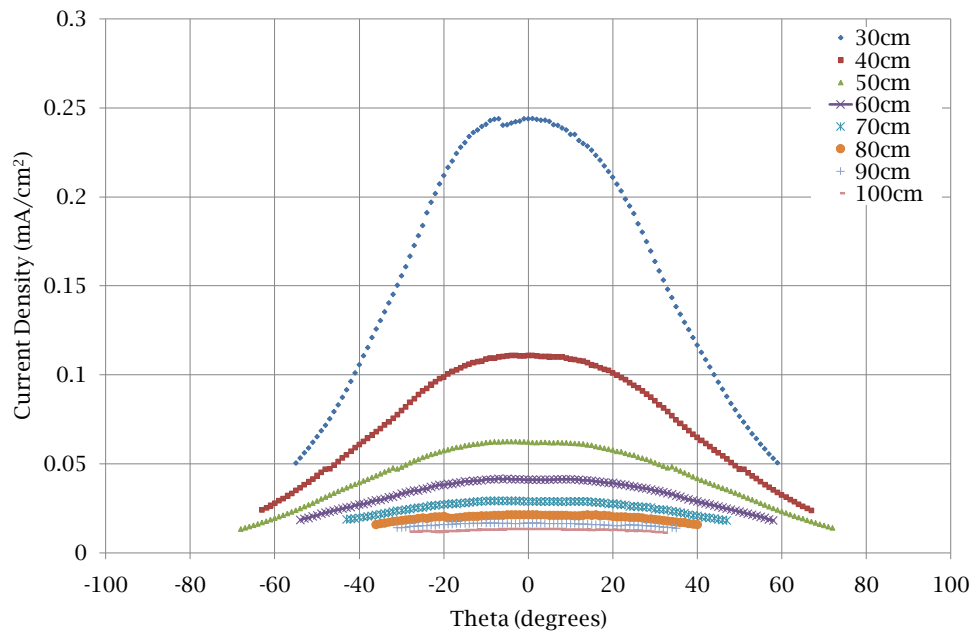


Figure 81: Z-face (plane containing x-face): Single plume mode, 30-100 cm radii.

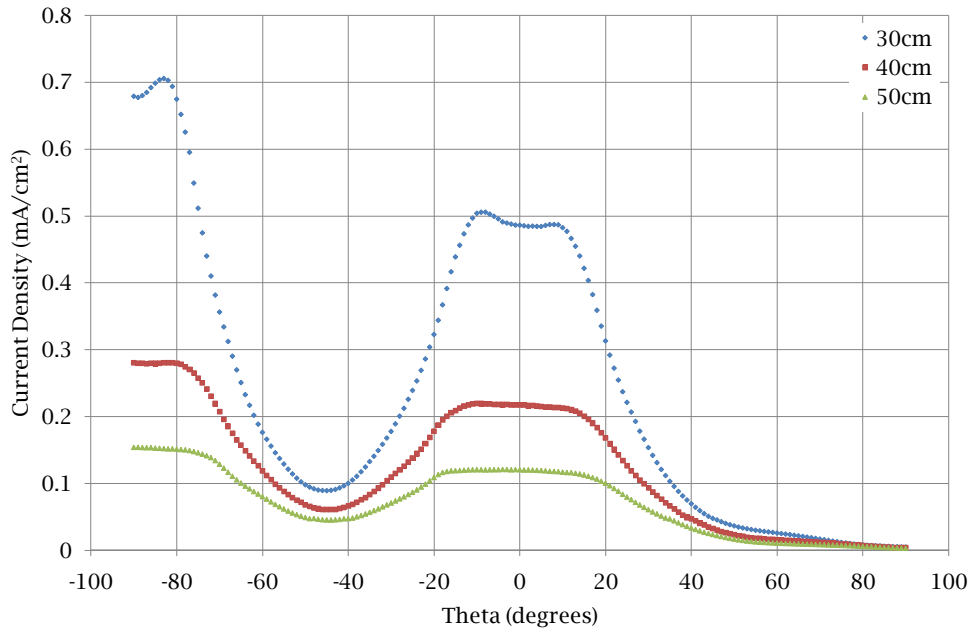


Figure 82: Z-face (plane containing x-face): Double plume mode (x and z-faces operating), 180 degree arc, 30-50 cm radii.

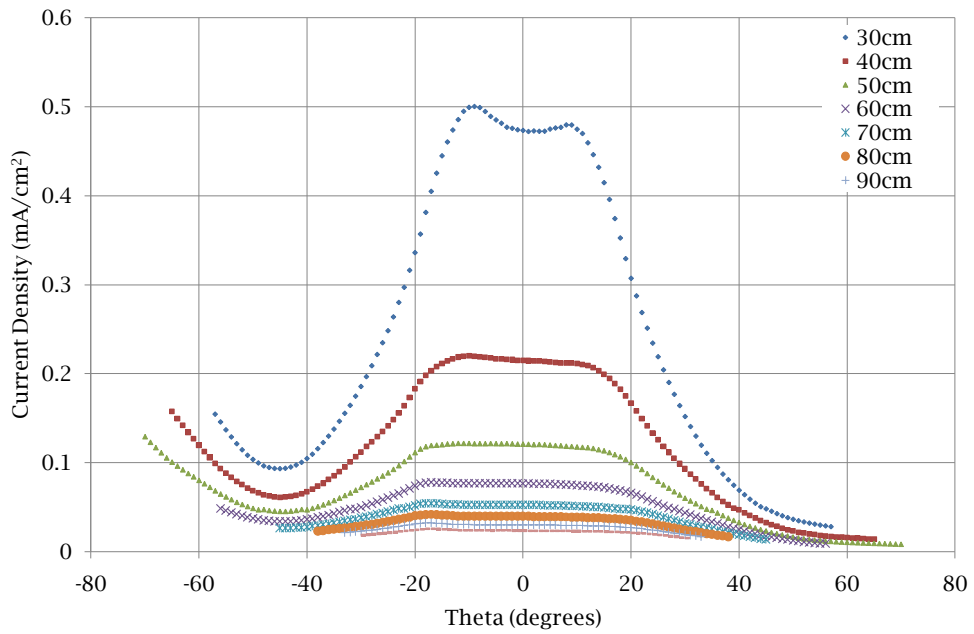


Figure 83: Z-face (plane containing x-face): Double plume mode (x and z-faces operating), 30-90 cm radii.

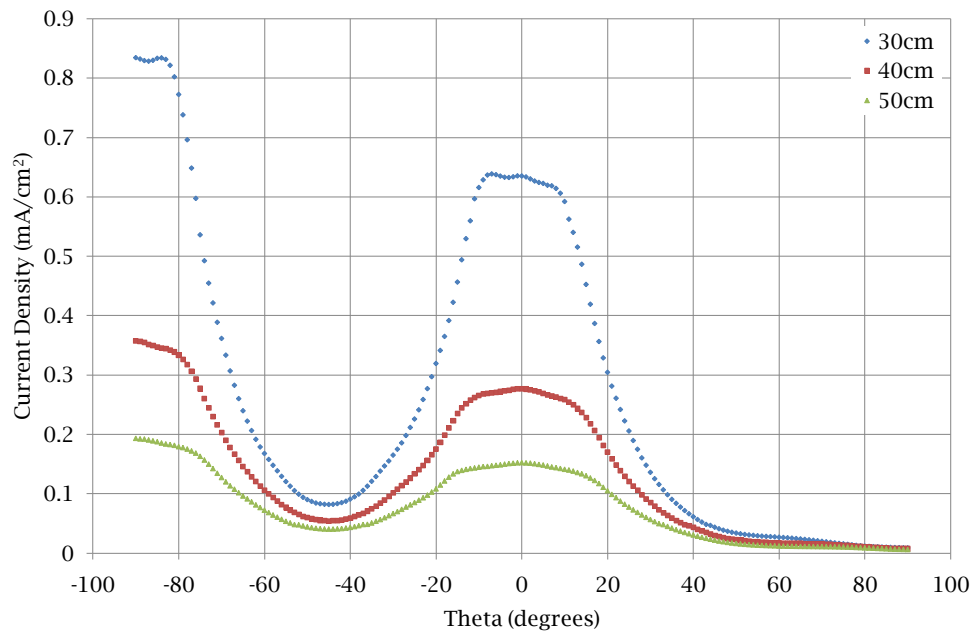


Figure 84: Z-face (plane containing x-face): Triple plume mode, 180 degree arc, 30-50 cm radii.

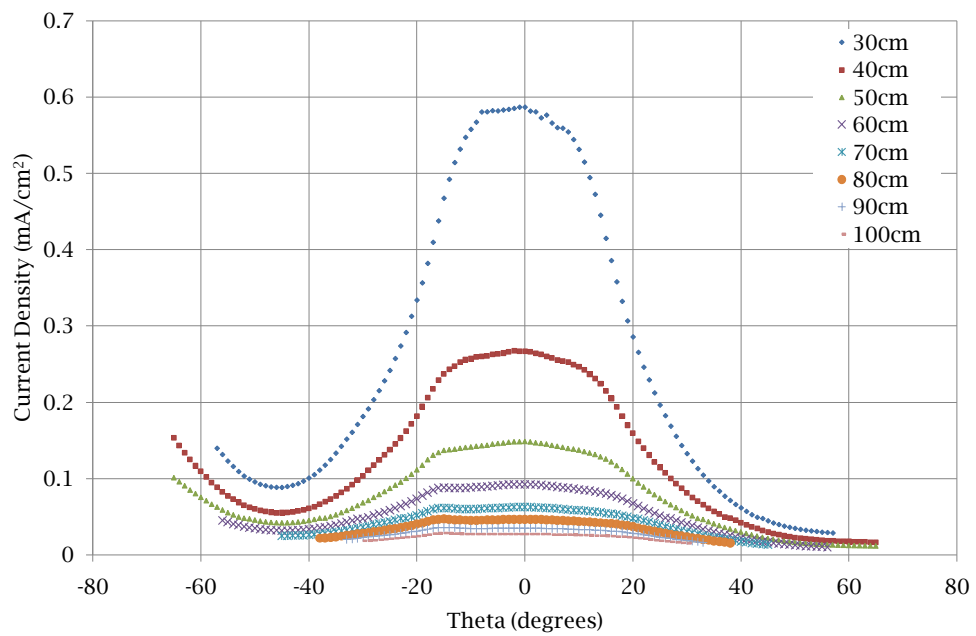


Figure 85: Z-face (plane containing x-face): Triple plume mode, 30-90 cm radii.

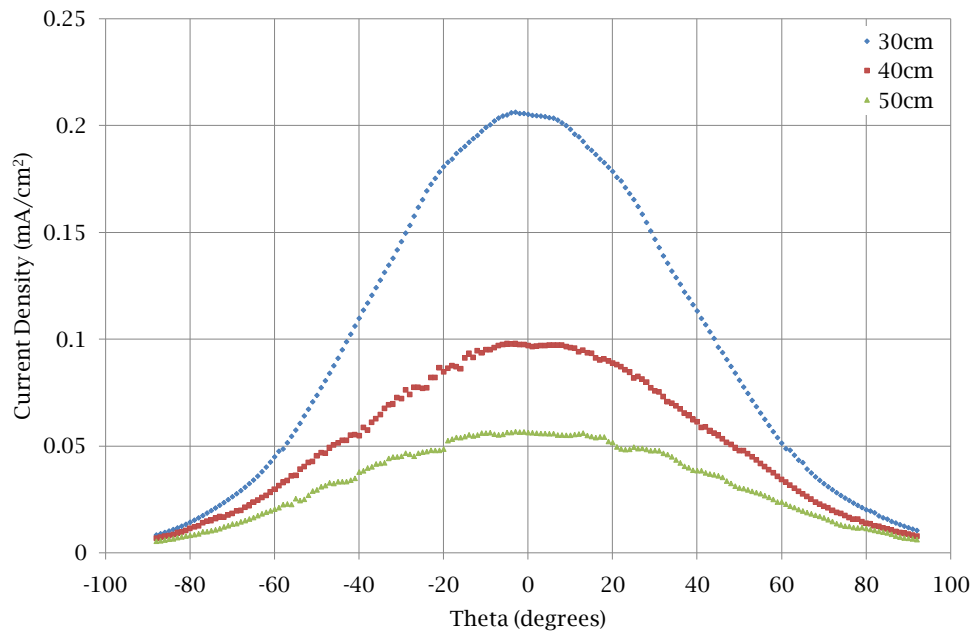


Figure 86: Z-face (plane containing y-face): Single plume mode, 180 degree arc, 30-50 cm radii.

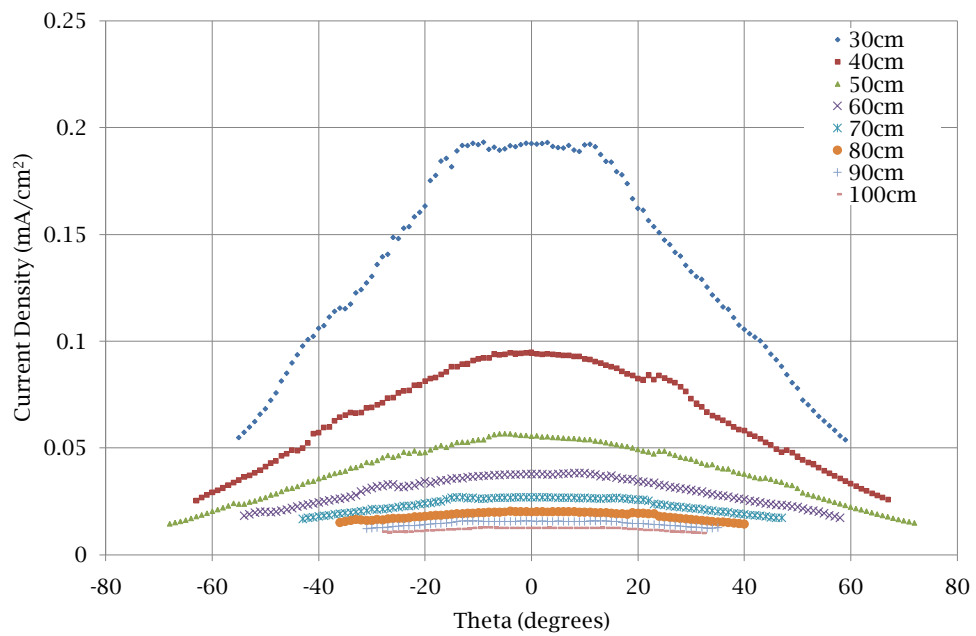


Figure 87: Z-face (plane containing y-face): Single plume mode, 30-100 cm radii.

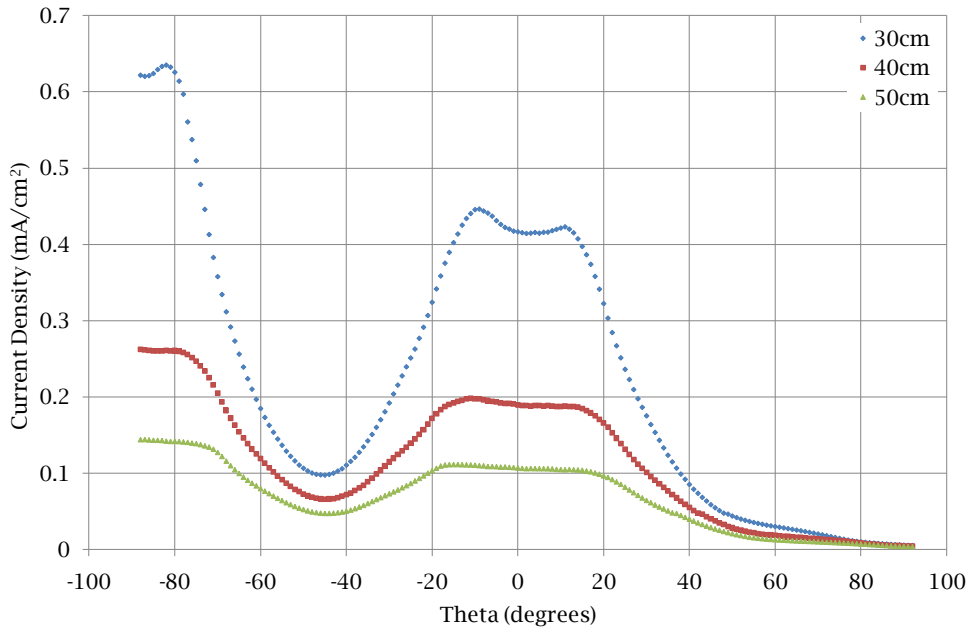


Figure 88: Z-face (plane containing y-face):Double plume mode (y and z-faces operating), 180 degree arc, 30-50 cm radii.

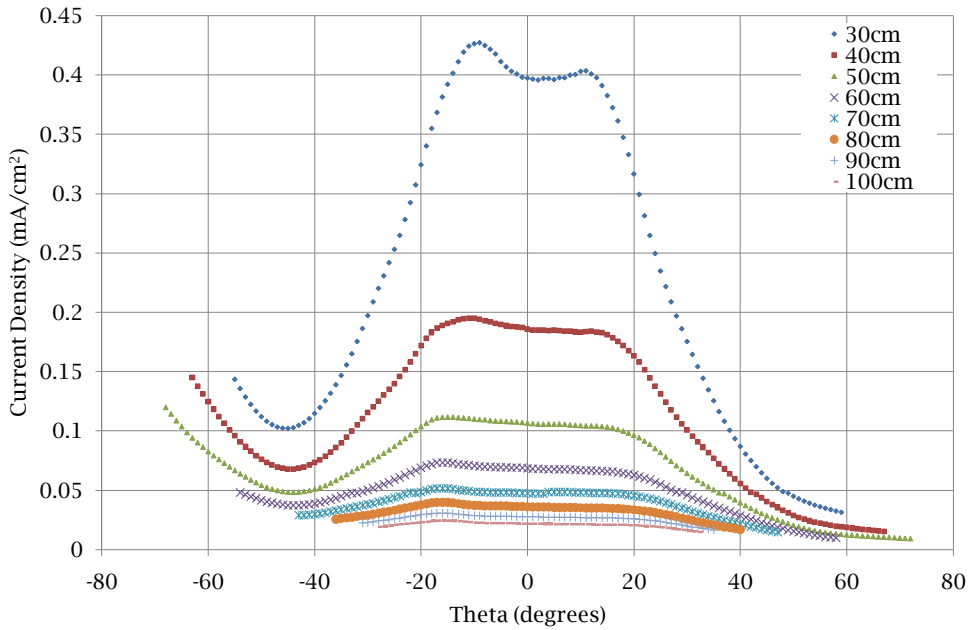


Figure 89: Z-face (plane containing y-face):Double plume mode (y and z-faces operating), 30-100 cm radii.

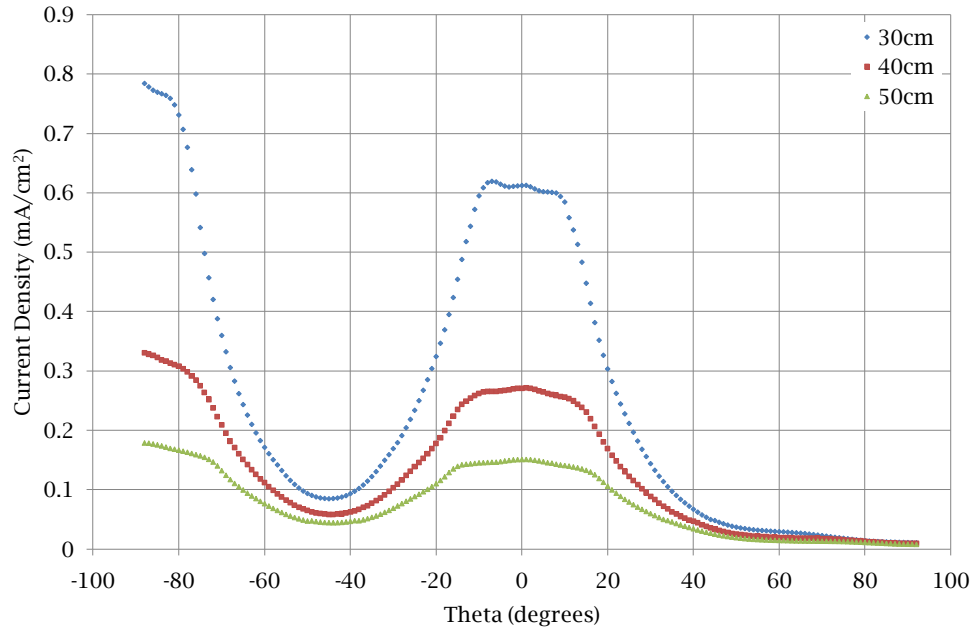


Figure 90: Z-face (plane containing y-face):Triple plume mode, 180 degree arc, 30-50 cm radii.

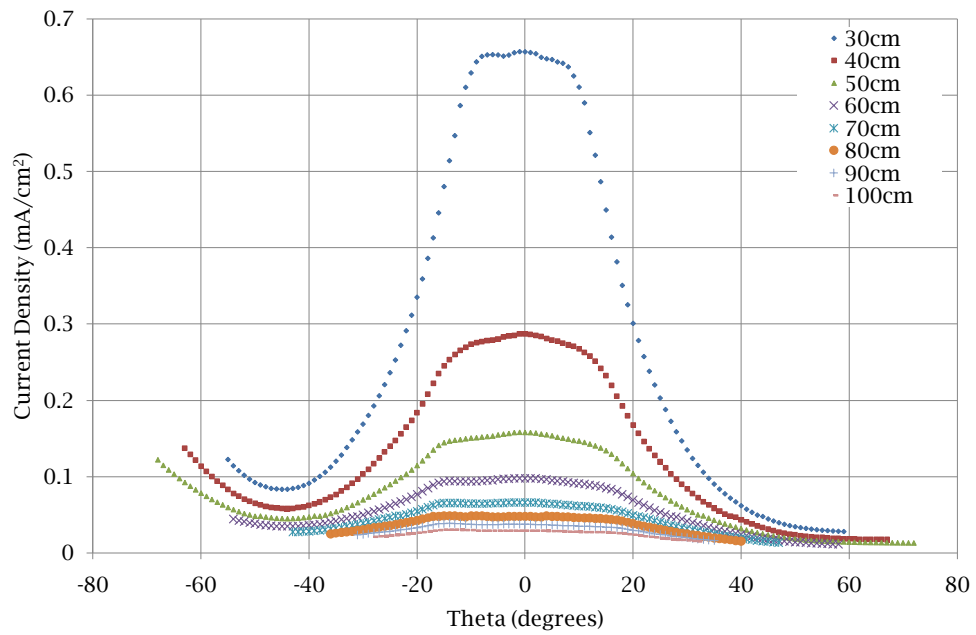


Figure 91: Z-face (plane containing y-face):Triple plume mode, 30-100 cm radii.

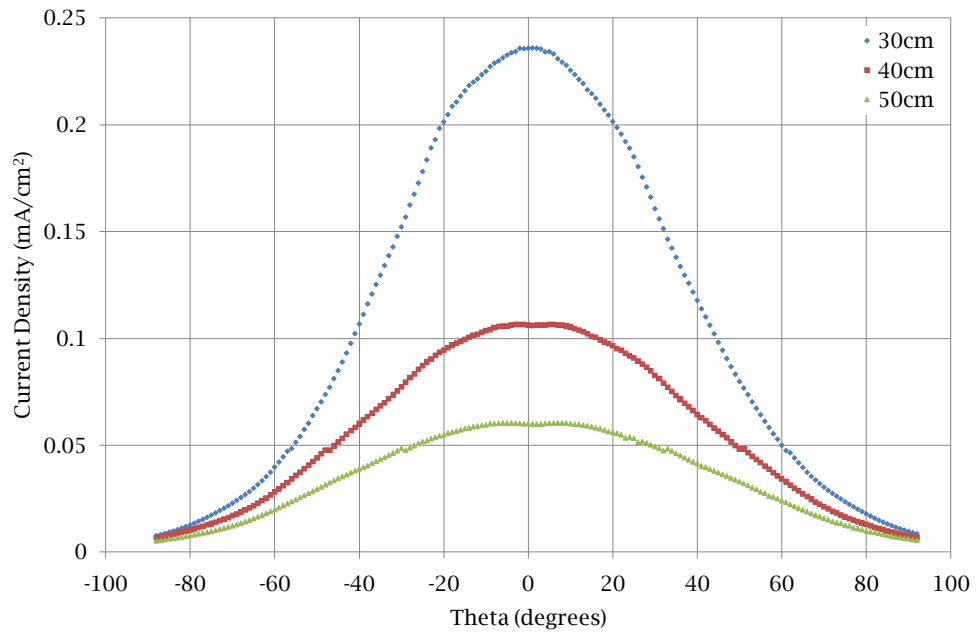


Figure 92: Z-face (plane 45 degrees between x and y-face): Single plume mode, 180 degree arc, 30-50 cm radii.

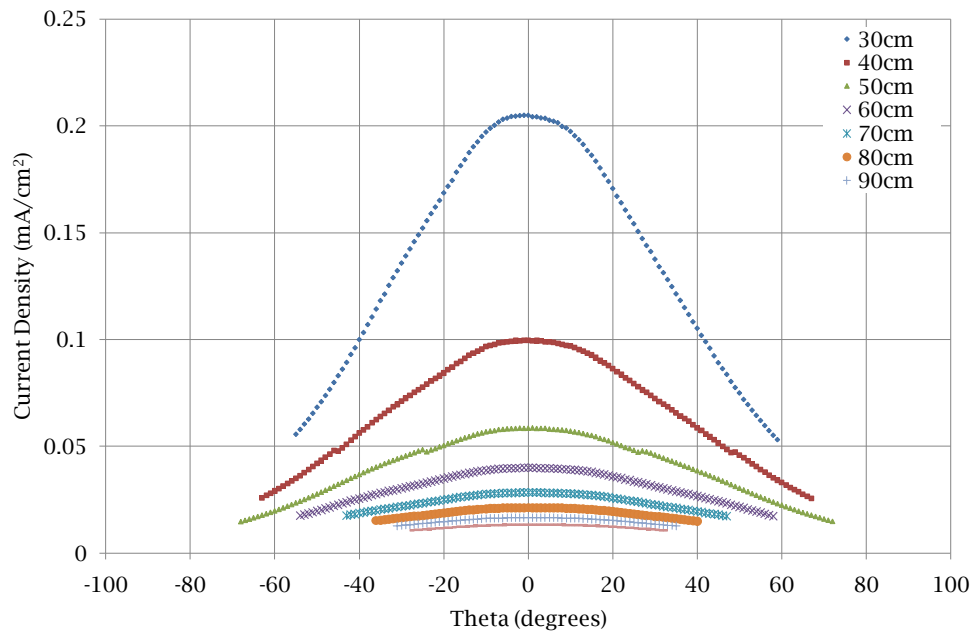


Figure 93: Z-face (plane 45 degrees between x and y-face): Single plume mode, 30-90 cm radii.

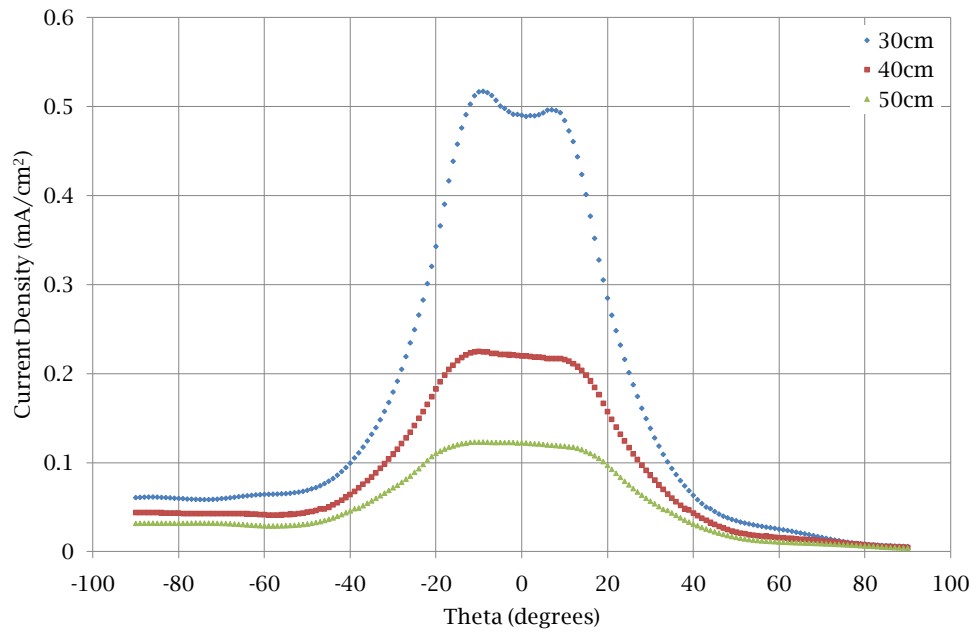


Figure 94: Z-face (plane 45 degrees between x and y-face): Double plume mode (x and z-faces operating), 180 degree arc, 30-50 cm radii.

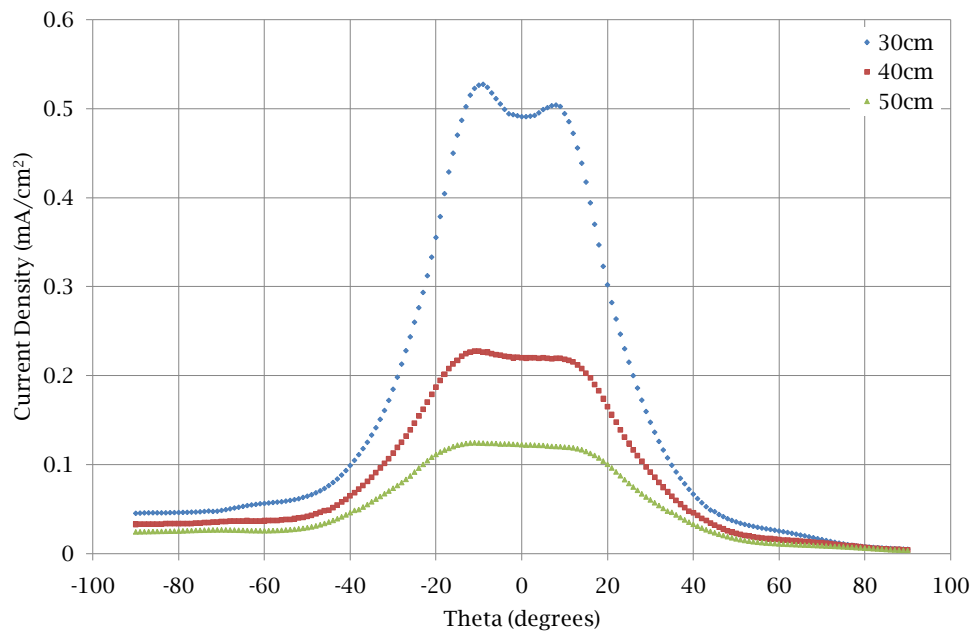


Figure 95: Z-face (plane 45 degrees between x and y-face): Double plume mode (y and z-faces operating), 180 degree arc, 30-50 cm radii.

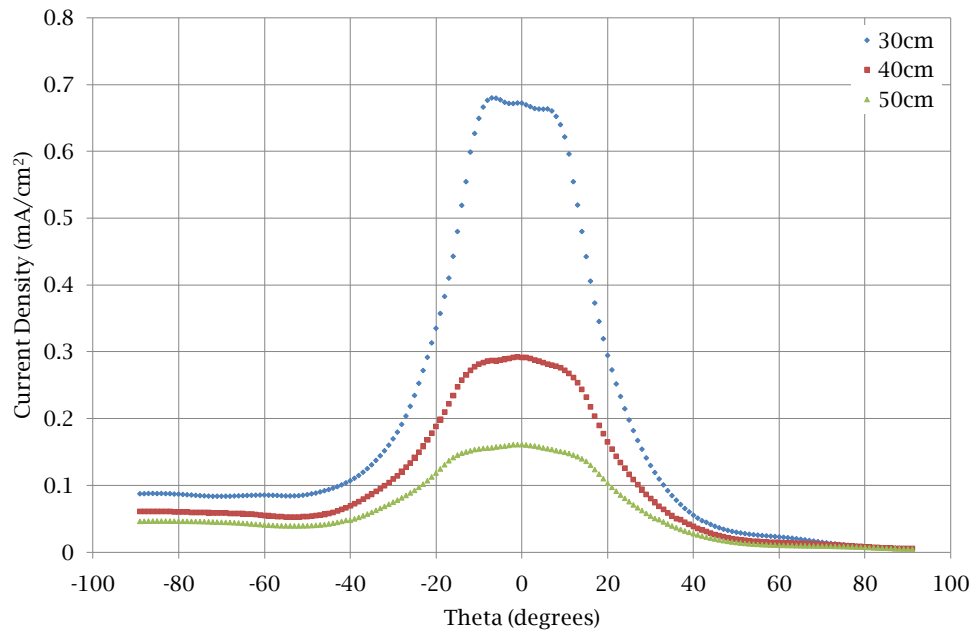


Figure 96: Z-face (plane 45 degrees between x and y-face): Triple plume mode, 180 degree arc, 30-50 cm radii.

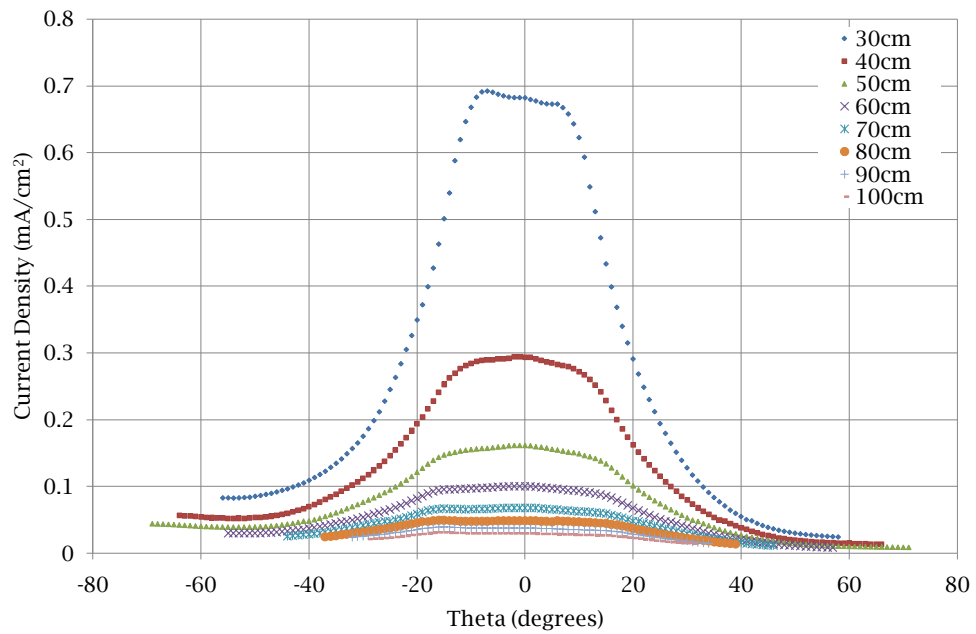


Figure 97: Z-face (plane 45 degrees between x and y-face): Triple plume mode, 30-100 cm radii.

## Bibliography

1. Humble, R. W., Henry, G. N., and Larson, W. J., *Space Propulsion Analysis and Design*, Space Technology Series, McGraw-Hill, 1995.
2. Aerojet, “Aerojet Capabilities - Spacecraft Propulsion,” [Online], 2009, <http://www.aerojet.com/capabilities/spacecraft.php>.
3. Larson, W. J. and Wertz, J. R., editors, *Space Mission Analysis and Design*, Microcosm Press, Torrance, CA, 3rd ed., 1999.
4. Jahn, R. G., *Physics of Electric Propulsion*, Dover Publications, Mineola, NY, 2006.
5. NASA Glenn Research Center, “GRC-NSTAR Ion Thruster,” [Online], April 2009, <http://www.grc.nasa.gov/WWW/ion/past/90s/nstar.htm>.
6. Martinez-Sanchez, M. and Pollard, J. E., “Spacecraft Electric Propulsion—An Overview,” *Journal of Propulsion and Power*, Vol. 14, No. 5, September-October 1998, pp. 688–699.
7. NASA Glenn Research Center, “Magnetoplasmadynamic Thrusters,” [Online], January 2010, <http://www.nasa.gov/center/glenn/about/fs22grc.html>.
8. Charles, C., “Plasmas for spacecraft propulsion,” *Journal of Physics D: Applied Physics*, Vol. 42, 2009, pp. 163001.
9. Rotter, J. E., *An Analysis of Multiple Configurations of Next-Generation Cathodes in a Low Power Hall Thruster*, Master’s thesis, Air Force Institute of Technology, March 2009.
10. Kaplan, M. H., *Modern Spacecraft Dynamics and Control*, John Wiley & Sons, Inc., New York, 1976.
11. Chobotov, V. A., *Spacecraft Attitude Dynamics and Control*, Krieger Publishing Company, Malabar, FL, 1991.
12. Agrawal, B. N., *Design of Geosynchronous Spacecraft*, Prentice-Hall, Inc., Englewood Cliffs, NJ, 1986.
13. Corey, R. L., Snyder, J. S., Price, X., Malone, S. P., and Randolph, T. M., “Hall Thruster Plume Model for Spacecraft Impingement Torque: Development and Validation,” *Journal of Spacecraft and Rockets*, Vol. 45, No. 4, July-August 2008, pp. 766–775.
14. Seikel, G. R., “Generation of Thrust – Electromagnetic Thrusters,” *Proceedings of the NASA-University Conference on the Science and Technology of Space Exploration*, NASA, Chicago, IL, November 1962.

15. Kim, V., Popov, G., Arkhipov, B., Murashko, V., Gorshkov, O., Koroteyev, A., Garkusha, V., Semenkin, A., and Tverdokhlebov, S., "Electric Propulsion Activity in Russia," *27th International Electric Propulsion Conference*, 15-19 October 2001.
16. Finke, R. C., editor, *Electric Propulsion and its Applications to Space Missions*, Vol. 79 of *Progress in Astronautics and Aeronautics*, AIAA, New York, NY, 1981.
17. Hermant, E., "SMART use for electric propulsion," *Aerospace America*, February 2005, pp. 34-37.
18. European Space Agency, "ESA Multimedia Gallery," [Online], 2010, <http://www.esa.int/esa-mm/mmg/home.pl>.
19. Oh, D. Y., "Evaluation of Solar Electric Propulsion Technologies for Discovery-Class Missions," *Journal of Spacecraft and Rockets*, Vol. 44, No. 2, March-April 2007, pp. 399-411.
20. Manzella, D., Oh, D., and Aadland, R., "Hall Thruster Technology for NASA Science Missions," *41st Joint Propulsion Conference and Exhibit*, No. AIAA20053675, Tucson, AZ, July 2005.
21. Dunning, J. W., Hamley, J. A., Jankovsky, R. S., and Oleson, S. R., "An Overview of Electric Propulsion Activities at NASA," *40th AIAA Joint Propulsion Conference and Exhibit*, No. AIAA20043328, NASA, Fort Lauderdale, FL, July 2004.
22. Gorshkov, O., Koroteev, A., Arkhipov, B., Murashko, V., Anfimov, N., Lukyashenko, V., Kim, V., and Popov, G., "Overview of Russian Activities in Electric Propulsion," *37th Joint Propulsion Conference and Exhibit*, No. AIAA-2001-3229, Salt Lake City, UT, July 2001.
23. Busek Space Propulsion, "First US Hall Thruster Operational in Space," Press Release, January 2007.
24. Hammond, W. E., *Design Methodologies for Space Transportation Systems*, AIAA Education Series, American Institute of Aeronautics and Astronautics, Inc., Reston, VA, 2001.
25. Goebel, D. M. and Katz, I., *Fundamentals of Electric Propulsion: Ion and Hall Thrusters*, JPL Space Science and Technology Series, Jet Propulsion Laboratory, March 2008, <http://descanso.jpl.nasa.gov/SciTechBook/SciTechBook.cfm>.
26. Kieckhafer, A., Massey, D., and King, L. B., "Probe Diagnostics in a Bismuth Hall Thruster," *29th International Electric Propulsion Conference*, No. IEPC-05-129, Princeton University, November 2005.
27. Touzeau, M., Prioul, M., Roche, S., Gascon, N., Perot, C., Darnon, F., Bechu, S., Philippe-Kadlec, C., Magne, L., Lasgorceix, P., Pagnon, D., Bouchoule, A., and Dudeck, M., "Plasma diagnostic systems for Hall-effect plasma thrusters," *Plasma Physics and Controlled Fusion*, Vol. 42, 2000, pp. B323-B339.

28. Pacros, A., *Instruments Design and Testing for a Hall Thruster Plume Experiment on the Space Shuttle*, Master's thesis, Massachusetts Institute of Technology, June 2002.
29. Nakles, M. R., Brieda, L., Reed, G. D., Hargus, W. A., and Spicer, R. L., "Experimental and Numerical Examination of the BHT-200 Hall Thruster Plume," *43rd AIAA Joint Propulsion Conference and Exhibit*, No. AIAA 2007-5305, Cincinnati, OH, July 2007.
30. Mikellides, I. G., Jongeward, G. A., Katz, I., and Manzella, D. H., "Plume Modeling of Stationary Plasma Thrusters and Interactions with the Express-A Spacecraft," *Journal of Spacecraft and Rockets*, Vol. 39, No. 6, November-December 2002, pp. 894–903.
31. King, L. B. and Gallimore, A. D., "Ion-Energy Diagnostics in an SPT-100 Plume from Thrust Axis to Backflow," *Journal of Propulsion and Power*, Vol. 20, No. 2, March-April 2004, pp. 228–242.
32. Farnell, C. C., Brown, D. L., Willis, G., and Branam, R., "Remote Diagnostic Measurements of Hall Thruster Plumes," *31st International Electric Propulsion Conference*, No. IEPC-2009-031, Ann Arbor, MI, September 2009.
33. Estublier, D. L., "The SMART-1 Spacecraft Potential Investigations," *IEEE Transactions on Plasma Science*, Vol. 36, No. 5, October 2008, pp. 2262–2270.
34. Azziz, Y., Martinez-Sanchez, M., and Szabo, J. J., "Determination of In-Orbit Plume Characteristics from Laboratory Measurements," *42nd AIAA Joint Propulsion Conference and Exhibit*, No. AIAA 2006-4484, Sacramento, CA, July 2006.
35. Azziz, Y., *Experimental and Theoretical Characterization of a Hall Thruster Plume*, Ph.D. thesis, Massachusetts Institute of Technology, 2007.
36. Farnell, C. C., *Plasma Flow Field Measurements Downstream of a Hollow Cathode*, Ph.D. thesis, Colorado State University, Fort Collins, Colorado, 2007.
37. Capelli, M., "The Hall effect and rocket flight," *Physics Today*, April 2009, pp. 76–77.
38. Bohnert, A. M., *Thermal Characterization of a Hall Effect Thruster*, Master's thesis, Air Force Institute of Technology, March 2008.
39. Choueiri, E. Y., "Fundamental difference between the two Hall thruster variants," *Physics of Plasmas*, Vol. 8, No. 11, November 2001, pp. 5025–5033.
40. Walker, Q. E., Capelli, M. A., and Hargus, W. A., "Preliminary Study of Arcjet Neutralization of Hall Thruster Clusters," *2001 International Electric Propulsion Conference*, No. IEPC-01-63, Electric Propulsion Society, Pasadena, CA, October 2001.

41. Raitses, Y., Smirnov, A., Granstedt, E., and Fisch, N. J., "Optimization of Cylindrical Hall Thrusters," Tech. Rep. PPPL-4256, Princeton Plasma Physics Laboratory, July 2007.
42. Reid, B. M., Brown, D. L., and Haas, J. M., "Performance Measurements of a 3-cm Cylindrical Hall Thruster," *JANNAF Journal of Propulsion and Energetics*, Vol. 2, No. 1, 2009, pp. 64–72.
43. Garrigues, L., Boniface, C., Hagelaar, G., and Boeuf, J., "Performance Modeling of a Thrust Vectoring Device for Hall Effect Thrusters," *Journal of Propulsion and Power*, Vol. 25, No. 5, September-October 2009, pp. 1003–1012.
44. Gallimore, A. D., "Establishment of a Hall Thruster Cluster Test Facility," Tech. rep., University of Michigan, February 2004.
45. NASA Kennedy Space Center, "Kennedy Media Gallery," [Online], July 1998, <http://mediaarchive.ksc.nasa.gov/detail.cfm?mediaid=2442>.
46. Beal, B. E., *Clustering of Hall Effect Thrusters for High-Power Electric Propulsion Applications*, Ph.D. thesis, University of Michigan, 2004.
47. Beal, B. E., Gallimore, A. D., and Hargus, W. A., "Preliminary Plume Characterization of a Low-power Hall Thruster Cluster," *38th AIAA Joint Propulsion Conference and Exhibit*, Indianapolis, IN, July 2002.
48. Lobbia, R. B. and Gallimore, A. D., "Evaluation and Active Control of Clustered Hall Thruster Discharge Oscillations," *41st AIAA Joint Propulsion Conference and Exhibit*, No. AIAA 2005-3679, Tucson, AZ, July 2005.
49. Victor, A. L., Zurbuchen, T. H., and Gallimore, A. D., "Ion-Energy Plume Diagnostics on the BHT-600 Hall Thruster Cluster," *Journal of Propulsion and Power*, Vol. 22, No. 6, November-December 2006, pp. 1421–1424.
50. Walker, M. L. R. and Gallimore, A. D., "Performance Characteristics of a Cluster of 5 kW Laboratory Hall Thrusters," *40th Joint Propulsion Conference and Exhibit*, No. AIAA-2004-3767, July 2004.
51. Hargus, W. A. and Nakles, M. R., "Hall Effect Thruster Ground Testing Challenges," *25th Aerospace Testing Seminar*, American Testing Society, Huntington Beach, CA, October 2009.
52. Brown, D. L., Larson, C. W., Beal, B. E., and Gallimore, A. D., "Methodology and Historical Perspective of a Hall Thruster Efficiency Analysis," *Journal of Propulsion and Power*, Vol. 25, No. 6, November-December 2009, pp. 1163–1177.
53. Polzin, K. A., Markusic, T. A., Stanojevic, B. J., DeHoyos, A., and Spaun, B., "Thrust stand for electric propulsion performance evaluation," *Review of Scientific Instruments*, Vol. 77, 2006, pp. 105108.
54. Hofer, R. R. and Jankovsky, R. S., "Influence of Current Density and Magnetic Field Topography in Optimizing the Performance, Divergence, and Plasma Os-

- cillations of High Specific Impulse Hall Thrusters,” *28th International Electric Propulsion Conference*, No. IEPC2003142, Toulouse, France, March 2003.
55. PHPK Technologies, *Torr Master TM500 Cryopump Instruction Manual*, PHPK Technologies/CVI, Columbus, OH.
  56. PHPK Technologies, *CBST 6.0 Scroll Compressor*, PHPK Technologies/CVI, Columbus, OH.
  57. PHPK Technologies, *Torr Master TM250 Cryopump Instruction Manual*, PHPK Technologies/CVI, Columbus, OH.
  58. Kurt J. Lesker Company, *300 Series Convection Vacuum Gauge User’s Manual*, Kurt J. Lesker Company, Clairton, PA, 114th ed., 2005.
  59. Farnell, C., *AFIT Beam Profiler Overview*, Colorado State University, Ft. Collins, 2007.
  60. Tedrake, R. and Pote, B., “Multi Axis Hall Thruster,” SBIR Phase I Final Report AFRL-PR-ED-TR-2004-0018, Busek Co. Inc., Natick, MA, August 2004.
  61. MKS Instruments, *ALTA Series True Digital Mass Flow Meter/Controller with Analog I/O Instruction Manual*, MKS Instruments, Wilmington, MA, 2004.
  62. Schaevitz Sensors, *Schaevitz MP Series Microprocessor-Based LVDT Readout/Controller Operating Instructions*, Schaevitz Sensors, Hampton, VA.
  63. Thermo Scientific, *NESLAB RTE Series Refrigerated Bath*, Thermo Fisher Scientific, Newington, NH, 2007.
  64. Farnell, C. and Williams, J. D., *Faraday Probe Operating Manual*, Colorado State University, Ft. Collins, 2007.
  65. Azziz, Y., *Instrument Development and Plasma Measurements on a 200-Watt Hall Thruster*, Master’s thesis, Massachusetts Institute of Technology, June 2003.

## *Vita*

LCDR Spencer E. Temkin attended Cornell University under the Naval Reserve Officers' Training Corps scholarship program and graduated with a Bachelor of Arts degree in Chemistry and Chemical Biology in 1999. He was commissioned an Ensign in the United States Navy and was selected for Naval Aviator training, earning the "Wings of Gold" in 2000.

Following a tour flying the P-3C Orion with the VP-8 "Fighting Tigers" of Brunswick, Maine, including two deployments and combat operations in Iraq, LCDR Temkin reported to the VT-28 "Rangers" of Corpus Christi, Texas for duty as a primary instructor pilot in the T-34C Turbo Mentor aircraft. He then served as Aircraft Launch and Recovery Officer aboard the aircraft carrier USS Kitty Hawk (CV-63), homeported in Yokosuka, Japan, during multiple operational deployments and her decommissioning phase.

In 2009 LCDR Temkin reported to the Air Force Institute of Technology. Following his graduation from AFIT he will return to VT-28 as a department head and instructor pilot.

Permanent address: 2950 Hobson Way  
Air Force Institute of Technology  
Wright-Patterson AFB, OH 45433

REPORT DOCUMENTATION PAGE				Form Approved OMB No. 074-0188	
<p>The public reporting burden for this collection of information is estimated to average 1 hour per response, including the time for reviewing instructions, searching existing data sources, gathering and maintaining the data needed, and completing and reviewing the collection of information. Send comments regarding this burden estimate or any other aspect of the collection of information, including suggestions for reducing this burden to Department of Defense, Washington Headquarters Services, Directorate for Information Operations and Reports (0704-0188), 1215 Jefferson Davis Highway, Suite 1204, Arlington, VA 22202-4302. Respondents should be aware that notwithstanding any other provision of law, no person shall be subject to a penalty for failing to comply with a collection of information if it does not display a currently valid OMB control number.</p> <p><b>PLEASE DO NOT RETURN YOUR FORM TO THE ABOVE ADDRESS.</b></p>					
1. REPORT DATE (DD-MM-YYYY) 17-12-2010		2. REPORT TYPE Master's Thesis		3. DATES COVERED (From - To) December 2009 - December 2010	
4. TITLE AND SUBTITLE  Performance Characterization of a Three-axis Hall Effect Thruster				5a. CONTRACT NUMBER	
				5b. GRANT NUMBER	
				5c. PROGRAM ELEMENT NUMBER	
6. AUTHOR(S)  Temkin, Spencer E., LCDR, USN				5d. PROJECT NUMBER 11Y133	
				5e. TASK NUMBER	
				5f. WORK UNIT NUMBER	
7. PERFORMING ORGANIZATION NAMES(S) AND ADDRESS(S) Air Force Institute of Technology Graduate School of Engineering and Management (AFIT/EN) 2950 Hobson Way WPAFB OH 45433-7765				8. PERFORMING ORGANIZATION REPORT NUMBER  AFIT/GAE/ENY/10-D02	
9. SPONSORING/MONITORING AGENCY NAME(S) AND ADDRESS(ES) Air Force Research Lab/Space and Missile Propulsion Div. Att: Dr. William A. Hargus 1 Ara Rd. Edwards, AFB CA 93524 e-mail: <a href="mailto:William.Hargus@edwards.af.mil">William.Hargus@edwards.af.mil</a> comm: 661-275-6799				10. SPONSOR/MONITOR'S ACRONYM(S) AFRL/RZS	
				11. SPONSOR/MONITOR'S REPORT NUMBER(S)	
12. DISTRIBUTION/AVAILABILITY STATEMENT APPROVED FOR PUBLIC RELEASE; DISTRIBUTION UNLIMITED.					
13. SUPPLEMENTARY NOTES					
14. ABSTRACT The research presented here represents the first efforts to operate and quantify the performance of a three-axis Hall effect thruster. This thruster is based on the Busek BHT-200 and used a novel construction with three orthogonal faces and a common magnetic core to reduce size and weight. Operating procedures for the thruster were developed and thrust and current density measurements were performed and compared with the baseline BHT-200. The three-axis thruster was successfully operated in single, double and triple face configurations. Distinct jet plume and ball plume modes were observed. Inverted pendulum thrust stand readings in the single face mode indicated that the three-axis thruster produced considerably lower thrust, specific impulse and thrust efficiencies than the BHT-200. Beam current density measurements conducted using a guarded Faraday probe showed significant differences in plume divergence angle, total beam current and current density distributions between the different faces and different operating modes. Results showed three-axis thruster efficiency and stability improved with more operating faces. Improvements to the three-axis thruster design and thrust stand configuration for use with the thruster were enumerated. Suggestions for refinement to experimental methodologies to optimize testing with the three-axis thruster were made and additional diagnostic techniques were described.					
15. SUBJECT TERMS Space Propulsion, Hall Thrusters, Thrust Stand, Faraday Probe, Attitude Control					
16. SECURITY CLASSIFICATION OF:		17. LIMITATION OF ABSTRACT	18. NUMBER OF PAGES	19a. NAME OF RESPONSIBLE PERSON	
REPORT	ABSTRACT	UU	149	Richard E. Huffman, Lt. Col., USAF	
U	U			19b. TELEPHONE NUMBER (Include area code) 937-255-6565	
c. THIS PAGE					
U					